Politecnico di Torino

argotec
SPACE FOR AMBITIONS

Test-Analysis Automated Correlation and Updating of a Spacecraft Structural Model

Master Thesis

A.A. 2025-2026

Supervisors:
Prof. Alfonso Pagani
Prof. Marco Petrolo
Eng. Marco Giolo
Eng. Corinna Cerini

Candidate:
Leonardo Martoni

Abstract

In present-day mechanical design for space applications, analysis and testing are crucial yet expensive components of the production cycle. As such, correlating the analytical model to the tested product enables companies and researchers to ensure the reliability of the created digital twin, enhancing future design modification capabilities and reducing testing needs. In this master thesis an automated correlation tool is developed in order to reduce times and provide a solid framework for correlating present and future items with reduced modifications. Firstly, a sensor placement algorithm is developed to provide the analyst with meaningful suggestions through an elimination process, and determine useful sensor positions and corresponding FEM nodes. The correlation is then performed through an initial sensitivity process to determine possible updating variables. Once the parameter selection is completed, a frequency-based optimization is performed to fully update the model. This document explores the process performed through all its steps on several items, from initial research to final conclusion, in order to provide a complete explanation of the correlation and its benefits.

Recurring Acronyms

AOCS:	Attitude and Orbital Control System
CAD:	Computer Aided Design
COC:	Cross Orthogonality Check
COG:	Center of Gravity
COTS:	Commercial Off The Shelf
DOF:	Degree Of Freedom
EIM:	Effective Independence Method
EMA:	Experimental Modal Analysis
EPS:	Electrical Power System
ESA:	European Space Agency
FEM:	Finite Elements Model
FEMU:	Finite Elements Model Updating
FFT:	Fast Fourier Transformation
FIM:	Fisher Information Matrix
FRF:	Frequency Response Function
GPKE:	Grid Point Kinetic Energy
IUT:	Item Under Test
MAC:	Model Assurance Criterion
MDOF:	Multiple Degrees Of Freedom
MIMO:	Multiple Input Multiple Output
MKE:	Mean Kinetic Energy
MMI:	Mode Match Index
OMA:	Operational Modal Analysis
SDOF:	Single Degree Of Freedom
STM:	Structural Thermal Model

Contents

1 Introduction **8**
- 1.1 Thesis Background . . . 8
- 1.2 Thesis Objective . . . 8
- 1.3 Thesis Overview . . . 9
- 1.4 Argotec Introduction . . . 11

2 Theoretical Background **17**
- 2.1 Modal Analysis . . . 17
  - 2.1.1 Frequency Response Function . . . 21
  - 2.1.2 Operational Modal Analysis . . . 28
- 2.2 Testing . . . 29
  - 2.2.1 Hammer Test . . . 34
  - 2.2.2 Shaker Test . . . 35
- 2.3 Correlation . . . 36
  - 2.3.1 Frequency Error . . . 37
  - 2.3.2 Modal Assurance Criterion . . . 37
  - 2.3.3 Cross Orthogonality Check . . . 38
- 2.4 Sensitivity Analysis . . . 39

3 State Of The Art **40**
- 3.1 Bibliographic Research . . . 40

4 Items Under Test **43**
- 4.1 HAWK PLUS . . . 43
  - 4.1.1 Design Philosophy . . . 43
  - 4.1.2 Structural Thermal Model . . . 44
  - 4.1.3 HAWK PLUS Propulsion System Dummy Mass Model . . . 45

5 Testing Points Determination **48**
- 5.1 Objectives . . . 48
- 5.2 Pre-Selection . . . 48
  - 5.2.1 Voxelization . . . 48
  - 5.2.2 Kinetic Energy Method . . . 50
- 5.3 Effective Independence Method . . . 51
- 5.4 Results . . . 54
  - 5.4.1 Algorithm Testing - PS Dummy Mass Large Configuration . . . 54

5.4.2 Application - HAWK PLUS STM 59

6 Tests Performed **65**
6.1 Objectives 65
6.2 Hammer Test 66
6.2.1 Test Set-up 66
6.2.2 Test Data 71
6.3 Shaker Test 72
6.3.1 Propulsion System Dummy Mass Test Set-up 72
6.3.2 Propulsion System Dummy Mass Test Data 73
6.3.3 HAWK PLUS Test Set-up 75
6.3.4 HAWK PLUS Test Data 76

7 Updating Process **77**
7.1 Overview 77
7.2 Analytical Model 79
7.3 Test Data 81
7.4 Correlation 82
7.4.1 Frequency Error 82
7.4.2 MAC & MMI 83
7.4.3 Mode Shapes Identification 83
7.5 Error Localisation 86
7.5.1 Sensitivity Analysis 86
7.5.2 First Optimization Iter 87
7.6 Optimization Process 88
7.6.1 Variables Boundaries 88

8 Results **90**
8.1 Test Cases 90
8.2 Propulsion System Dummy Mass 91
8.3 HAWK PLUS STM 94

9 Conclusions **99**
9.1 Future Improvements 99

Bibliography **101**

List of Figures

1.1 Thesis Overview . . . 10
1.2 ISSpresso on-board of the ISS [Arg] . . . 11
1.3 LICIACube image of asteroid ejecta [ESA22] . . . 12
1.4 ArgoMoon image of Earth [AN22] . . . 13
1.5 IRIDE Project logo [ESA25] . . . 14
1.6 Pathfinder's First Image over Rome [ESA25] . . . 15

2.1 Spring-Mass-Dampener Model [Pag25] . . . 18
2.2 Free Multi-DOF System with Negligible Damping [Pag25] . . . 19
2.3 Simple Plate Sine Dwell Response [Avi14] . . . 21
2.4 Overlay of Time and Frequency Response Function [Avi14] . . . 22
2.5 Variables Predominant in each FRF area [Ras] . . . 24
2.6 Single H_{ii} Element Magnitude [HF01] . . . 25
2.7 Complete H Magnitude Matrix [Avi14] . . . 25
2.8 Phase Changes Associated with Resonance Peaks [Avi14] . . . 27
2.9 Jitter deformation in Satellite images [Liu+22] . . . 30
2.10 Laser Doppler Vibrometer with acusto-optics modulators [Chi21]. . . . 32
2.11 Results of a high-speed camera system recording and comparison of different magnification algorithms applied to the result [CS25]. . . . 32
2.12 Roving Hammer vs Roving Accelerometer [Avi14] . . . 35
2.13 Hammer and Shaker testing on cantilever beam [Avi14] . . . 36

4.1 HAWK PLUS Render . . . 43
4.2 HAWK PLUS Brochure Showcase of the Different Bays [Srl25] . . . 44
4.3 HAWK PLUS STM . . . 45
4.4 STM Propulsor Dummy Mass in Small Configuration . . . 46
4.5 STM Propulsor Dummy Mass in Large Configuration . . . 47

5.1 Different Voxel Sizes [Oh+21] . . . 49
5.2 Voxel Conditioning . . . 52
5.3 MKE Conditioning . . . 52
5.4 Propulsor FEM Model - Large Configuration . . . 54
5.5 Voxel Selection . . . 55
5.6 MKE Selection . . . 55
5.7 Voxel MAC . . . 56
5.8 MKE MAC . . . 56
5.9 Propulsor FEM Model - Small Configuration . . . 57

5.10 Propulsion System Dummy Mass Small Configuration - Final Selection . 58
5.11 Propulsion System Dummy Mass Small Configuration - MAC 59
5.12 Example of tertiary structure selection points due to local modes 60
5.13 Local Mode affecting the tertiary structure panels 61
5.14 Modal Participation distribution in the first 100 modes 62
5.15 Sensor Location on Payload Interface (Z+) 64

6.1 Sensor Roving during Hammer Testing 68
6.2 Sensor Locations in the Z+ Plate 69
6.3 Sensor Positioning in the Z+ Plate 70
6.4 Photographs taken during Hammer Test 70
6.5 FRF Between MP6 and input 71
6.6 Sensor Placement during Vibration Testing 72
6.7 Superposition of all FRFs captured during the test 73
6.8 Accelerometers FRFs 74
6.9 STM setup on the Shaker Slip Table 75
6.10 Output Example from the Vibes Test 76

7.1 Detailed Correlation Plan 78
7.2 Comparison between analysis and test results in the Z axis 85

8.1 Error Evolution over 10 iterations 92
8.2 MAC Matrices before and after Optimization 93
8.3 Error Evolution during the optimization iteration 96
8.4 MAC Matrices before and after Optimization 98

List of Tables

5.1 Conditioning and Matrix Size for different pre-selection optimizations . . 52
5.2 MAC values after EIM selection with the 2 different methods 56
5.3 Modal Partecipation Table 61
5.4 Node Selected by the Algorithm 63

6.1 Sensor Positions and main accelerometer direction for Hammer Test . . . 67

7.1 Variables Boundaries Overview 89

8.1 Correlation results for PS Dummy model 91
8.2 Variables Variation with respect to their original value 92
8.3 Correlation results for HAWK PLUS STM 95
8.4 Variables Variation with respect to their original value 95
8.5 Correlation results after the second optimization 97
8.6 Variables Variation in the second optimization 97

Introduction

1.1 Thesis Background

The current fast paced growth of the space economy and its related markets is posing a daily challenge to the industries working in the sector, as shorter and faster delivery times are expected with each new order. This quickening in the industrial process is to be achieved without loss of quality and safety regulations to ensure that the high-tech end of the line products retain the usual reliability, which is key in challenging environments related to space. In order to achieve such challenging goals from a structural and mechanical point of view, it is deemed necessary to properly correlate the Finite Element Models to ensure analysis fidelity and acceptability. This process allows the analyst to correct the FE model and reduces the need for extensive testing in changing future configurations, thanks to increased trust in the analytical model.
This thesis aims to implement an autonomous correlation method that is completely independent from the Item Under Test (IUT), to provide a reusable and adaptable tool to serve several different systems and spacecraft. The tool was developed by the author during his internship period at Argotec S.r.l. using their testing facilities and developed models to successfully correlate the HAWK PLUS Structural Thermal Model (STM). Throughout the entire period, the author has also been supported and counseled by the PoliTo university supervisors, who provided crucial insights and material for developing the final product.

1.2 Thesis Objective

As stated the thesis aims to provide a methodology, able to automatically and iteratively correlate given FE models to the test data. The methodology must also be agnostic to the provided model and easily

adaptable to fit different test cases with minimal change. A customized tool, created through python code and defined by the methodology hereby descripted, is implemented to correlate different test cases. The most important and defining test case in the thesis is represented by the HAWK PLUS Structural Thermal Model.

1.3 Thesis Overview

A preliminary assessment of the intended correlation plan begins with active research on the current state of the art (chapter 3), in order to showcase the differences between the chosen method and its application with regard to readily available and known methods in literature. The introduction chapter is followed by a theoretical background definition (chapter 2), in order to provide the reader with useful notations and equations adopted throughout the method definition. An ulterior section (chapter 4) is dedicated to briefly showcase the IUTs and HAWK PLUS as a standardized platform. Necessary data for the correlation, as well as how it was obtained, is detailed in two distinct sections, addressing a developed testing point selection algorithm (chapter 5) and consequently, performed tests (chapter 6).
Most importantly, the developed updating methodology is explained in detail through all its phases in chapter 7 and especially in section 7.1 to fully showcase the procedure in all its steps. Lastly, the results gathered from two different test cases are described in chapter 8, and the drawn conclusions are gathered in chapter 9, along with possible future enhancements of the methodology. A visual map of the thesis work and the interconnections between the proposed Chapters is visible in Figure 1.1.

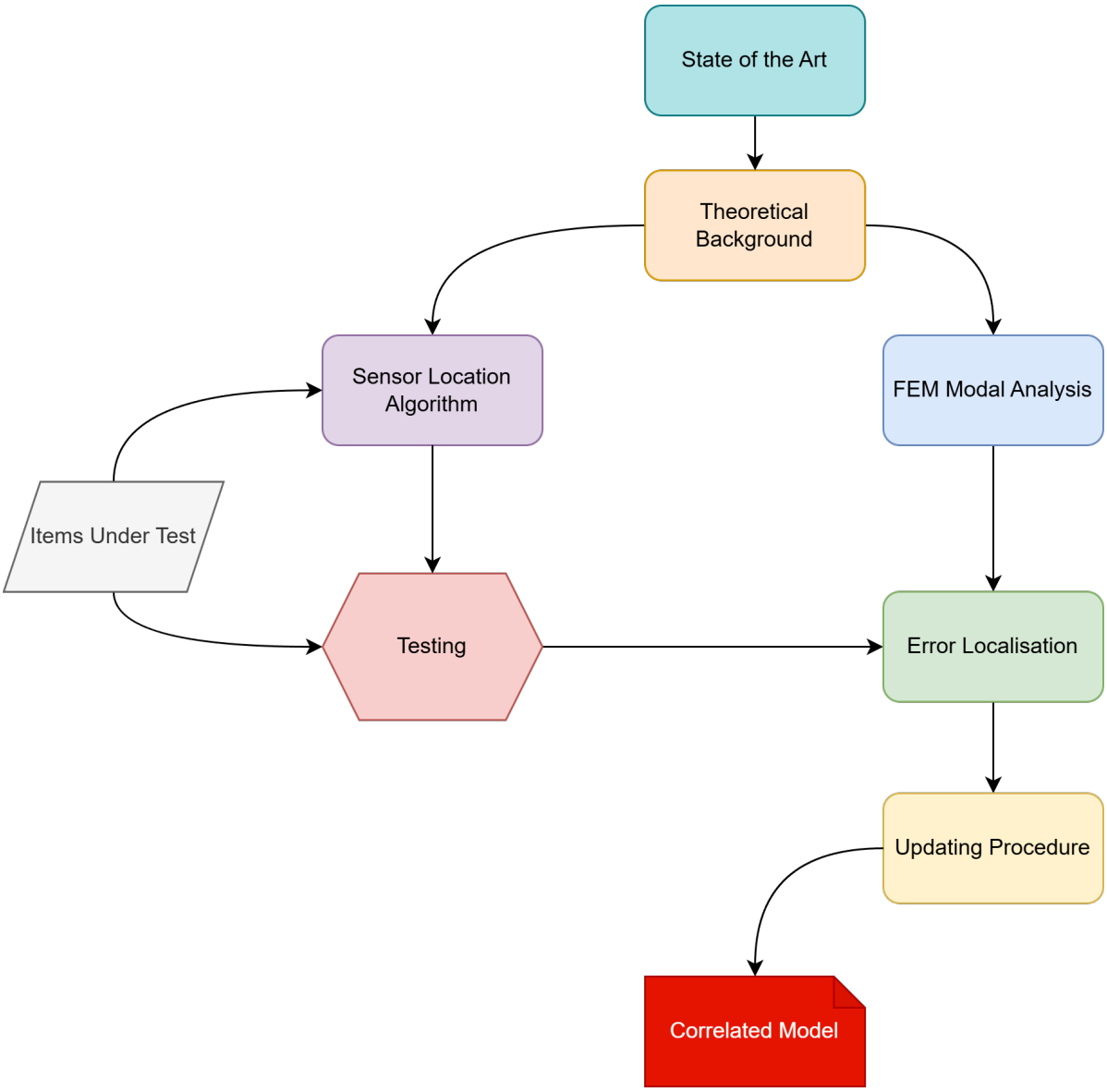

Figure 1.1: Thesis Overview

1.4 Argotec Introduction

HAWK PLUS is a project developed by Argotec Srl, an aerospace company based in San Mauro Torinese, Italy, founded by David Avino in 2008. The company specializes in the design, manufacturing, and operation of Small Satellites (up to 250 kg) and the development of support and comfort solutions for astronauts and future space explorers. Argotec laboratories and facilities are located in Italy, the US, and the European Astronaut Center (EAC) in Cologne, where several activities are carried out in collaboration with the Italian Space Agency. The company accomplished several successful missions since its creation, notably in a temporal order:

- **[2015-17]ISSpresso:** ISSpresso was the first espresso coffee machine designed for use in space, produced for the International Space Station by Argotec and Lavazza in a public-private partnership with the Italian Space Agency (ASI). ISSpresso was one of nine experiments selected by the Italian Space Agency for the Futura mission.

Figure 1.2: ISSpresso on-board of the ISS [Arg]

- **[2019-22]LICIACube:** a microsatellite designed, built, and operated by Argotec as part of NASA's Double Asteroid Redirection Test (DART) mission, the first planetary defense mission in history. LICIACube successfully separated from DART main body and took over 600 images of the impact between the DART probe and the asteroid Dimorphos at 11 million kilometers from Earth,while traveling at a speed of 7 km/sec. In August 2023,LICIACube was named the AIAA Mission of the Year.

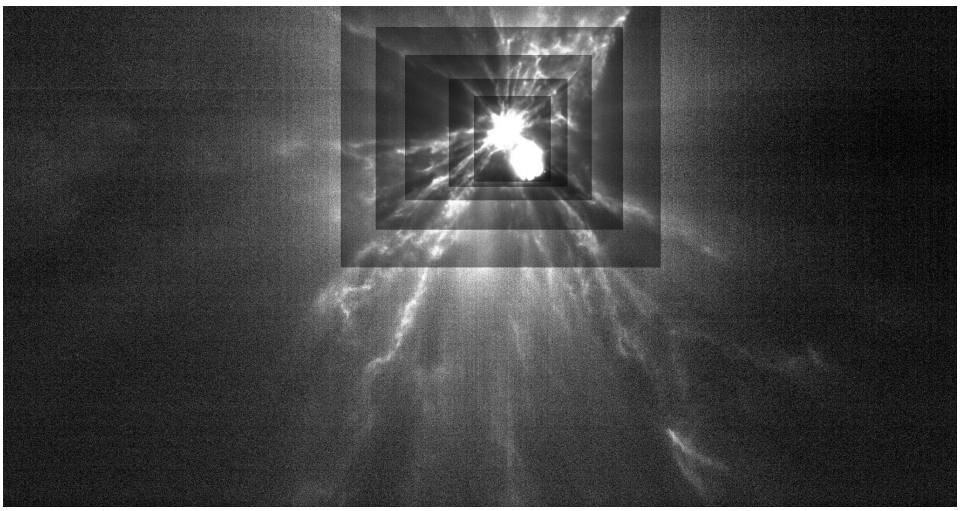

Figure 1.3: LICIACube image of asteroid ejecta [ESA22]

- **[2019-22]ArgoMoon:** a microsatellite designed, built, and operated by Argotec, launched as part of NASA's Artemis 1 mission, the first in the Artemis program, which aims to return humanity to the Moon. As the only European satellite among 10 selected through a rigorous process by NASA, ArgoMoon flew aboard the Space Launch System (SLS). Of these 10 satellites, only 4 successfully established communication with Earth after being deployed from the SLS's second stage, and ArgoMoon was one of them. Its mission was to validate technology in orbit and capture images of the Moon and Earth from a unique vantage point.

Figure 1.4: ArgoMoon image of Earth [AN22]

- **[2025-Today]HEO for IRIDE:** Hawk for Earth Observation(HEO)

Figure 1.5: IRIDE Project logo [ESA25]

is Argotec solution for the IRIDE constellation commissioned by the italian government. The HEO constellation can monitor climate change and its effects in near real time, including soil erosion, deforestation, and ice melting. It can also provide timely warnings to prevent damage from natural disasters such as avalanches, floods, and earthquakes. The current constellation is comprised of HEO Pathfinder and 7 following HEO satellites all already operative in Low Earth Orbit. Pathfinder already provided successfull images of the capital city Rome with a spacial resolution as small as 2.66m as visible in Figure 1.6.

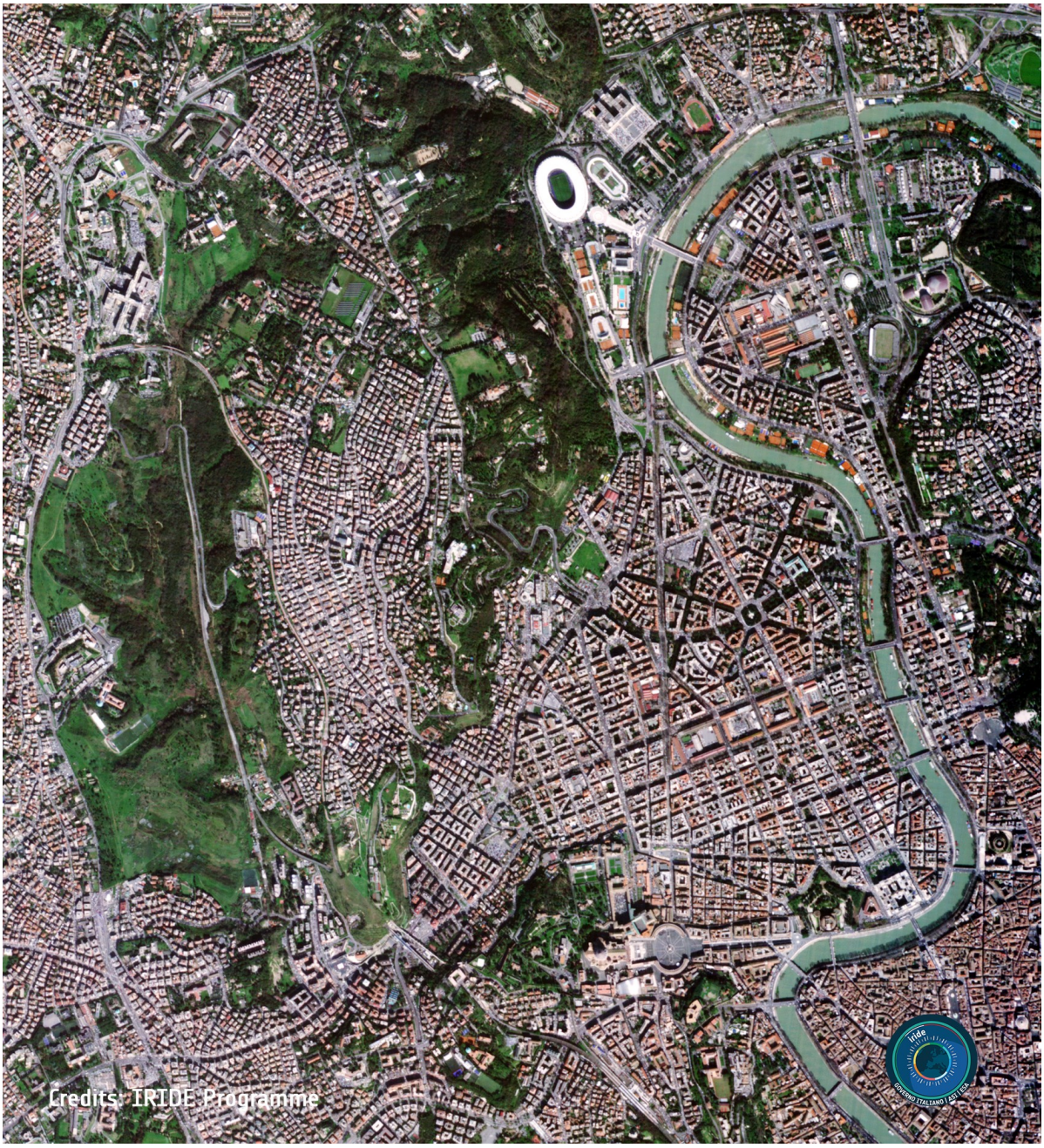

Figure 1.6: Pathfinder's First Image over Rome [ESA25]

- **[Today]Current Projects:** Currently Argotec is working on several missions such as HENON and LUMIO. The first is a mission which will pioneer the use of a Distant Retrograde Orbit (DRO) in the Sun-Earth system, a trajectory never before employed for application and scientific purposes in the study of Space Weather. The second instead is an ambitious mission aimed at observing and quantifying the flashes caused by meteoroid impacts on the far side of the Moon.

Operating from a halo orbit at the Lagrange point L2 in the Earth-Moon system, LUMIO's CubeSat will complement observations collected from Earth and contribute to creating an accurate model of meteoroid flow in the lunar environment. Lastly, and most importantly for this thesis, Argotec is undergoing a platform standardization program to enhance and industrialize its HEO platforms for commercial use. This project will be further detailed in section 4.1.

Theoretical Background

2.1 Modal Analysis

Modal Analysis is a process whereby the dynamic properties of a structure are investigated. The main dynamic properties of interest in a structure are its natural frequencies, mode shapes and damping. Natural frequencies are the frequencies at which a system naturally vibrates once it has been forced into motion, in case of a singular DOF system it can be easily computed as:

$$w_n = \sqrt{\frac{k}{m}} \qquad [\frac{rad}{s}] \tag{2.1}$$

This crucial equation 2.1 represents the analytical solution of the homogeneous equation of motion of a single DOF system represented by a spring-mass-dampener simplified model, where damping is supposed negligible with respect to the acting forces.
The system previously defined and visible in Figure 2.1 is described by the simplified equation of motion:

$$m\ddot{x}(t) + kx(t) = 0 \tag{2.2}$$

Which has a general harmonic solution :

$$x_h(t) = Asin(\omega t) + Bcos(\omega t) \tag{2.3}$$

Including Equation 2.3 in Equation 2.2 yields the following Equation 2.4 which is only solvable for the trivial solution, when A and B are zero, or when ω is a natural frequency of the structure as described by Equation 2.1.

$$A(k - m\omega^2)sin(\omega t) + B(k - m\omega^2)cos(\omega t) = 0 \tag{2.4}$$

The equations discussed above are true for a single DOF system but can be propagated in matrix form for non-constrained multi-DOF systems

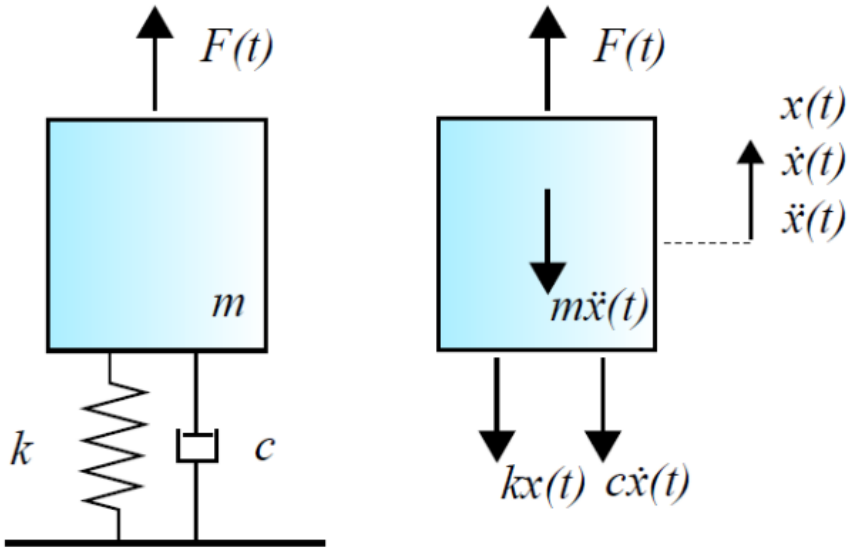

Figure 2.1: Spring-Mass-Dampener Model [Pag25]

with the same negligible damping assumption, such as the one visible in Figure 2.2. The linear equilibrium equations system for the model described in Figure 2.2 can be written as:

$$\begin{bmatrix} m_1 & 0 & 0 & 0 \\ 0 & m_2 & 0 & 0 \\ 0 & 0 & m_3 & 0 \\ 0 & 0 & 0 & m_4 \end{bmatrix} \begin{Bmatrix} \ddot{x}_1(t) \\ \ddot{x}_2(t) \\ \ddot{x}_3(t) \\ \ddot{x}_4(t) \end{Bmatrix} + \begin{bmatrix} k_1 & -k_1 & 0 & 0 \\ -k_1 & k_1+k_2 & -k_2 & 0 \\ 0 & -k_2 & k_2+k_3 & -k_3 \\ 0 & 0 & -k_3 & k_3 \end{bmatrix} \begin{Bmatrix} x_1(t) \\ x_2(t) \\ x_3(t) \\ x_4(t) \end{Bmatrix} = \begin{Bmatrix} 0 \\ 0 \\ 0 \\ 0 \end{Bmatrix} \quad (2.5)$$

Or shortly:

$$M\ddot{x}(t) + Kx(t) = 0 \quad (2.6)$$

Equation 2.6 has an harmonic solution $x(t) = \phi e^{i\omega_n t}$ which substituted in the formula yields the classical eigenvalues problem used to describe and compute numerically eigenvalues, representing the natural frequencies of the model and eigenvectors, representing its mode shapes.

$$(K - \lambda M)\phi = 0; \qquad \lambda = (\omega_n)^2 \quad (2.7)$$

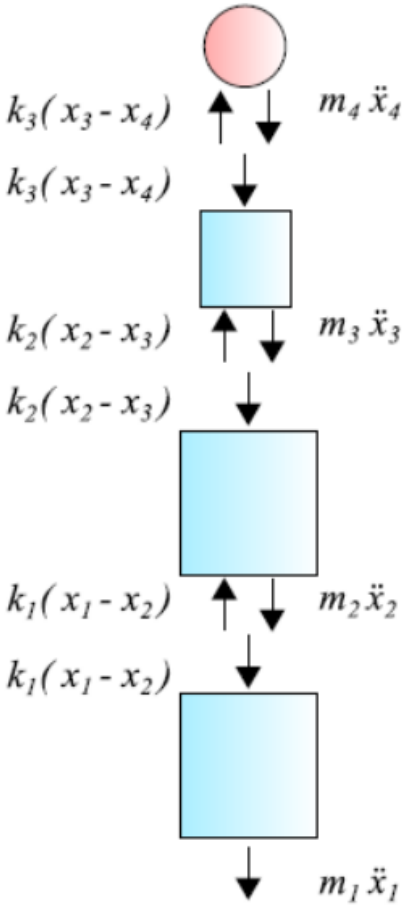

Figure 2.2: Free Multi-DOF System with Negligible Damping [Pag25]

Mode shapes represent the oscillating patterns the structure undergoes when subjected to frequencies matching its natural ones. These particular load cases are called resonances and are especially dangerous for structures as the input force is magnified uncontrollably, possibly causing structural damage or even leading to catastrophic structural failures.
Understanding the natural frequencies of a structure is therefore necessary to ensure structural safety and reliability in the different operative phases of the mission. Usually, this necessity directly translates to a requisite which the launcher service provider specifically imposes on the custom structure.
In a linear vibrating system, the natural mode shapes form a set of mutually orthogonal vectors, meaning that each mode represents an independent pattern of deformation that does not overlap energetically

with the others. These mode shapes are not unique in amplitude: each eigenvector ϕ is only defined up to an arbitrary multiplicative constant, because the underlying equilibrium equations constitute a homogeneous system. As a consequence, the components of ϕ are not uniquely fixed; for each mode there are effectively only $n-1$ independent equations, and the remaining degree of freedom can be used to assign an arbitrary value to one component (often the $n-th$), which is usually done to introduce a normalization condition (for example, mass-normalization or setting a chosen component to unity). In Equation 2.8 mass normalization is described:

$$\Phi^T M \Phi = I \tag{2.8}$$

It is important to note that eigenvector calculations are extremely computationally burdensome and while it is true that every DOF in the structural model has its own natural frequency and associated modal shape, it is practically unfeasible to compute each and every one. To address this limitation participation factors and corresponding modal effective mass are computed as follows:

$$L_i = \{\phi_i^T\}[\mathbf{M}]\{\mathbf{R}\} \qquad m_{eff,i} = L_i^2 \tag{2.9}$$

R is defined as the rigid-body motion or the displacement pattern that arises when the base of the structure is subjected to a unit imposed motion. In other words, we imagine the entire base moving by a unit displacement, and we observe how the system moves as a whole when no internal deformation is allowed. Both the above can be normalized over the global mass in order to be expressed as a percentage of the overall excited mass:

$$\Gamma_i = \frac{L_i}{m_{g,i}} \qquad m_{eff,i} = \frac{L_i^2}{m_{g,i}} \tag{2.10}$$

Equations 2.9 and 2.10 are actively used to limit the output eigenvectors once a target effective mass has been reached. This is possible because only a few modes really excite a sensible percentage of modal effective mass, and as such those modes are the primary interest of the analysis, as well as the most representative of the real response under testing of the final structure. A visual example of mode shapes associated with response peaks (both in frequency and time domains) is provided in case of a simple plate sine dwell response in Figure 2.3.

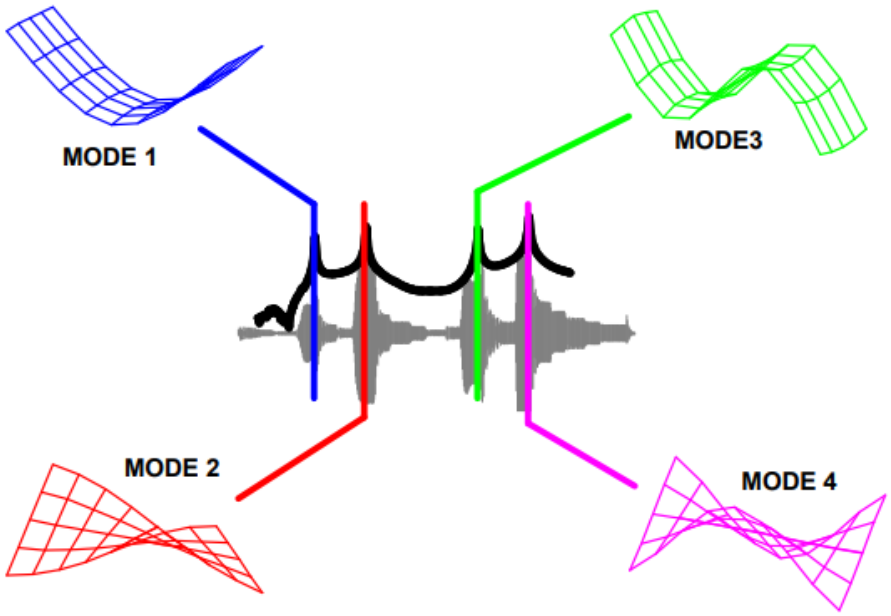

Figure 2.3: Simple Plate Sine Dwell Response [Avi14]

The last important structural dynamic property often studied in the modal analysis is the damping factor, representing how the structure naturally dampens the input frequency and load and it is often numerically estimated.
Modal Analysis is performed on Finite Element Models (FEM), which are a discretization of the real structure, often represented digitally through a CAD. Such discretizations involve describing the model as an assembly of nodes and elements, which can be one-dimensional,two-dimensional or three-dimensional with different properties and characteristics, useful for reducing and describing different structural parts of the real body. In the following chapters, all FE models and respective analysis and optimizations are performed using Simcenter Femap to model, pre-process and post-process the different analysis sets, which are then computed using Nastran solvers, mainly SOL103 and SOL200.

2.1.1 Frequency Response Function

A Frequency Response Function (FRF) describes the steady-state response of a system to harmonic excitation as a function of excitation frequency. In general, an FRF is defined as the (complex) ratio of output response to input force for a known periodic input in steady state. Formally, if $F(\omega)$ and $X(\omega)$ are the Fourier transforms (or phasor amplitudes) of the input

force $f(t)$ and output response $x(t)$ respectively, then the FRF is:

$$H(\omega) = \frac{X(\omega)}{F(\omega)} \tag{2.11}$$

This function characterizes the system's dynamic behavior in the frequency-domain, and is in fact the Fourier transform of the impulse response function of the structure. The FRF is generally complex-valued, having both a magnitude (gain) and a phase, indicating how much the system amplifies/attenuates at each frequency and the phase lag between input and output. An FRF is an inherent property of a linear structure (depending only on its mass, damping, and stiffness distributions) and is independent of the amplitude of excitation, if no damping is present, the FRF becomes purely real-valued (zero phase) because the system's response is in phase or 180° out of phase with the input across all frequencies. In Figure 2.4 a simple example of FRF is shown overlaid to its time domain equivalent to showcase peaks similarities, based on the same plate example of Figure 2.3.

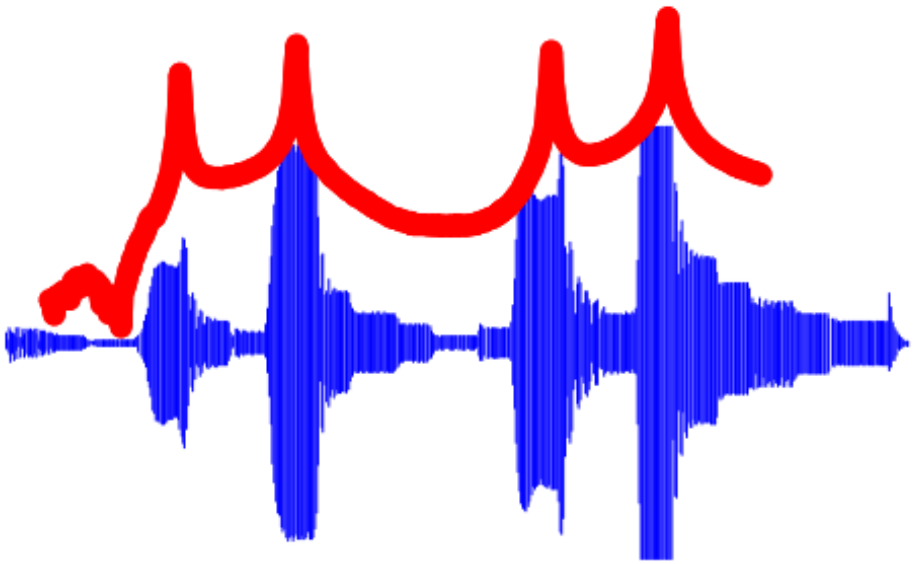

Figure 2.4: Overlay of Time and Frequency Response Function [Avi14]

The simplest case is a single-degree-of-freedom system composed of a mass m attached to a spring k and damper c as previously seen in Figure 2.1. Its equation of motion under an external force $f(t)$, including the damping factor c, is:

$$m\ddot{x}(t) + c\dot{x}(t) + k\,x(t) = f(t) \tag{2.12}$$

For harmonic excitation $f(t) = F_0 e^{j\omega t}$, the steady-state response will be $x(t) = X_0 e^{j\omega t}$. Substituting this into the equation of motion and solving for the complex amplitude ratio X_0/F_0 yields the FRF:

$$H(\omega) \;=\; \frac{X(\omega)}{F(\omega)} \;=\; \frac{X_0}{F_0} \;=\; \frac{1}{-\,m\omega^2 \;+\; j\,c\omega \;+\; k} \tag{2.13}$$

This is the receptance FRF (force-to-displacement $[\frac{g}{Hz}]$) for the damped SDOF system. It can be rewritten in various forms, for example dividing numerator and denominator by the stiffness k gives:

$$H(\omega) = \frac{1/k}{1 - (\omega/\omega_n)^2 + 2j\zeta(\omega/\omega_n)} \tag{2.14}$$

where ω_n is the natural frequency as already defined in 2.1 and $\zeta = \frac{c}{2\sqrt{km}}$ is the damping ratio. At $\omega = \omega_n$, the denominator's real part vanishes ($k - m\omega_n^2 = 0$) and the response magnitude reaches a peak limited only by damping. Thus ω_n corresponds to the resonance frequency of the SDOF, where the FRF magnitude is maximal and phase shifts by 90°[Irv00]. Equation 2.14 encapsulates the dynamic stiffness of the system in the denominator: $k - m\omega^2 + jc\omega = 0$ defines the frequencies where the system's impedance goes to zero (i.e. infinite response, in the absence of damping). In the low-frequency limit ($\omega \to 0$), the spring's stiffness dominates and $H(\omega) \approx 1/k$ (the static compliance). In the high-frequency limit, the inertial term $-m\omega^2$ dominates and $H(\omega) \to 0$ (the mass appears "infinitely stiff") and between these extremes, near ω_n the system transitions through a resonant peak where damping controls the amplitude. Figure 2.5 shows an example of the considerations just done and the different areas of influence are highlighted. As previously described in modal analysis in section 2.1, real structures have many degrees of freedom. Considering an n-DOF linear system (for example, a discretized structure or an n-mass system), the equations of motion in matrix form (neglecting damping) are as explicated in Equation 2.6, with the addition of the forcing factor:

$$M\ddot{x}(t) + Kx(t) = f(t) \tag{2.15}$$

where $[M]$ and $[K]$ are the mass and stiffness matrices (size $n \times n$), and $f(t)$, $x(t)$ are the force and displacement vectors (size n). For a set of harmonic forces $f(t) = \mathrm{Re}\{\mathbf{F}e^{j\omega t}\}$ applied (potentially at multiple

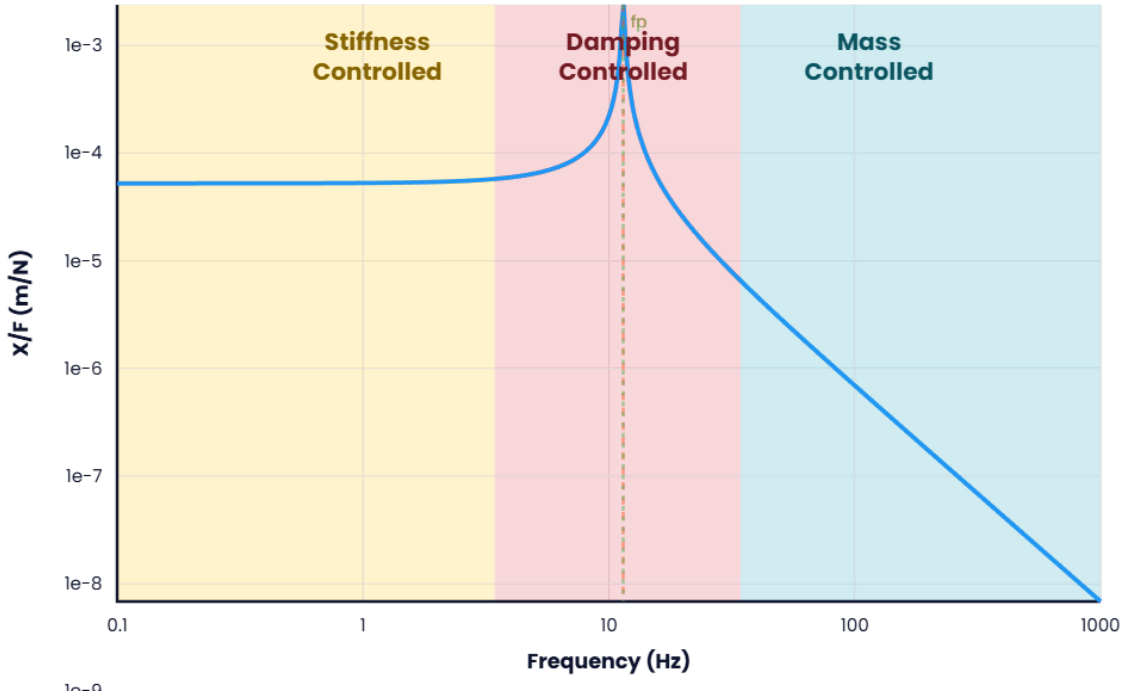

Figure 2.5: Variables Predominant in each FRF area [Ras]

coordinates), the steady-state response will be $x(t) = \mathrm{Re}\{\mathbf{X}e^{j\omega t}\}$. Substituting harmonic motion $\mathbf{X}e^{j\omega t}$ in Equation 2.15 gives the dynamic equilibrium in the frequency domain:

$$(K - \omega^2 M)X = F \tag{2.16}$$

The matrix $[Z(\omega)] = [K] - \omega^2[M]$ is known as the dynamic stiffness matrix. Except at frequencies ω equal to a natural frequency of the system (which make $[Z]$ singular), this matrix can be inverted. Thus the solution is:

$$\mathbf{X} = [Z(\omega)]^{-1}\mathbf{F} \tag{2.17}$$

The matrix $[H(\omega)] = [Z(\omega)]^{-1}$ is the FRF matrix for the MDOF system. Its elements $H_{ij}(\omega)$ give the displacement response at coordinate i due to a unit-force applied at coordinate j (as a function of frequency). Each element is a complex function of ω, generally with multiple resonance peaks corresponding to the system's natural frequencies. The diagonal elements $H_{ii}(\omega)$ are driving-point (or point) FRFs, measuring response at the same location as the force input; the off-diagonals $i \neq j$ are cross FRFs, measuring the transfer of force at one location to motion at another. Notably, for linear structures with symmetric mass/stiffness (no

coupling to non-measured DOFs), the FRF matrix is symmetric: $H_{ij} = H_{ji}$. An example of a single element of this matrix is given in Figure 2.6, while an overview of a possible complete FRF matrix is shown in Figure 2.7, showcasing the symmetry of response in a symmetric plate, such as the one already used for Figure 2.3 and Figure 2.4.

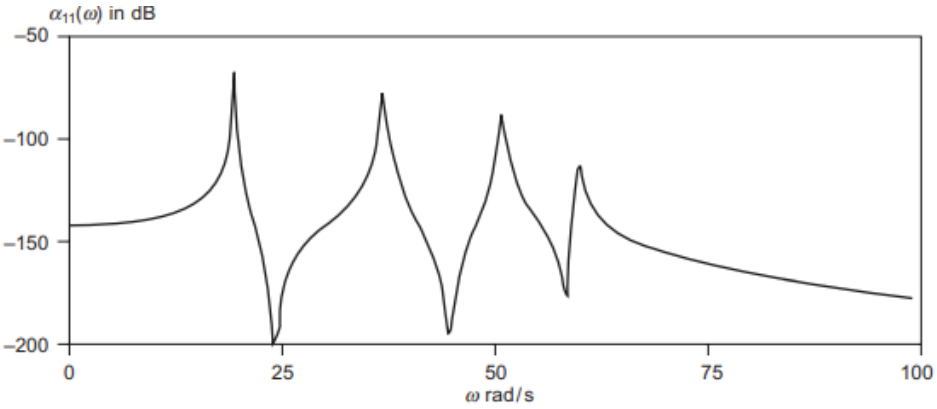

Figure 2.6: Single H_{ii} Element Magnitude [HF01]

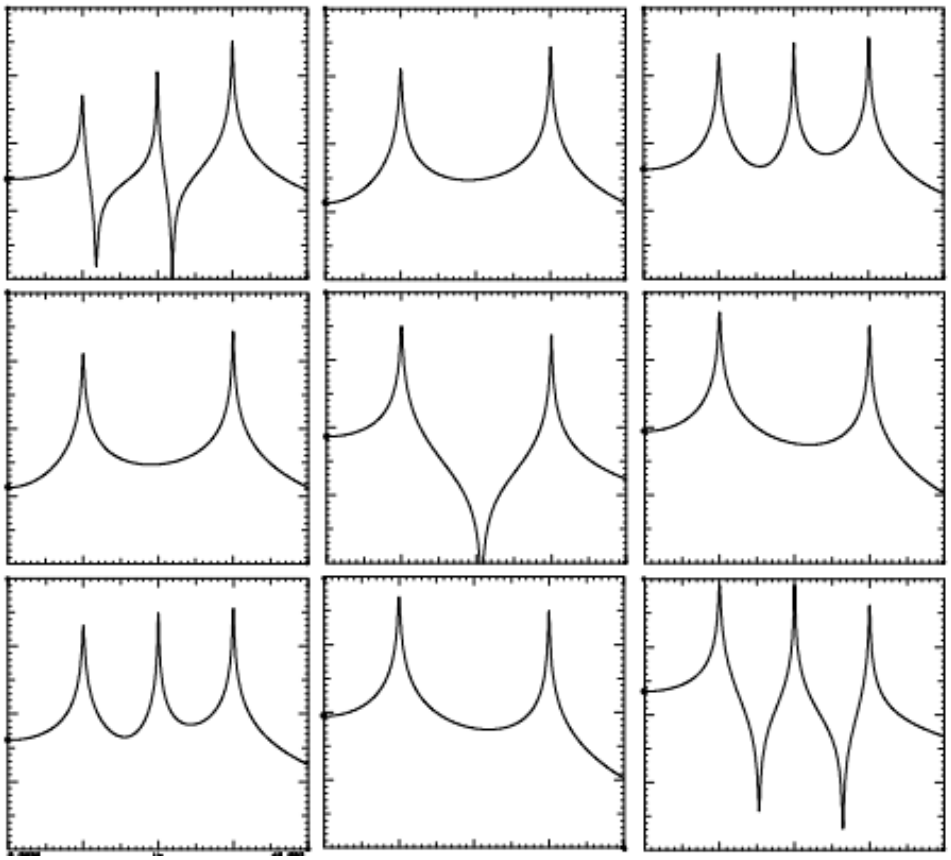

Figure 2.7: Complete H Magnitude Matrix [Avi14]

This reciprocity means that exciting point j and measuring at i yields the

same FRF as exciting at i and measuring at j. In practice, reciprocity allows flexibility in testing (e.g. one can either rove the hammer or the sensor). Physically, each resonance of the MDOF system will appear as a peak in all FRF elements, albeit with different amplitudes depending on the mode shape. When $i = j$, a driving-point FRF typically starts at the static compliance $1/k_{ii}$ at $\omega = 0$ and tends to zero as $\omega \to \infty$, with prominent peaks at each natural frequency (Figure 2.6). Each FRF element $H_{ij}(\omega)$ can be expanded in terms of the system's modes (eigenpairs). For an undamped system, one can show:

$$H_{ij}(\omega) = \sum_{r=1}^{n} \frac{\phi_i^{(r)} \phi_j^{(r)}}{(k_r - m_r \omega^2)} \tag{2.18}$$

where $\phi^{(r)}$ is the r^{th} mode shape vector normalized with modal mass m_r and $k_r = m_r \omega_r^2$ (with ω_r the r^{th} natural frequency). This modal summation form of the FRF highlights that each mode contributes a partial fraction term, producing a resonance (pole) in H_{ij} near ω_r. With damping included (assuming classical damping for simplicity), the modal FRF expression generalizes to:

$$H_{ij}(\omega) = \sum_{r=1}^{n} \frac{\phi_i^{(r)} \, \phi_j^{(r)}}{m_r \left(\omega_r^2 - \omega^2 + 2j\zeta_r \omega_r \omega\right)} \tag{2.19}$$

where ζ_r is the damping ratio of the r^{th} mode. This formula shows that the resonance peaks in $|H_{ij}(\omega)|$ occur near $\omega = \omega_r$ (slightly shifted if damping is non-negligible) and that the height (amplitude) of each peak is inversely proportional to the damping $2\zeta_r \omega_r m_r$ and also scaled by the coordinates' modal participation $\phi_i^{(r)} \phi_j^{(r)}$. Thus, by examining the FRF matrix of a structure, one can extract its modal parameters: natural frequencies (peak locations), damping ratios (peak widths), and mode shapes (relative amplitudes of peaks across different FRF channels). This process, called **Curvefitting** or **Modes Extraction** is necessary during test data extraction to obtain modal information from accelerometers placed during testing.

The phase $\gamma(f)$ instead indicates the lag or lead of the response relative to the input force. At very low frequencies (quasi-static loading), most structures act stiffness-dominated, so the displacement response is in phase with force (phase $\approx 0°$). At very high frequencies, inertia

dominates, so the acceleration is in phase with force (displacement is 180° out of phase, indicating force and displacement in opposite directions). Near a resonance frequency, the response transitions from being stiffness-controlled (in-phase) below resonance to being mass-controlled (out-of-phase) above resonance, passing through a 90° phase lag at the exact resonance (for a lightly damped SDOF). Damping affects the phase gradient and peak sharpness: higher damping flattens the resonance peak and reduces the abruptness of phase change [HF01].

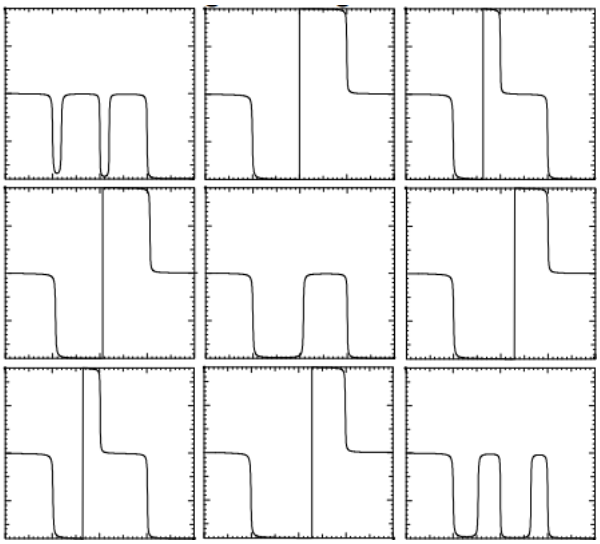

Figure 2.8: Phase Changes Associated with Resonance Peaks [Avi14]

An analytical approach in describing gain and phase of an FRF can be included evaluating its real and imaginary parts as:

$$|H(f)| = \sqrt{Re(H)^2 + Im(H)^2} \qquad \gamma(f) = tan^{-1}(\frac{Re(H)}{Im(H)}) \tag{2.20}$$

Lastly, it is possible to observe anti-resonances (minima in the FRF magnitude) at frequencies between resonances in transfer FRFs. An anti-resonance represents a frequency where the output response cancels out due to contributions from multiple modes which is effectively a zero of the transfer function for that input/output pair. The locations of anti-resonances relate to the dynamic interaction between modes, in particular it is needed that the imaginary part of the FRF for sequential modes have the same sign. If they have different signs than a saddle exists between those modes instead.

2.1.2 Operational Modal Analysis

Acquiring data directly in operative conditions or testing without acquiring input spectrum data, for example due to sensors unavailability or missing costly components, results in the so called Operational Modal Analysis(OMA). Due to missing input data, classical Frequency Response Functions (FRFs) and the corresponding transfer matrix $\mathbf{H}(\omega)$ cannot be formed directly. Instead, OMA techniques utilize statistics, such as the output power/cross-spectral density matrix $\mathbf{S}_{yy}(\omega)$, correlation functions, coherence, transmissibility functions, and modal indicators computed from output spectra [PD01]. OMA methods can be broadly grouped as:

- **Frequency-domain, non-parametric techniques**, such as Frequency Domain Decomposition (FDD) and enhanced variants (EFDD), which use the Singular Value Decomposition (SVD) of $\mathbf{S}_{yy}(\omega)$ to separate modal contributions and estimate mode shapes [PD01].
- **Time-domain, parametric techniques**, notably Stochastic Subspace Identification (SSI), which fit a stochastic state-space model directly to the measured outputs and then recover modal parameters from the identified system matrices [PD01].
- **Correlation-based approaches** (e.g., NExT-ERA), where cross-correlations of ambient responses are interpreted as impulse-response-like free decays that can be processed with realization algorithms such as ERA [JCL95].

A key limitation of OMA is that the identified mode shapes are only determined up to an arbitrary scale factor (and sign/phase). Without measured forces, straightforward mass-normalization is not possible, which prevents direct estimation of modal masses/participation factors and inhibits assembling a fully scaled FRF matrix $\mathbf{H}(\omega)$ from the operational modal model. The Transfer Functions (TF), between input and output, without the mass-information can be computed with OMA available data. When scaling is required, additional information or interventions must be introduced, for example mass-perturbation (mass-change) strategies, or combining OMA mode shapes with a correlated finite-element mass matrix / model updating to recover scaling factors [YS17; Ber04].

2.2 Testing

Modal testing is an experimental process used to determine a structure's dynamic characteristics (its modal parameters) by exciting the structure and measuring its vibrational response. In essence, it consists of a set of controlled tests to build a mathematical model of the structure's dynamic behavior. The structure is excited, usually through an impact hammer or electrodynamic shaker to stimulate its natural vibration modes, and sensors (typically accelerometers) record the resulting vibrations. The measured accelerations, in case of accelerometers chosen as sensors, are than post processed along with the input levels provided to the structure under test, whenever input recordings are available through a force sensor on the modal hammer or a force transducer at the shaker tip. Post processing usually includes the creation of FRFs and curvefitting the same, in order to obtain the principal modal parameters of the item under test, such as damping, natural frequencies and mode shapes. The resulting "modal model" allows visualization of the vibration mode shapes and provides a basis for predicting the structure's response to dynamic loading. In practical terms, modal testing yields empirical data defining how a structure vibrates, which is essential for validating designs, troubleshooting vibration issues, and ensuring safety through possible fault detection. In the aerospace context, modal testing takes on critical importance as aircraft, and most importantly for this thesis spacecraft, are highly flexible structures operating under significant dynamic loads. In fact, modal testing is a required milestone in spacecraft certification as the vibrational environment, especially at launch, can be extremely hostile to a spacecraft design. As such its properties must be fully defined and verified to ensure compliance to standards and avoiding damage to both the payload and the launcher vehicle. Several requirements need to be met to demonstrate the compliance with standing rules and compatibility with the chosen launcher while avoiding coupling [ESA08]. Beyond certification, modal testing is conducted on components and entire structures to verify FEM and to check for any unforeseen resonances or structural weaknesses. It can be stated that the final purpose of modal testing in aerospace is to ensure that the real structure's dynamic behavior is well understood and aligns with design expectations, thereby guaranteeing safety and performance. Modal test data is also used to diagnose vibration or noise

issues, for example, modal analysis of a satellite structure can reveal a mode causing instrument jitter which can be detrimental for both imaging and telecommunications. Jitter affects images causing blurring and fake motions as visible in Figure 2.9, while it leads to signals delays or time variance with respect to an original clocked signal used as reference.

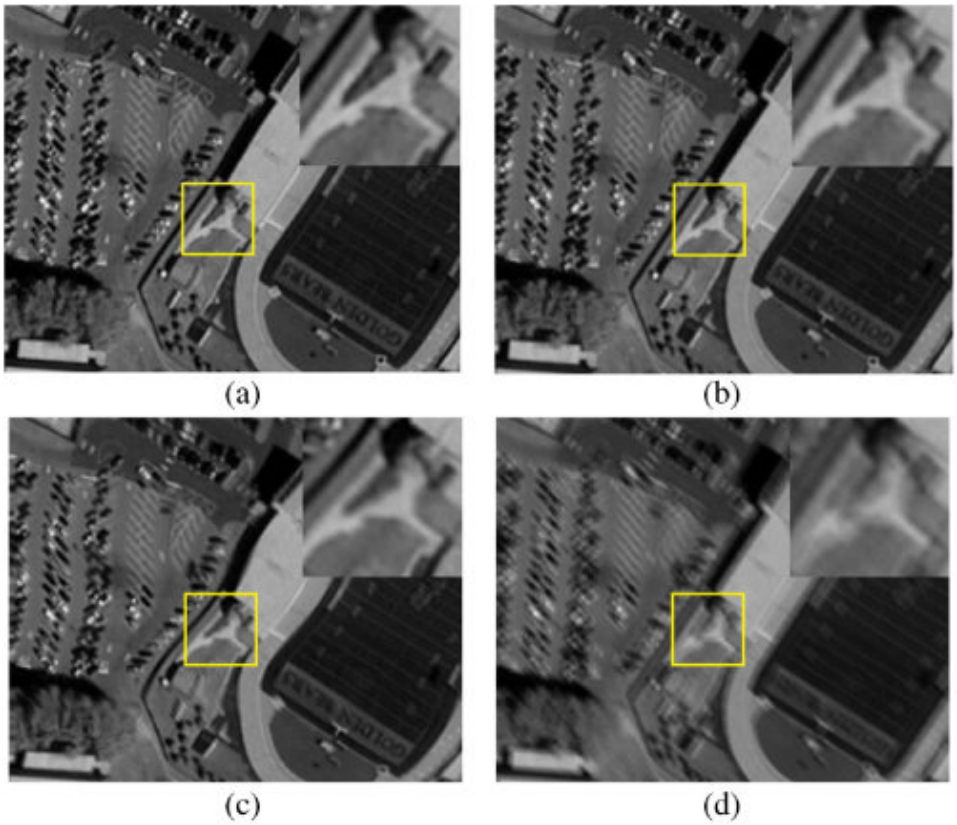

Figure 2.9: Jitter deformation in Satellite images [Liu+22]

Another application is using modal parameters as indicators of structural health, as changes in natural frequencies or mode shapes over time can signal damage (e.g. a crack or loose joint softening the structure). Modal testing is therefore applied to structural health monitoring, using in-situ sensors to detect changes in modal properties that might indicate fatigue damage. The modal data provide a baseline for comparison, and any significant deviations can trigger inspections. This process is performed both in small scale tests, checking to quickly verify if subsequent tests on the structure caused fatal damage or faulty connections, both on real operative and complex cases such as the International Space Station (ISS), in order to verify its fatigue tolerance and status after years of deployment [Fit+12].
Collecting high-quality response data is at the core of modal testing.

Transducers are placed on the structure to measure its motion (output) and the input force. The most common sensor for structural response is the accelerometer, which measures acceleration at a point on the structure. Accelerometers are popular because they are small, reasonably easy to install, and cover a broad frequency range. The acceleration data can be integrated (numerically) to obtain velocity or displacement if needed, but in modal analysis it's typical to work with acceleration/force FRFs (often called accelerance). The number and placement of sensors is a critical consideration: they must be sufficient to capture all the important mode shapes but may also cause small mass effects affecting the final outcome, especially if too many are used. Sensor locations are usually pre-determined manually basing on the anticipated mode shapes from the modal analysis performed on the FE model. A classic guideline is to place sensors such that each target mode has a distinct pattern of response among the measured points (to allow distinguishing modes). If sensors are too sparse or miss a part of the motion, a mode shape might be poorly characterized or even unobserved. In this thesis, specifically in chapter 5, a different numerical approach is explored, to automatically provide a selection of points suitable for accelerometer locations. The same will be used throughout the entire project to prove its functionalities. Other non traditional, often on-contact sensors, to carry out modal testing are also available. Although often very expensive compared with the basic mono-axial or triaxial accelerometer, providing different improvements and benefits such as avoiding mass-loading the structure or reaching hard-to-access areas. A few examples would be:

- **Laser Doppler vibrometers (LDVs)** can measure velocity at a point by sensing Doppler shifts in a laser beam reflected off the structure, allowing precise, contactless vibration measurements. An example of LVDs designed by the American National Institute of Standards and Technology is available in Figure 2.10;
- **High-speed camera systems** with digital image correlation or stereo-photogrammetry can measure full-field vibration shapes by tracking markers or patterns on the structure. It can also be used in real-time applications such as launchers take-off or in-flight measurements on planes, to check and measure the vibrations actively interesting the item under test, to later fully define the loads.

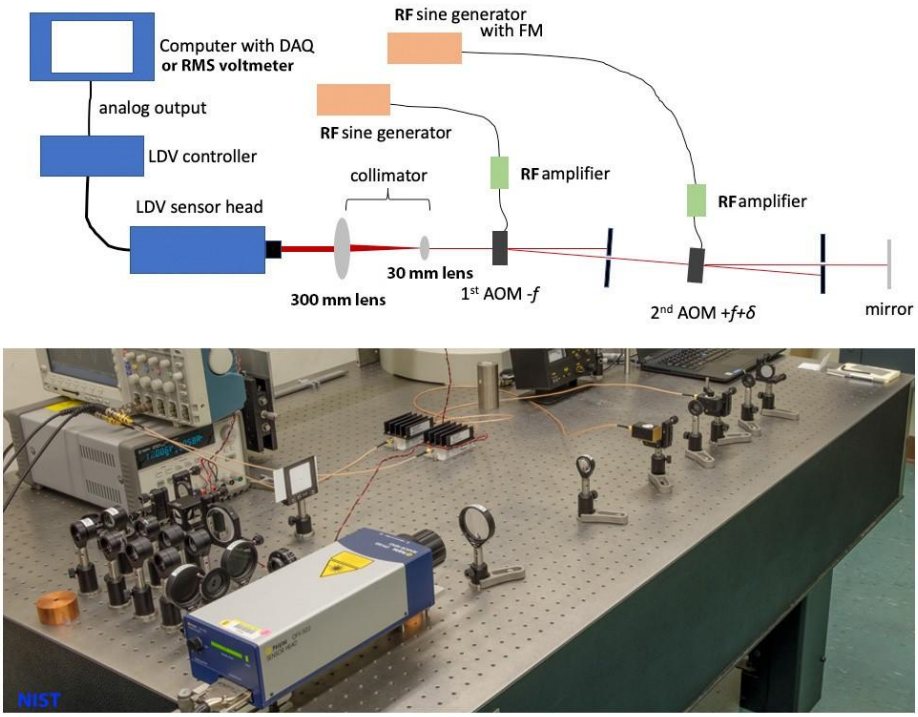

Figure 2.10: Laser Doppler Vibrometer with acusto-optics modulators [Chi21].

An example of a recording and different filters applied to it to magnify the results is visible in Figure 2.11.

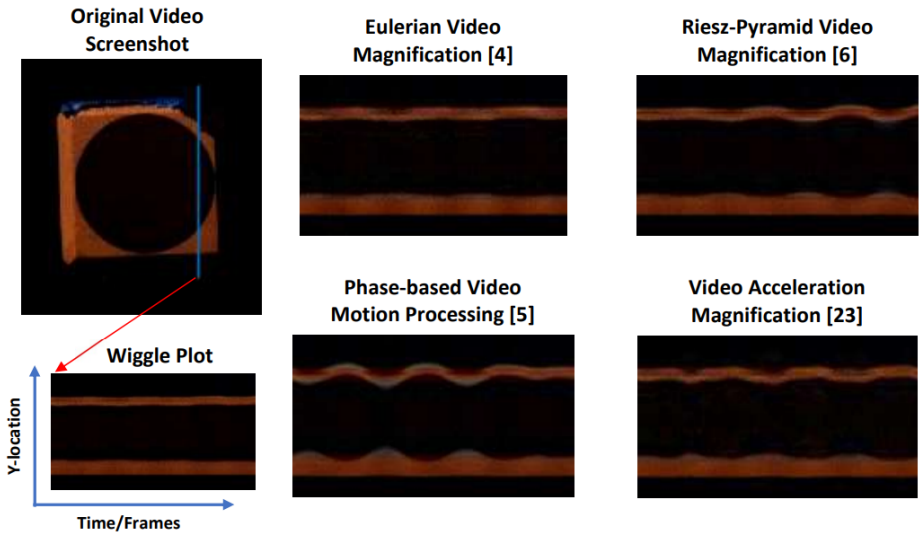

Figure 2.11: Results of a high-speed camera system recording and comparison of different magnification algorithms applied to the result [CS25].

Independently from the chosen sensor type, a data acquisition system records the signals, and typically an FFT analyzer or analysis software

computes FRFs from the input-output time histories. These items, often called spiders, receiving the sensors data are crucial in ensuring measurement quality, along with the cabling of both the sensors and the spider itself. The number and availability of such systems, as well as the possibility of using them in parallel, often puts a logistic strain on the actual number of sensors placed and actively recording on a structure. These limitations are often overcome through sensor roving, which requires both multiple tests and suffers from masses moving on the structure (the accelerometers) possibly contaminating data, especially for smaller components or subsystems. Ensuring high fidelity measurements involves considerations such as sensor calibration, adequate frequency resolution (sufficiently long sample time or fine resolution to clearly define narrow resonances), and using signal processing (windowing, averaging) to improve the signal-to-noise ratio. A high-quality modal test will also monitor coherence, which is a frequency-domain indicator of how much of the output is due to the measured input. Good coherence (near 1.0) at a resonance suggests that the measured output is reliably caused by the input force, whereas low coherence might indicate noise or non-linear behavior. Averaging is needed in order to measure coherence and to ensure a successful test campaign.
Importantly, modal tests can be conducted in various configurations:

- **Single Input Multiple Output (SIMO):** One exciter (input) is used, and multiple response points are measured simultaneously. The exciter might be moved to different locations in successive runs to excite different modes (if needed), but only one is active at a time. Historically, this was common – for instance, using one shaker attached to the structure and measuring many accelerometers.

- **Multiple Input Single Output (MISO):** An equivalent approach to SIMO achieved by roving an exciter, almost exclusively an impact hammer in this case, to many points while a single accelerometer stays fixed as reference. By reciprocity, this produces the same FRFs as SIMO although it can effectively be used for small components only or whenever a single accelerometer is sufficient/available.

- **Multiple-Input Multiple-Output (MIMO):** Multiple exciters (e.g. several shakers) excite the structure simultaneously at different points, and many outputs are measured. This approach has become

more practical with advanced control and analysis tools. The advantage of MIMO is that it can help excite all modes uniformly and can separate closely spaced modes. For large aerospace structures, MIMO is often beneficial, such as for example, exciting an airplane at several locations (fuselage, wing tips, tail) at once to ensure both symmetric and anti-symmetric modes get energy. MIMO testing also reduces test time since all data is acquired in one campaign rather than multiple setups. This practice is very suitable (and expensive) for large structures such as planes or other disciplines like civil engineering, but is overly accurate and over-dimensioned for smaller satellites and components such as those currently in the scope of this thesis. As such it won't be investigated further proceeding in the document.

Another very important aspect to monitor are experimental boundary conditions. Ensuring that the way the structure is fixed in test reflects the assumptions in analysis is key and necessary for obtaining meaningful and practical measurements. Free-Free conditions should also be recreated properly if required by the analysis and exclusively for hammer testing. Such conditions are obtained via cables and rubber bands properly dimensioned to sustain the item under test without stiffening it or at least minimizing such effects, removing de-facto the boundary effects making them negligible [Sch20].

2.2.1 Hammer Test

Impact hammer testing provides a quick, broadband input depending on the hammer's tip hardness: a hammer strike imparts an impulse force, effectively exciting a wide spectrum of frequencies at once. This results in a free vibration decay of the structure containing all modes, which can be captured and transformed (via FFT) to obtain FRFs. Hammer tests are very efficient for smaller structures or when a quick check of modal properties is needed. On larger aerospace structures, or when more controlled input is required, shaker excitation is common. Hammer Testing can be performed in both free-free configuration, which can be achieved through a system of strings and bands strongly reducing the boundary effects on the test and as such providing much more reliable data to effectively build the FRF matrix $H(\omega)$. During an hammer test it is also practically viable to do both sensor roving (if needed) and hammer

or input roving, which can't usually be achieved in shaker testing. A quick overview of which different part of the H(ω) matrix is being built by performing roving input or roving accelerometer is provided in Figure 2.12. In The real setup used will be described in section 6.2 and it will use both

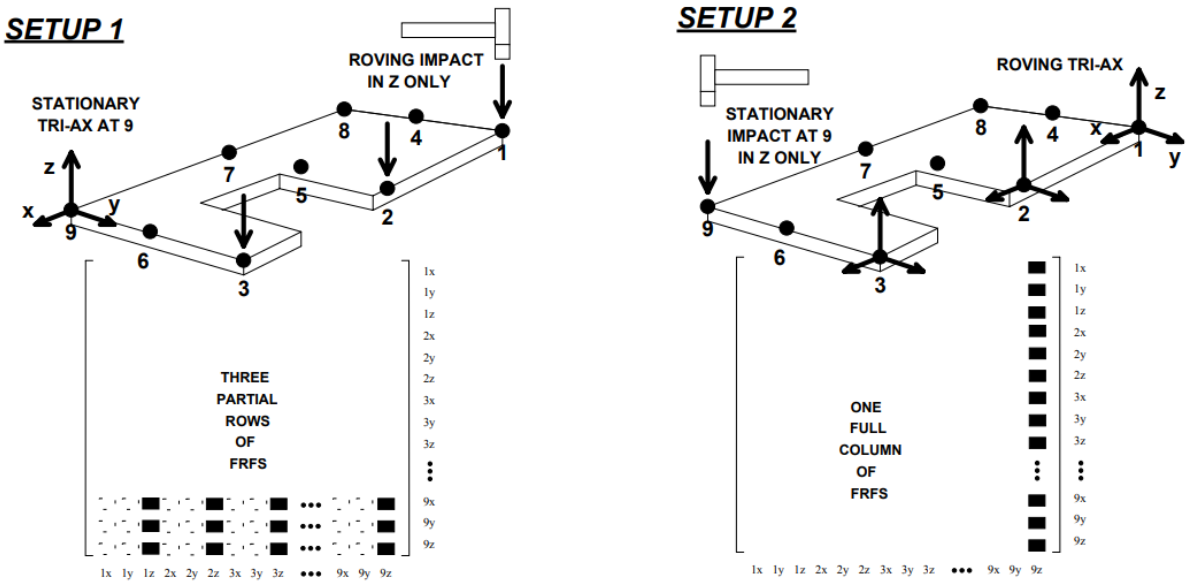

Figure 2.12: Roving Hammer vs Roving Accelerometer [Avi14]

roving of accelerometers and hammer in different configurations to obtain several useful FRFs (H(ω)) matrices. It should also be stated that the choice of the hammer tip is a very important point to ensure all modes of interest are visible in the acquired data, increasing the hardness of the tip may excite modes at higher frequencies but may also lead to poor analysis of lower frequency modes.

2.2.2 Shaker Test

Electrodynamic shakers can apply a known force over time, often a broadband random or swept sine signal, allowing the test to systematically cover the frequency band and even dwell on resonances if needed. Standard practice is to begin with low-level excitation and gradually increase force to ensure the structure's response is linear (checking that resonance frequencies don't shift with amplitude, which would indicate nonlinearity). The chosen excitation method should produce a high signal-to-noise ratio in the measurements and adequately excite all modes of interest. For example, if certain modes are missing in initial data, the test may need to reposition sensors or adjust the input spectrum to better

stimulate those modes. Measuring the driving-point FRF (the point where input is applied and output measured at the same location) at least at one or more locations is crucial for scaling mode shapes (to obtain consistent scaling) and also helps in identifying if any modes were missed. A force transducer is also needed if available in order to measure the input force provided to the item under tests, else the test will provide operational modes which can be used to create FRFs dimensionally acceleration over acceleration, effectively losing the mass information (and scaling) as already discussed in section 2.1.2. Lastly it is worth noting the difference between the data acquired from a basic impact testing and a shaker test, in particular while it may be easy to implement a roving input with a modal hammer it is not viable with a shaker and as such the second only provides a single column of the FRF matrix per test (which is notably enough to compute the full matrix) while roving the hammer provides a single row of the matrix. It is important to notice that theoretically the 2 outputs provide the same result as both a full row and a full column are enough to write the full matrix due to reciprocity and symmetry in the matrix itself. In Figure 2.13 a simple example on a 3 points cantilever beam is provided to better visualize the concept.

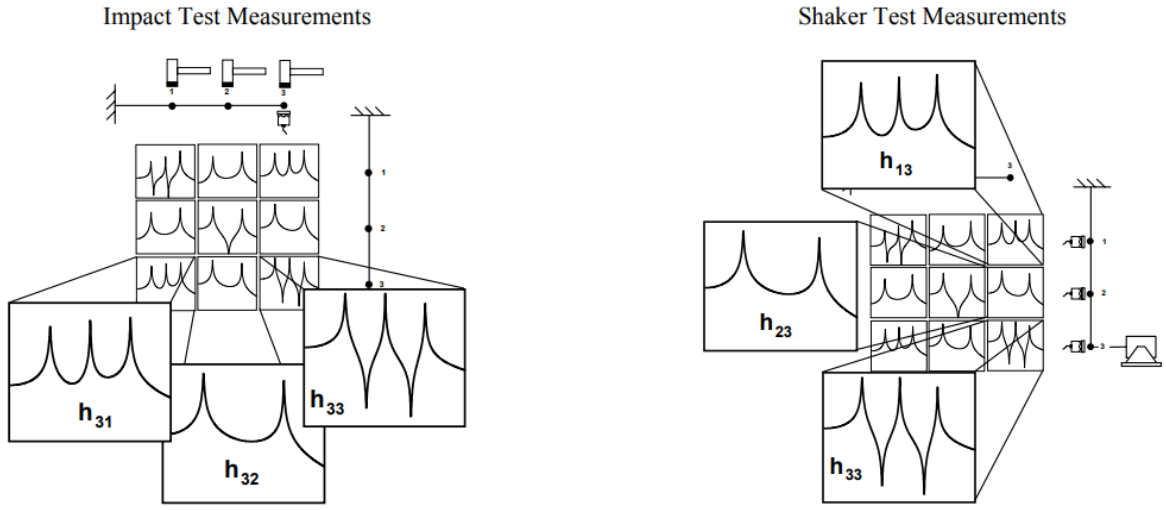

Figure 2.13: Hammer and Shaker testing on cantilever beam [Avi14]

2.3 Correlation

Correlation is the process of error determination and later, through different means, reduction in order to assess the actual differences between

the modal analytical model built and analyzed mathematically on software and the real, built and produced physical model. In this chapter the different mathematical tools used to evaluate the error in the system are described to provide the reader with the used metrics and functions later applied to the real cases in study. In general test data is considered to be the reference high-fidelity data on which to base both test-analysis error estimation and later optimization targets to be achieved. The aforementioned assumption is surely strongly reliant on the test reliability and a good combination of sensor placement, input provided and data postprocessing. Lastly, regulatory bodies such as ESA and NASA have strict requirements on the process of analytical-test models correlation along with specified ranges of acceptability for all the metrics later described [ESA08].

2.3.1 Frequency Error

Frequency error can, theoretically and numerically be easily computed, but this can only be performed after it has been assessed that the analytical mode I am evaluating is being compared with its truly respective mode measured during test. This action, often identified as mode tracking or mode pairing consists in using several tools (later detailed in sections 2.3.2 and 2.3.3) like MAC and COC to compare the mode shapes of different modes under study. This step is crucial because there may be important frequency shifts over one or several modes possibly inverting the order in which they appear (this is more likely the closer two natural modes are in the frequency range) and it would be a grave mistake to compare for example a bending mode with a totally different shifting mode. Once the modes are paired the frequency error can simply be computed as:

$$E_{rel} = \frac{\lambda_{aj} - \lambda_{mj}}{\lambda_{mj}} \tag{2.21}$$

where subscript "a" stands for analytical modes and subscript "m" stands for measured or tested modes [Cal97].

2.3.2 Modal Assurance Criterion

The Modal Assurance Criterion (MAC) is a mathematical technique used to evaluate the degree of correlation between two arbitrary mode shapes.

It is defined as:

$$MAC_{jk} = \frac{|\phi_{mj}^T \phi_{ak}|^2}{(\phi_{ak}^T \phi_{ak})(\phi_{mj}^T \phi_{mj})} \tag{2.22}$$

Its value ranges from 0 to 1 where 1 means that one mode shape is a multiple of the other and 0 means that there is no correlation at all between the chosen modes. MAC is a powerful tool to perform mode pairing as it is mass-independent and as such doesn't require to compute the system matrices, which is a very computationally heavy task especially for real life systems, often analytically modeled in FEMs with millions of degrees of freedom. Moreover due to its formulation it is also scaling invariant meaning that unscaled operational modes can also be correlated using MAC despite them not being mass-normalized and as such not suitable for other correlating methods such as COC.

2.3.3 Cross Orthogonality Check

The Cross Orthogonality Check (COC) is another mathematical tool used to evaluate the correlation between measured and analytical modes or in general any 2 chosen modes. It is defined as:

$$C = \Phi_m^T M \Phi_a \tag{2.23}$$

As it is clearly visible in the COC calculation the mass matrix, ideally in its entirety, is needed to compute the matrix components. In reality only a reduced version of the mass matrix (M_r) is computed and used in the COC formulation due to the testing point being entire order of magnitude less in number than the mesh points of the analytical model. Once again C can vary from 0, showing no correlation between modes, up to 1 where the modes are only scaled up to a scalar constant (or, as stated before in chapter 2.3.2, they are multiple of each other). It is also possible and valuable to compute an AUTO-COC using the test modes measured.This is done in order to approximate the test mass element needed for normalization of the eigenvectors, this process is done using the Analytical Reduced Mass Matrix as it is simplier and proven to be sufficiently effective [Cal97]. The following equations are used:

$$A_{ij} = \phi_{mi}^T M \phi_{mj} \tag{2.24}$$

$$\phi_{mi} = \frac{\varphi_{mi}}{m_{mi}^{1/2}} \tag{2.25}$$

where φ_{mi} is the measured mode shape before normalization and m_{mi} is the associated estimated measured mass, computed as:

$$m_{mi} = \varphi_{mi}^T M \varphi_{mj} \tag{2.26}$$

In case the eigenvectors are mass-normalized and orthogonal with respect to the mass matrix than the solution should be the unit matrix.

2.4 Sensitivity Analysis

Sensitivity Analysis is the process of evaluating how the variables chosen for optimization affect the eigenvalues or eigenvectors of the modal model. As such, the purpose of the sensitivity analysis is to determine:

$$\frac{\partial \lambda_i}{\partial x_i} \qquad \frac{\partial \phi_i}{\partial x_i} \tag{2.27}$$

These derivatives represent how the chosen variables impact our final metrics and are used to evaluate potential optimization candidates and rank them in order to choose a minor number of more effective candidates to optimize the model. This process is necessary both to evaluate the variables chosen as candidates, both to minimize the computational load of the process which, for large models, can be a strain and a cost. Sensitivities are also used later on in the optimization process as weights in the updating loop. In order to obtain the sensitivities a loop is created in which the analysis are ran with very small changes to the chosen variables in turn, allowing for determining the effective changes of the single variable to the entire model. Variable selection in the first place is a crucial task which is performed first with engineering judgment and than refined through sensitivity analysis. It is key to notice that in order to aid the engineer in the selection the modes are visualized and kinetic energy per node is computed highlighting the areas most affected by modes, both locally and globally. The parameters evaluated during selection are the FEM components and properties in FEMAP and can be materials properties(E,λ,G), elements definitions(t,A,I,...) and connections(stiffness,type).

State Of The Art

3.1 Bibliographic Research

The correlation process of FE models using modal data is an active topic of research in the structural and vibrational field of work, as it represent a key aspect in ensuring reliable and trustworthy models while minimizing the testing time and economical effort. Multiple papers and thesis, coming from both aerospace studies [Cal97][Fit+12] and civil engineering [Sve+21][Beh+15], were used by the author as reference to set up its thesis work.
Four different approaches to modal analysis were explored in these papers, in particular:

- [Cal97] **Finite Element Model Updating in Structural Dynamics using Design Sensitivity and Optimisation:** represents a deterministic view presented by Calvi's work on model updating using design sensitivity and optimisation. As described in that thesis, the objective was to exploit optimisation tools to create an error-localisation and updating procedure that minimizes the discrepancy between experimental and analytical modal data, with particular attention to large FE models and demanding mode-shape correlation requirements.
  Moreover, this approach is presented as the semi-automatic adjustment of a parameterised FE model through objective functions built from modal residuals, with candidate variables selected through sensitivity analysis and engineering judgement. The emphasis is therefore not on direct matrix correction, but on updating physically meaningful parameters under bounds and constraints.
  A key aspect of the Calvi approach is the use of sensitivities not only to drive the optimisation, but also to support parameter selection and

error localisation. The underlying idea is that the parameters chosen for updating should be those that significantly influence the eigenfrequencies and mode shapes targeted in the correlation process. The proposed methodology lays an essential foundation for this thesis research but it is also improved upon by strongly increasing the automation in the procedure, while improving the test results post processing and their direct inclusion within the procedure, as detailed in subsection 7.4.3. Moreover, an ulterior study described in subsection 7.6.1, regarding strict physical boundaries in the optimization process expands on the idea introduced in Calvi's Thesis of physical boundaries and retaining the physical meaning of the correlated structure.

- [Sve+21] **Improved finite element model updating of a fullscale steel bridge using sensitivity analysis:** this study by Svendsen et al. remains within the deterministic approach, but it refines it in a way that is especially relevant for civil structures. Their updating framework uses measured natural frequencies and modal assurance criterion (MAC) values as outputs in a sensitivity-based calibration procedure, with the FE model parameterized through uncertain stiffnesses, densities, masses and support conditions. This structured search is meant to balance modal improvement against physical realism, in fact, this paper excludes some identified modes from the updating algorithm and uses them as control modes, thereby checking whether the updated model improves only the fitted subset or the broader modal description of the IUT. Frequencies are given greater weight than MAC values, and the final solution is selected not simply because it minimizes the objective function, but because it also yields acceptable parameter values. The contribution of this paper to this thesis is hence important for the development of the updating methodology, in particular the effective inclusion of sensitivity and boundaries in the optimization process.
  The thesis expands on this paper adapting its strengths to fit the particularities of space structures and the available data from the different tests carried out as described in chapter 6.

- [Fit+12] **INTERNATIONAL SPACE STATION MODAL CORRELATION ANALYSIS:** offers a different perspective as

the main purpose is not extensive parameter updating, but validation of a large integrated model for on-orbit loads verification. The ISS analytical model is assembled from ground-test-verified component FEMs, including component mode synthesis models, and adapted as closely as possible to the actual orbital configuration and interfaces. Modal correlation is then used to assess whether the model is sufficiently accurate for operational and verification purposes. The paper notably explains how test and analytical mode shapes are compared mainly through MAC, while cross-orthogonality is discussed as a standard correlation tool whose usefulness depends on having sufficiently rich spatial measurement coverage. This NASA study provides the thesis with a detailed definition of the metrics adopted throughout the method to assess the correlation of the IUT, visible in subsection 7.4.2, while giving a useful and alternative insight on possible different uses of the correlation and updating procedure in damage identification and structural health assessment.

- [Beh+15] **Hierarchical Bayesian model updating for structural identification:** offers a completely different approach to modal updating proposing a probabilistic method instead of the deterministic one explored in this thesis. Their central argument is that a single deterministic parameter vector is often inadequate for structures, because modal properties vary across tests due not only to measurement and estimation errors but also to true changes induced by temperature, excitation level or other ambient effects. The proposed framework therefore treats updating parameters as random quantities and aims to estimate both their values and their variability. Even though this approach is not explored further in this thesis it gives an important insight on different updating methods approaching the problem from a completely different perspective and proposing a radically different solution to the correlation problem.

The correlation methodology developed, detailed in chapter 7, is a deterministic approach that implements a sensitivity based optimization procedure. Test data is automatically included in the iterations, and the optimization is constrained by physics-driven boundaries. The methodology is also agnostic to the studied models, enhancing adaptability and enabling the reusability of both the procedure and the developed tool.

Items Under Test

4.1 HAWK PLUS

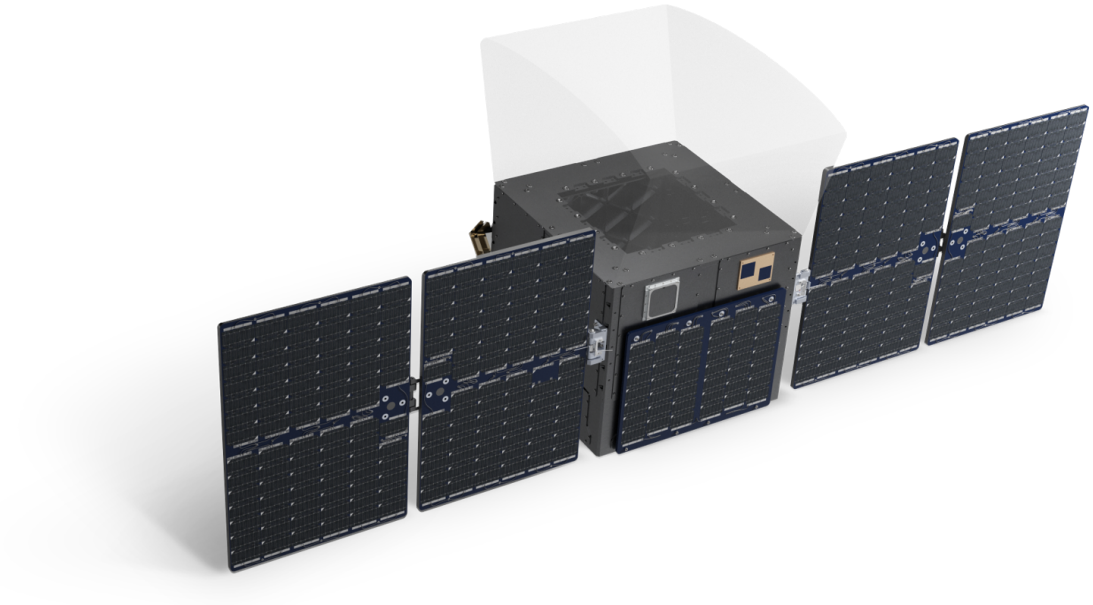

Figure 4.1: HAWK PLUS Render

4.1.1 Design Philosophy

In development at Argotec, HAWK PLUS is the modular micro-satellite platform that combines standardization and flexibility to enable faster and cost-effective missions. The main design driver is modularity and industrialization, aiming at providing flexible, fast and easily customizable alternatives for many different missions. To fulfill such an achievement HAWK PLUS is studied and developed as a standardized platform built as an assembly of several different bays, each specialized and yet customizable

for mission specific requirements, such as Electrical Power System (EPS), Attitude and Orbital Control System (AOCS) and Avionics.

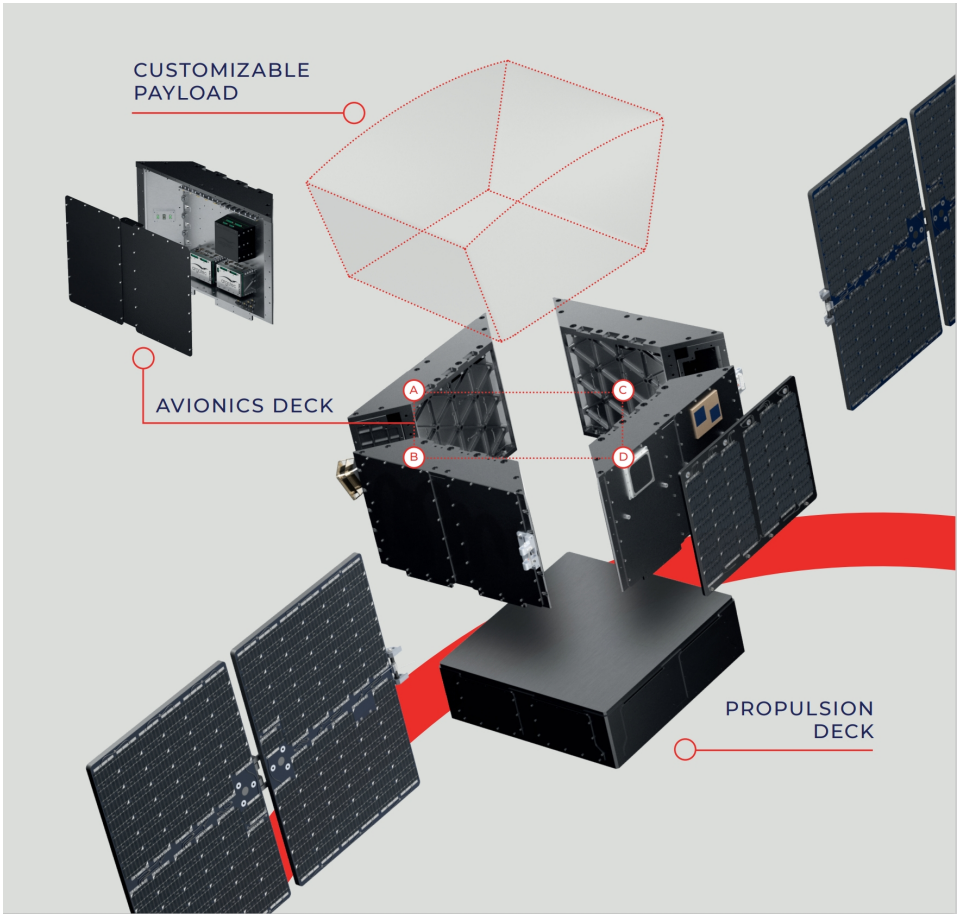

Figure 4.2: HAWK PLUS Brochure Showcase of the Different Bays [Srl25]

4.1.2 Structural Thermal Model

A satellite Structural Thermal Model (STM) is a non-flight, mechanically and thermally representative spacecraft model used to qualify structural and thermal design assumptions and modeled properties through environmental testing and model correlation prior to flight hardware acceptance [ESA23].As the definition above given by the ECSS details, the STM under test is a physical representation of the final platform which is thoroughly tested and, in this thesis, correlated to gain reliability on the digital twin developed and to verify analysis data and assumptions made during the FEM modeling phase of design. In order to test the STM both Hammer and vibe tests are performed. for the scope of this thesis both the hammer test data and the shaker tests will be considered This topic is

further studied in chapter 6.
In the STM several dummy masses are created in order to simulate the main subsystem which will be present in the final satellite. A dummy mass is a non-functional substitute introduced into a system in order to reproduce the relevant inertial properties of a real component without replicating its operational functions. It is designed to match, as closely as required, the total mass, the center of gravity, and, when necessary, the mass moment of inertia of the original part as well as the true interface and mounting points for proper integration.
A CAD representation of the STM without the Payload Dummy Mass is visible in Figure 4.3.

Figure 4.3: HAWK PLUS STM

4.1.3 HAWK PLUS Propulsion System Dummy Mass Model

The other main dummy mass in the HAWK PLUS STM is the propulsion system one. Two different versions of this dummy mass have been created starting roughly from the same components in different quantities and fixing conditions. The small configuration, visible in Figure 4.4, has been used in this thesis as a test item for both the initial phases of the code and the definition of the correlation algorithm. This choice is due to the relatively smaller size of the model and, consequently, reduced computational time in both the updating and modeling part of the algorithm. Lastly, the small configuration has been tested through a

resonance search using the shaker as later described in section 6.3. The

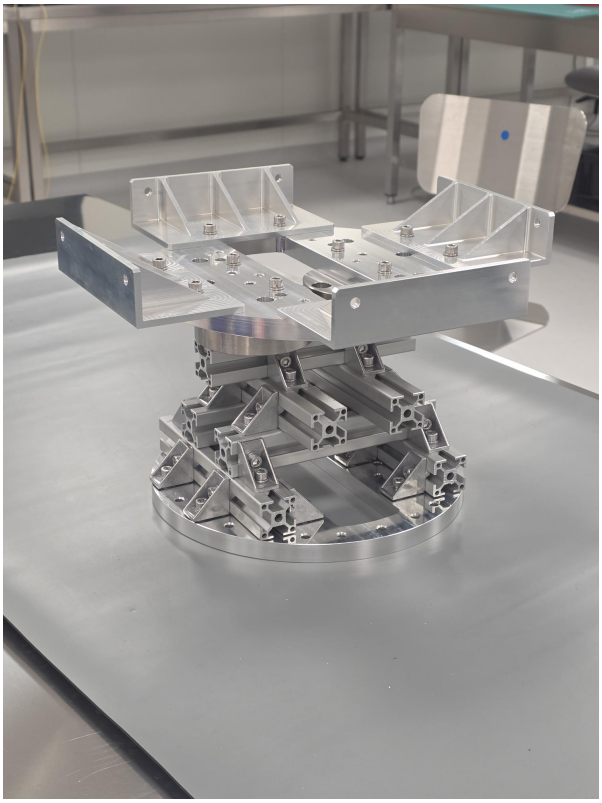

Figure 4.4: STM Propulsor Dummy Mass in Small Configuration

Propulsor Dummy Mass in Large configuration, visible in Figure 4.5, is mostly used inside the final STM configuration throughout all the testing phases, including the hammer test. As such, this configuration is to be considered a baseline for all further analytical models and testing processes.

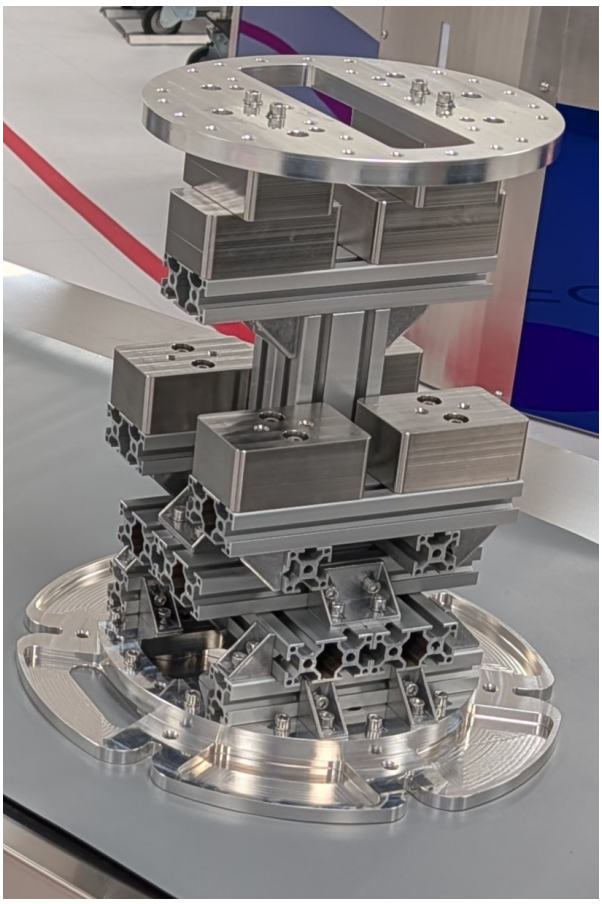

Figure 4.5: STM Propulsor Dummy Mass in Large Configuration

Testing Points Determination

5.1 Objectives

Testing Points Determination refers to the process of choosing the best places for accelerometers in the test model starting from the FEM analysis. Usually, this process is done manually by studying the deformed shapes visible as an output from a standard modal analysis, both in free-free and restrained conditions, and locating the best areas in which the most important modes are visible and trackable. This chapter of the thesis aims at showcasing an alternative, automated method, which provides possible sensor placement locations, knowing the FEM geometry and eigenvectors from the performed modal analysis.

5.2 Pre-Selection

In large-scale models, considering every point as a candidate can make the selection process unfeasible due to the overwhelming amount of data. Pre-selecting a smaller candidate set, through a so called candidate screening process or coarse selection, is often a decisive step to reduce computational time and resources, often turning an unsolvable problem into a solvable one. Several methods and algorithms for nodes pre-selection are available in literature and two have been selected: a geometrical based approach called voxelization and a physical approach based off mean kinetic energy per node.

5.2.1 Voxelization

A widely used and conceptually simple pre-selection strategy is voxelization: converting a continuous or irregular representation (mesh or point cloud) into a structured 3D grid of voxels, and then selecting

representative points per voxel (centroids for example). The underlying idea is to enforce spatial coverage and reduce redundancy by ensuring that densely sampled areas do not dominate the candidate pool purely due to discretization density. Thanks to this spatial spacing, it is almost impossible for the algorithm to choose contiguous points, depending of course on the size of the voxel with respect to the model main dimensions. In voxelization, the domain is partitioned into cubes of side length h (the voxel size). For each voxel, that contains at least one original point (in case of a point cloud) or intersects with the geometry/mesh, a representative is chosen, commonly the centroid of contained points, the nearest original point to the voxel center, or a boundary point if sensing must occur on surfaces. By construction, this reduces the candidate set from N to approximately the number of occupied voxels, which can be orders of magnitude smaller. The parameter h directly controls the trade-off: small voxels preserve spatial detail but yield more candidates; large voxels strongly compress the candidate set but may erase important geometric or physical features. An example of voxel sizing is shown in Figure 5.1.

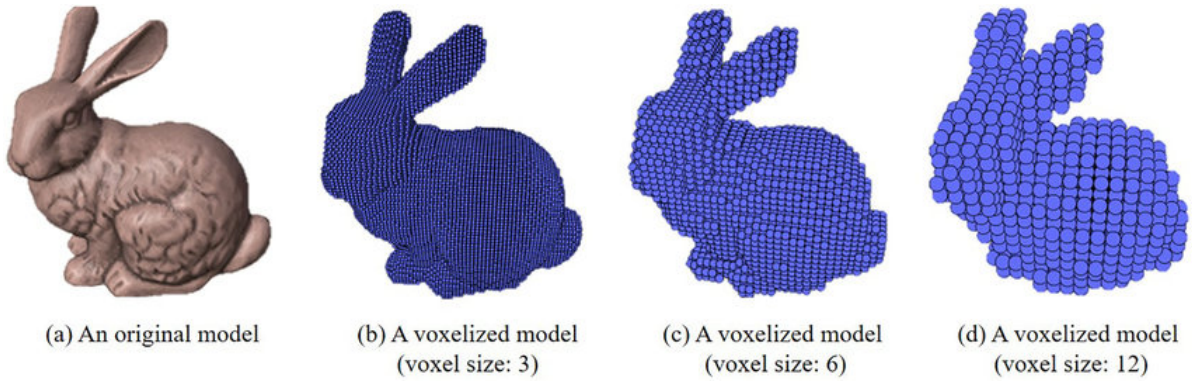

Figure 5.1: Different Voxel Sizes [Oh+21]

Voxelization has several practical advantages. It is fast (linear or near-linear time in the number of points), parallelizable, and easy to implement. It also provides a natural way to impose minimum sensor separation: selecting one point per voxel ensures sensors do not cluster too tightly. This is particularly valuable when later selection methods have diminishing returns for nearby points because their signals are highly correlated. This method can also incorporate constraints like "surface-only" selection by voxelizing only the surface point set or by retaining voxels intersecting the boundary.
However, voxelization is primarily geometry-driven and may be blind to

physics. If the most informative regions occupy small geometric volume—thin boundary layers, crack tips, sharp corners, interfaces, or localized sources, than uniform voxelization may under-represent them unless h is chosen very small everywhere, which dramatically increases the number of points countering all the other benefits listed above. A common refinement is adaptive voxelization, where voxel size varies by region: smaller voxels in areas of high curvature, near boundaries, or where gradients are expected to be high; larger voxels elsewhere. Such a refinement requires additional detail and a knowledge of the system dynamics defeating the automation purpose that drives the entire process. The optimal voxel size is iteratively determined evaluating the conditioning of the $\overline{\overline{\phi}}$ matrix, later defined in Section 5.3.

5.2.2 Kinetic Energy Method

A completely different, physics driven approach is the Mean Kinetic Energy (MKE) Method. The mean kinetic energy approach ranks candidate points by how much kinetic activity they exhibit over time and retains only the most energetic ones as candidates for final sensor placement. This selection is based on the consideration that the most energetic nodes are the most involved in the model dynamics and as such are good candidates for accelerometers measurements in order to properly visualize vibrations. Having a time series of velocity vectors $\mathbf{v}(x,t)$ at each spatial location x over a set of time snapshots $t_1, ..., t_T$, the kinetic energy density is defined as:

$$KEd = \frac{1}{2}\rho||v||^2 \tag{5.1}$$

where ρ is density (or an effective density in non-dimensionalized form). The mean kinetic energy at a point can be defined as:

$$MKE(x) = \frac{1}{T}\sum_{i=1}^{T}\frac{1}{2}\rho(x)||v(x,t)||^2 \tag{5.2}$$

The value per grid point is obtained through NASTRAN using built in calls and corresponding equation [MSC22]:

$$GPKE = \Phi_g^{mass} \otimes [M_{gg}\Phi_g^{mass}] \tag{5.3}$$

Where Φ_g^{mass} indicates that the mass-normalized eigenvectors are scaled so that the total grid point kinetic energy is scaled to be unity and the

operator $\otimes$ indicates term-wise matrix multiplication The values are scaled such that the total kinetic energy is 1.0 and the printed values are further scaled to be a percentage of the total [MSC22]. This metric is more complex and computationally expensive to measure but at the same time preserves the physical meaning of the search, including mass information in the selection process. Due to entire regions being usually active in the dynamics of the vibration modes, this selection methods is more susceptible to proximity bias, often localizing spatially close grid points. This aspect of the method makes it very suitable for a pre-selection of nodes but rarely fit to single-out the effectively best sensor locations and as such a new, different method must be implemented. The number of candidates preserved after the selection may vary and an optimum is defined by calculating the conditioning of the $\overline{\overline{\phi}}$ matrix, later detailed in Section 5.3.

5.3 Effective Independence Method

Effective Independence is an iterative method which ranks candidate sensor locations according to their contribution to the linear independence of the **target modal partition** [GS95]. The target modal partition matrix $\overline{\overline{\phi}}$ is an mxn matrix of eigenvectors where m represents the number of candidate sensor positions and n is the number of target modes of interest. For small subsystems or objects m can be equal to the points of the mesh and n to every corresponding mode. In larger, real-life models this simplification is not feasible, and as such, some pre-selection methods, as the ones described in previous section 5.2, must be performed to avoid $m = N$ (where N = DOF of the system), which would bring to an overwhelming computational load. Notably, not even every vibrational mode of a structure is evaluated as it would once again bring $n = N$, NASTRAN and other commercially available solvers automatically showcase only a limited number of eigenvectors, limiting the choice to a total amount of participated mass or to an user input arbitrary number. In this thesis however a large number of modes (~ 100) are demanded to the solver in order to accurately visualize and find the most participated ones. A filter is added to the Python code, automatically sorting the modes for mass participation over the 3 axis and choosing only a smaller number of high significance modes. In order to limit the number of sensor

candidates, an optimization iterative computation of $\overline{\overline{\phi}}$ conditioning is performed for both methods, as visibile in Figure 5.2 and Figure 5.3 for the Propulsion System Dummy Mass described in subsection 4.1.3. This process aims at compromising between having an acceptable conditioning number and a sensible number of points, upper and lower bounds for both voxel dimension and kinetic energy number of candidates are established in order to ensure both a sufficient discretization of the problem and a significant reduction of the selected points in order to run the EIM optimally.

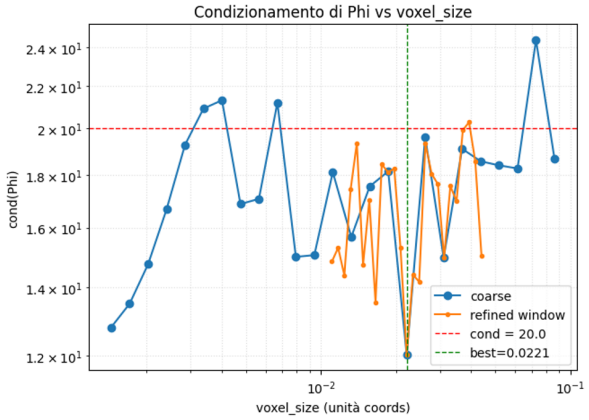

Figure 5.2: Voxel Conditioning

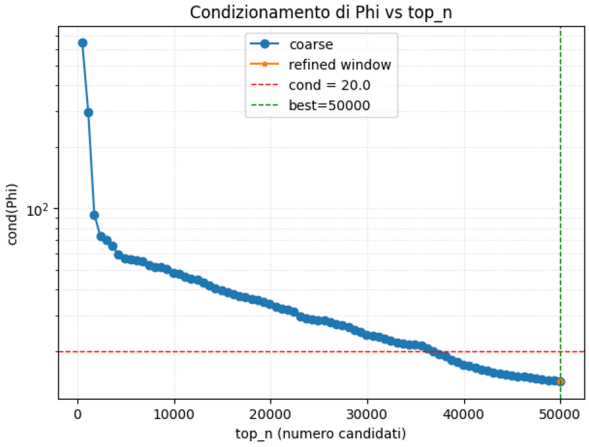

Figure 5.3: MKE Conditioning

The example shown leads, in the respective overall minima, to the following conditioning and matrix dimensions:

	Voxelization	Mean Kinetic Energy
Conditioning	12.03	14.19
Matrix Size	4428x33	300.000x33

Table 5.1: Conditioning and Matrix Size for different pre-selection optimizations

Once the $\overline{\overline{\phi}}$ is fully assembled than the method is computed starting from the definition of the **Fisher Information Matrix**(FIM):

$$FIM = \overline{\overline{\phi}}^T \overline{\overline{\phi}} \tag{5.4}$$

and the corresponding Eigen-problem Solution:

$$(FIM - \lambda)\psi = 0 \tag{5.5}$$

Since the columns of $\overline{\overline{\phi}}$ represent different modes they are linearly independent. Therefore, the eigenvalues of FIM are real and positive and

its eigenvectors are orthogonal. Due to these mathematical properties, it is possible to compute the **Association Matrix**, which represents the association of each column of the matrix with the corresponding eigenvalue:

$$G = [\overline{\overline{\phi}}\psi] \odot [\overline{\overline{\phi}}\psi] \tag{5.6}$$

where $\odot$ represents the term-by-term multiplication of matrix, also called Hadamard or Schur Product. The association matrix is than used as a map in order to compute the **Fractional Eigenvalue Distribution** for the set of calculated eigenvalues as:

$$F_E = G[\lambda]^{-1} \tag{5.7}$$

which indicates the fractional contribution of the i^{th} sensor location candidate to the j^{th} eigenvalue. Finally, once all the Fractional Eigenvalue Distributions are computed for each candidate, than the **Effective Independence Distribution** is defined as:

$$E_D = [\sum_{j=1}^{k} F_{E1j} : \sum_{j=1}^{k} F_{E2j} : ... : \sum_{j=1}^{k} F_{Esj}]^T \ \in [0, 1] \tag{5.8}$$

Which is an $mx1$ Column Vector in which the i^{th} term is the fractional contribution of the j^{th} sensor to the linear independence of the modal partitions. Once this process is completed and the E_D matrix computed, the lowest value is selected and discarded updating the selection candidates by removing that sensor from the list and progressing to the next iteration. The process can be performed for an accelerometer in all 3 directions or direction-based, discarding each time the direction of the sensor chosen. While the second approach can have interesting developments in the usage of mono-axial accelerometers, it also leads to a $\overline{\overline{\phi}}$ matrix 3 times bigger (as for each sensor all 3 translational directions are evaluated independently) and as such it is rarely viable for large scale models. Moreover, the availability in-situ of tri-axial accelerometers rendered such a detailed selection ineffective and virtually useless for the application of this thesis.

5.4 Results

5.4.1 Algorithm Testing - PS Dummy Mass Large Configuration

A first study conducted on the HAWK PLUS Propulsion System Dummy Mass in Large Configuration(4.1.3) aims at showcasing the different choices performed by the algorithm after the different pre-selection methods are applied independently. The FE model is shown in Figure 5.4.

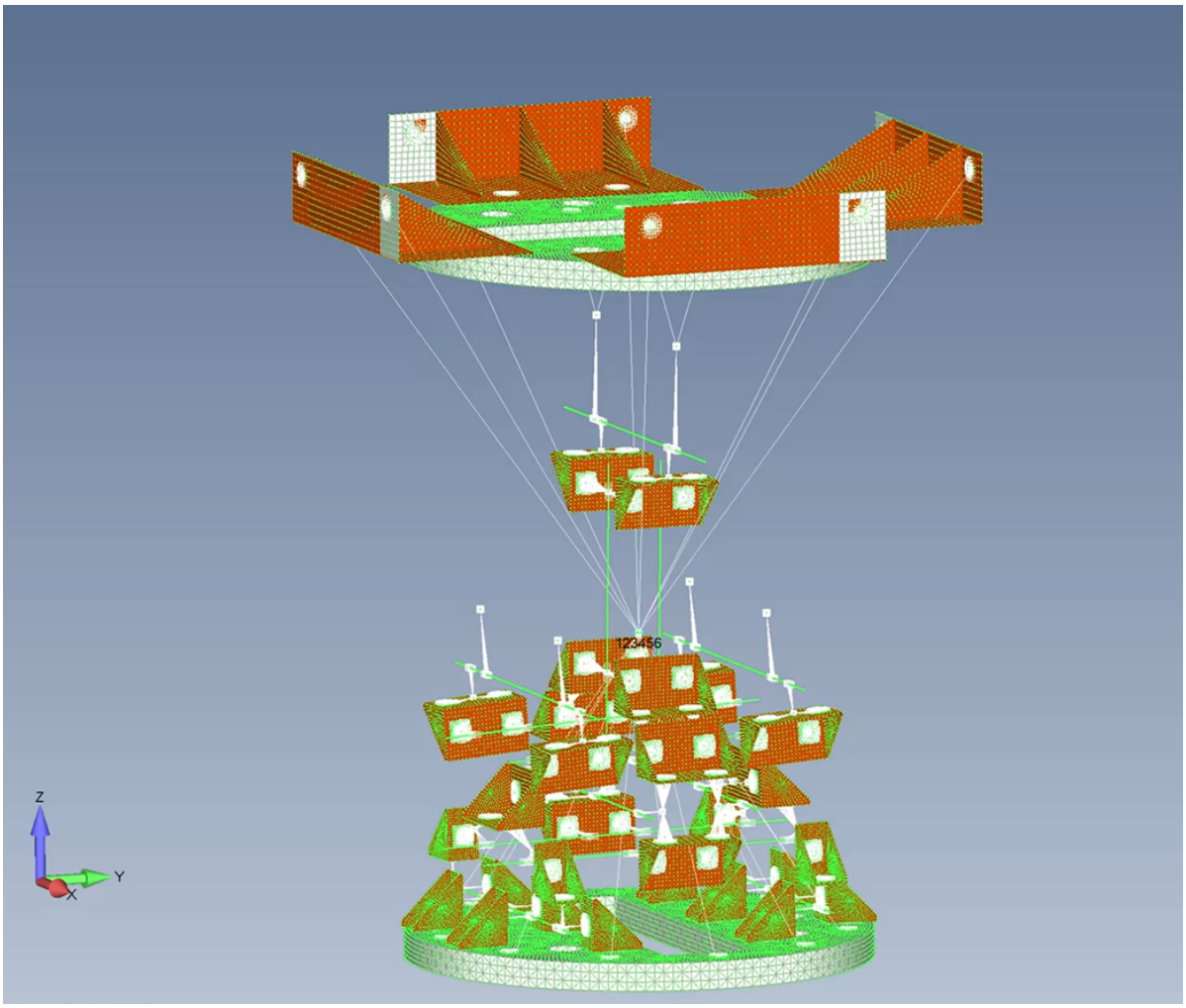

Figure 5.4: Propulsor FEM Model - Large Configuration

Once the detailed FEM model of the Large Configuration PS Dummy Mass was available and a modal analysis performed on it, the algorithm performed sensor selection using the 2 different pre-selection methods targeting a total of 16 accelerometers. The number is an overshooting of the total accelerometers available for testing in order to visualize possible differences and providing the user with the final choice between suggested

points. The high number of sensor places selected is responsible for the redundancy of some selection points being closely spaced, especially in high-excitation areas. In figures 5.5 and 5.6, both the pre-selector chosen candidates and the actual selected points are shown to provide representative example of the strengths and weaknesses of the 2 algorithms tested.

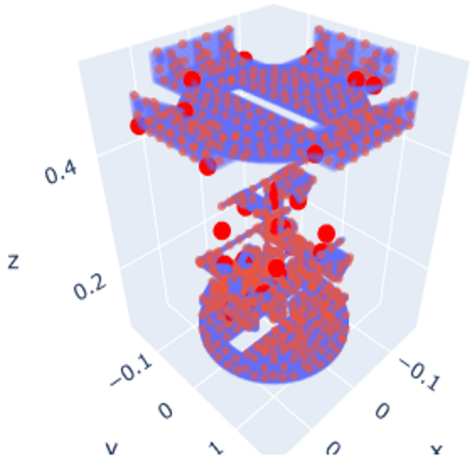

Figure 5.5: Voxel Selection

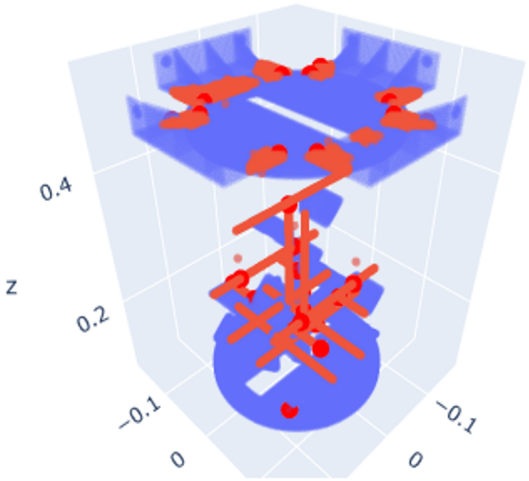

Figure 5.6: MKE Selection

It is particularly evident how the MKE selection tends to focus on the highly energetic areas providing good results from a physical standpoint but potentially missing good locations due to low spatial coverage. The voxel selection on the other hand, fully covers the model, allowing for a greater variety of candidates and reducing the risk of closely spaced sensors. The problem using this algorithm, however, is that not enough selection points are actually placed nearby dynamically active and hence physically important areas, leading to the evaluation of many non-efficient points which will likely be discarded in the EIM selection process. The most important sensor locations are chosen from both the selection algorithms, ensuring general reciprocity and trustworthiness of both methods. The analysis performed to obtain the modal data is a **Constrained Modal Analysis** with constraints applied at the bottom plate of the PS dummy mass and at the top of the L-shaped brackets, both in the dedicated fixtures. As it will eventually be in case of shaker testing as the Large Configuration will be tested fully assembled with the rest of the STM and not as a stand-alone system. Lastly to evaluate the

selected sensors location MAC is calculated using the reduced modal matrix in the selected points of interest. Figures 5.7 and 5.8 show visually the MAC matrix while Table 5.2 shows the most important values obtained from the correlation. In this example Voxelization performs better both at iteration time, due to the $\overline{\overline{\phi}}$ matrix being several order of magnitude smaller, and at final correlation results as expected from the lowest conditioning number (Table 5.1).

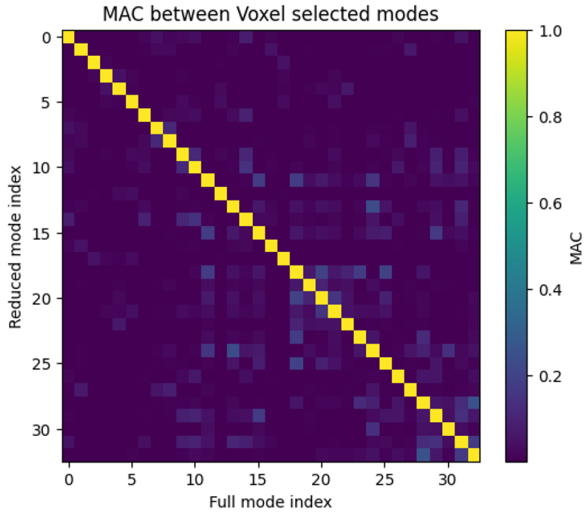

Figure 5.7: Voxel MAC

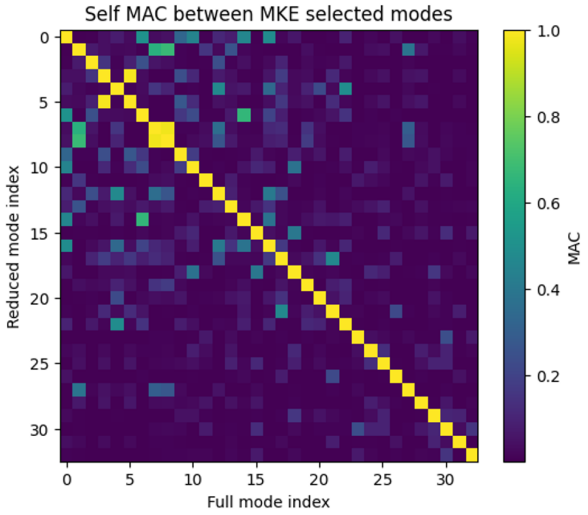

Figure 5.8: MKE MAC

Method	Diagonal Min.	Diagonal Max.	Off-Diagonal Max.	Off-Diagonal Avg.
Voxelization	0.9999994	1.0000011	0.24895607	0.01595325
MKE	0.999992	1.0000007	0.98565954	0.04890084

Table 5.2: MAC values after EIM selection with the 2 different methods

Nonetheless, MKE results proved to be acceptable and at the same level of accuracy of the Voxelization Method, despite a significant larger matrix, and as a consequence, longer computational time. One important characteristic to single-out in these test results is that MKE's $\overline{\overline{\phi}}$ conditioning shows an almost linear decrease as the candidate number increases, allowing for predictability of outcome and possible non-optimal candidates number selection to adjust computational time - accuracy ratio to desiderata. On the other hand the voxel size effect on $\overline{\overline{\phi}}$ is more erratic causing harder predictions and not showing linearity, requiring an optimization to be performed on a case-by-case scenario.
The first active use of the developed methods is applied in selecting sensors

locations for the PS Dummy Mass in Small Configuration (4.1.3). This test was carried out both to verify the quality of the algorithm output and to choose the actual points of interest at which we want to measure the analyzed modes. The finite element model of the item under test is showed in Figure 5.9 as a reference in an undeformed and unmodified state.

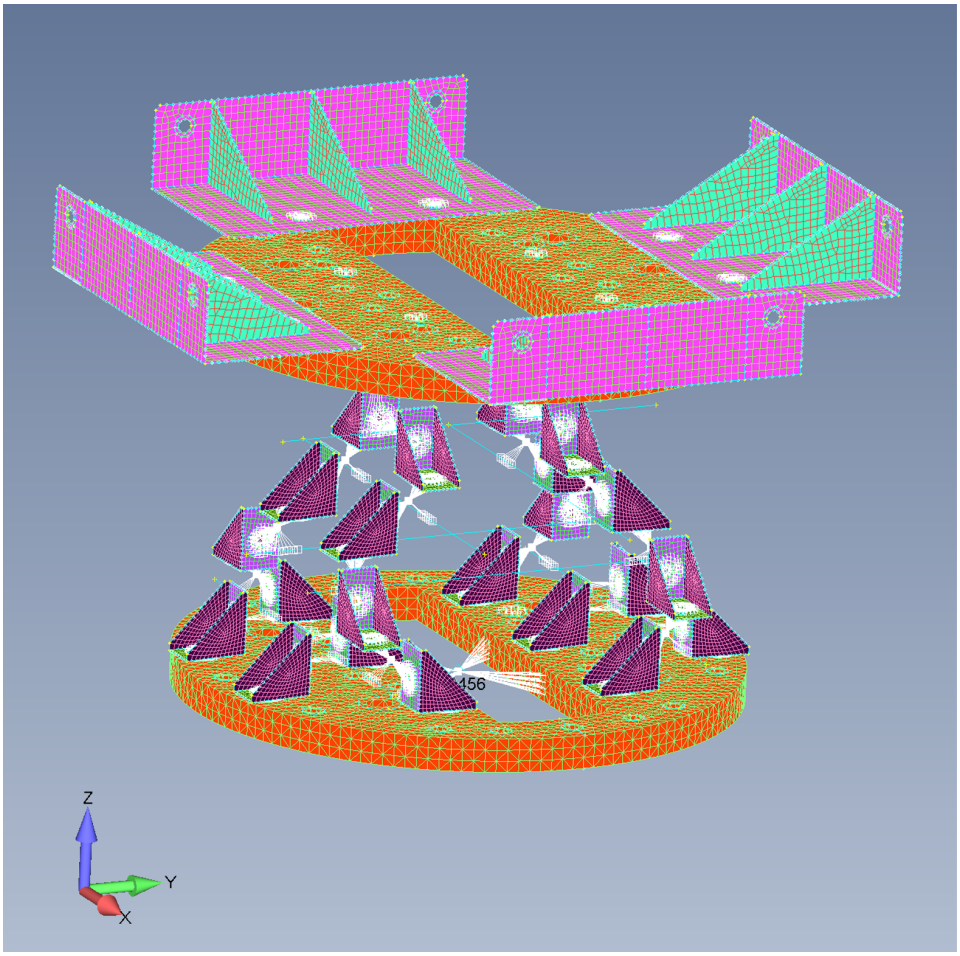

Figure 5.9: Propulsor FEM Model - Small Configuration

Both sensor selection algorithms have been used to evaluate the quality of results, cross-check and choose the best performing. In this example the MKE proved to be the most effective, as well as the fastest, as such, only its results will be showcased for brevity. It is important to notice that both algorithms identified roughly the same points in the analysis. The difference was played by the $\overline{\overline{\phi}}$ conditioning and size, affecting results accuracy and computational time respectively. Figure 5.10 showcases the output of the EIM algorithm and the selected points; it is important to notice that a way smaller number of sensors, roughly equivalent to those than applied to the structure during testing (see Section6.3.1), is

commanded to the algorithm and the modal analysis provided for computation is a Constrained Modal Analysis with constraints only at the Propulsor Base as it will later be during shaker testing.

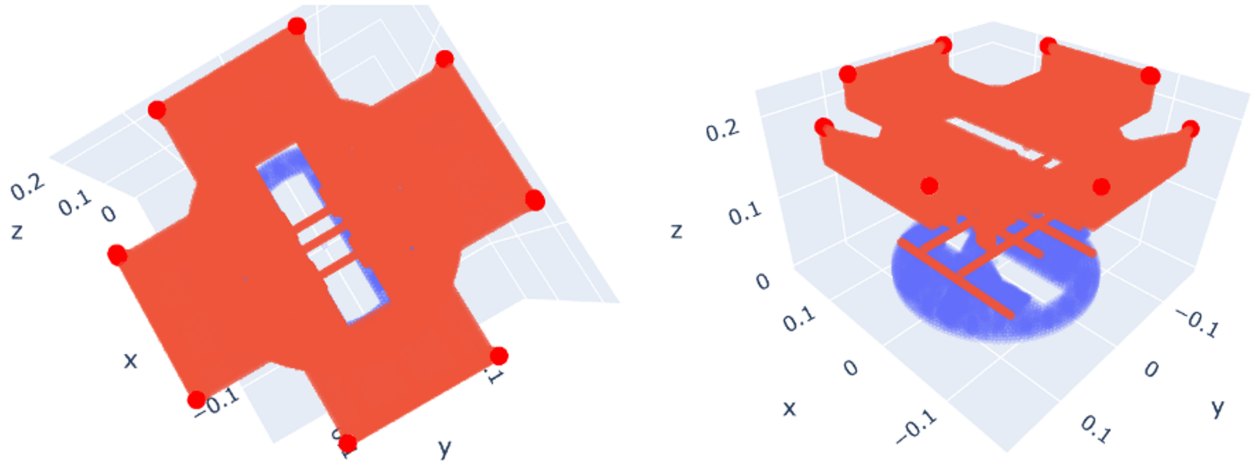

Figure 5.10: Propulsion System Dummy Mass Small Configuration - Final Selection

Once the points are selected MAC is computed to correlate the chosen points and verify their linear independence.
In Figure 5.11, it is clear that a limited number of off-diagonal elements are significant. This is due to some sensor points being selected spatially close to each-other, as 10 sensors were requested to the algorithm but only 8 were singularly unique due to the high concentration of energy in small regions. As already discussed insubsection 5.2.2, this is a characteristic problem with the MKE selection strategy. Nonetheless, it has not proved to be a stopping issue as it just caused redundancy in some already selected points, lowering MAC quality but not affecting final measurements, as will be seen in subsection 6.3.2. Engineering judgment is required for the proper final definition of the sensing points, interpreting the algorithm's solutions.

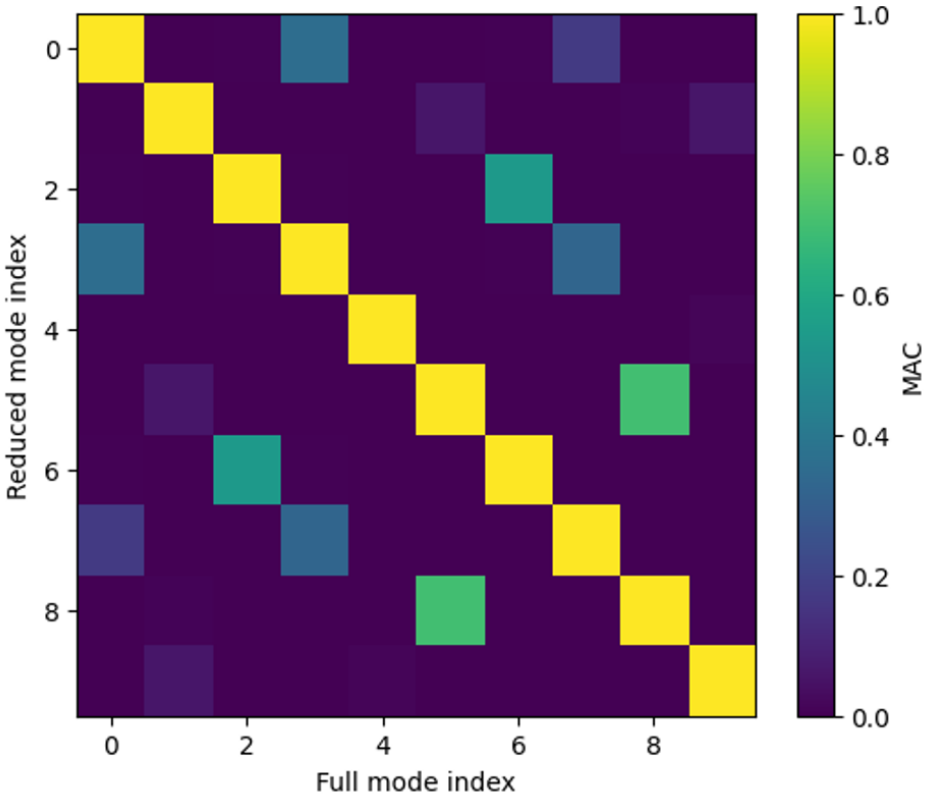

Figure 5.11: Propulsion System Dummy Mass Small Configuration - MAC

5.4.2 Application - HAWK PLUS STM

As the system developed proved successful in testing point selection for a small subsystem, it was deemed ready for its application on HAWK PLUS STM. A specific modal analysis was carried out to compute the Global Kinetic Energy per node as necessary for the MKE Algorithm version. That version of the algorithm was considered primarily due to its key physical background and reliability, despite longer computational times. As both the modal analysis and the BDF file itself proved to be orders of magnitude bigger than the subsystem case, several changes have been implemented in the code to allow for smoother running and shorter computing times. Such changes mainly revolve around considering triaxial accelerometers, as they will practically be, and most importantly, efficiently parsing only the most participated modes of interest. This implementation not only is necessary for faster computational times but it is also crucial for accurate determination of proper testing points. In fact, including all the 100 requested modes in the analysis would cause several local modes on smaller components to be predominant in the Kinetic

Energy computation.

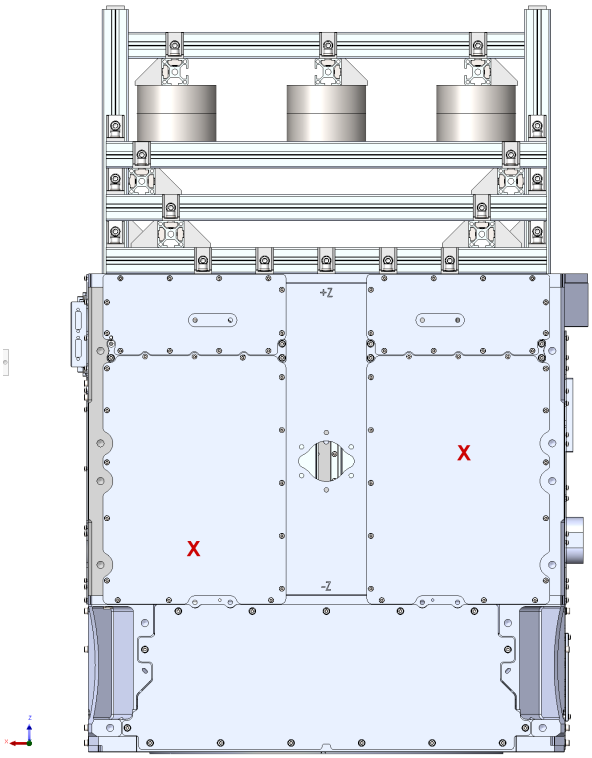

Figure 5.12: Example of tertiary structure selection points due to local modes

An example of this is visible in Figure 5.12, where tertiary structures have been selected due to several local modes creating high displacement areas on the thin panel. One of the several modes affecting the panels is visible in Figure 5.13.
Due to many tertiary components being thin and lightweight, their selection proved recurrent, even if limited by the modal filter, but mostly unimportant for the structural evaluation of the overall satellite's structure. In order to address this recurring phenomenon and improve algorithm efficiency, as well as reducing computational times, an ulterior filter has been introduced based on node IDs. In particular this first layer of filtering effectively excludes all nodes in non-primary structural layers through an active filter on the layer ID and node number. This pre-selection is only possible if the FEM is organized per layer, differentiating the numbering of each section and component.
The final version of the algorithm, with all the modifications previously listed, was than applied to the STM Modal model selecting only the first 9 most participated modes, visible in Table 5.3.
As visible in Figure 5.14, this selection is coherent with the most

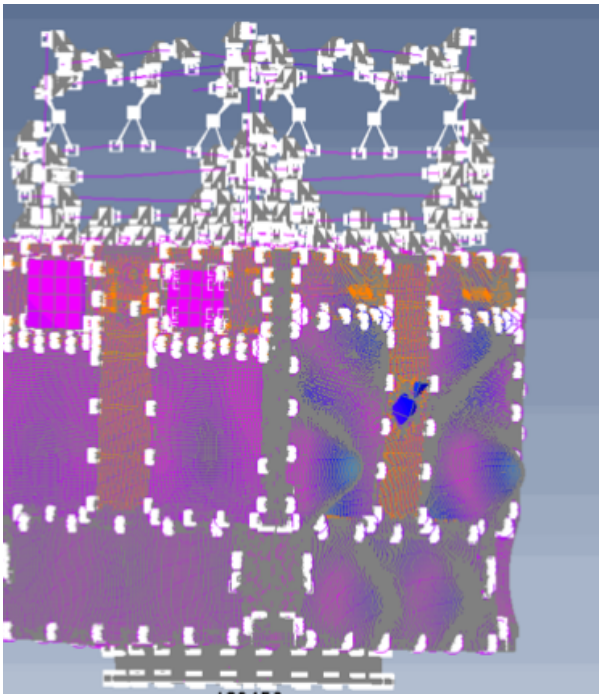

Figure 5.13: Local Mode affecting the tertiary structure panels

Mode	T1	T2	T3
1	0.01%	50.79%	0.00%
2	51.37%	0.02%	0.05%
3	0.16%	0.00%	57.03%
4	0.00%	8.38%	0.05%
5	0.00%	8.83%	0.02%
6	12.95%	0.03%	0.24%
16	0.03%	0.09%	15.49%
32	0.03%	0.00%	11.56%
83	0.01%	8.58%	0.01%

Table 5.3: Modal Partecipation Table

participated modes in the first 100 required modes from NASTRAN's modal analysis on FEMAP. This selection was deemed acceptable as the overall mass participation in each axis reached the 90% threshold and the selected ones represented all those with mass participation over 5%.

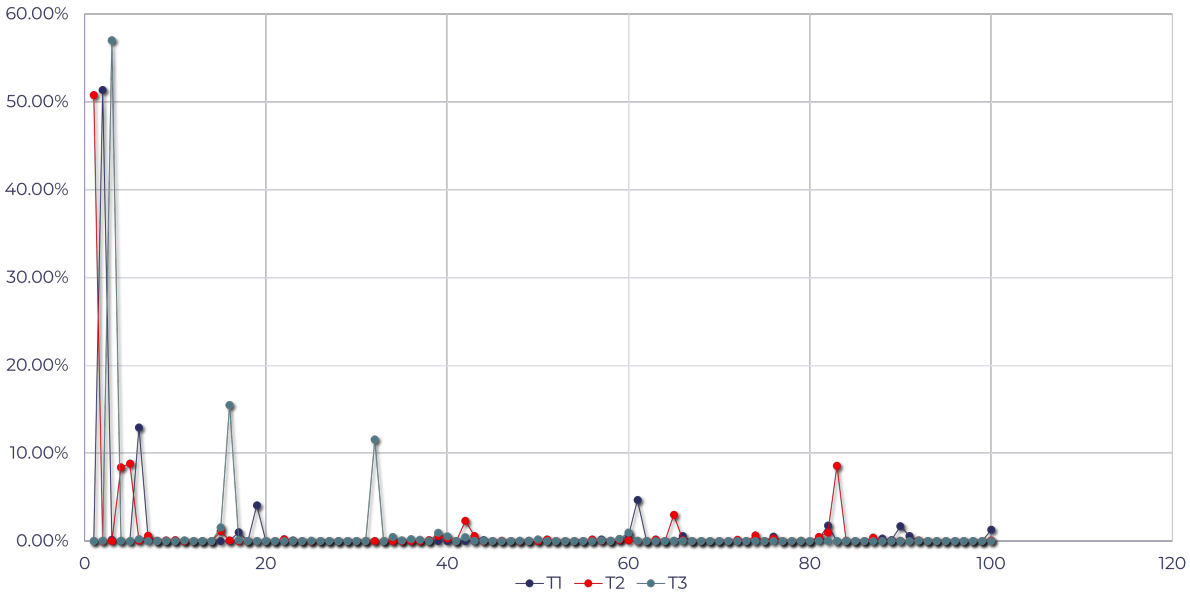

Figure 5.14: Modal Participation distribution in the first 100 modes

The algorithm output locations are listed in Table 5.4. It is clearly visible that multiple closely spaced points have been chosen in higher KE location. This is incompatible with real life testing as , of course, an accelerometer can not physically cover a single node in FEM. Despite this clear issue, which may require future work in introducing a geometry-based filter blocking the algorithm from selecting adjacent points, the output points requested were willingly an higher number than the ones truly needed. This workaround was proven acceptable as the algorithm under test here is not the final scope of the thesis but merely an additional tool designed to enhance the quality and increase the simplicity of obtaining valuable data necessary for the correlation process. Note that in Table 5.4 the Proximity column describes which nodes the chosen node is adjacent to, and as such, an "x" marks a successfully isolated node or the first of a series of closely spaced ones, hence a selection.
The final selections are visible in Figure 5.15, which provides an overview of some selected locations in the Z+ Plate of the STM. These selections were effectively included in the hammer test accelerometers placement as visible in Figure 6.2. Note that the nomenclature in the pictures is purely demonstrative and holds no coherence with the accelerometers naming later defined in chapter 6.

Node ID	Group	Proximity
1016714	PS Deck Central Cylinder	x
1018449	PS Deck Central Cylinder	x
1018751	PS Deck Central Cylinder	1016714
1018792	PS Deck Central Cylinder	x
1021247	PS Deck Central Cylinder	1018449
1021549	PS Deck Central Cylinder	1016714
2006349	PL Deck Central Plate	x
2006350	PL Deck Central Plate	2006349
2006423	PL Deck Central Plate	2006349
3032119	Z+Quarter Plate	x
3032120	Z+Quarter Plate	3032119
3033657	Z+Quarter Plate	x
3033662	Z+Quarter Plate	3033657
3033664	Z+Quarter Plate	3033657
3058440	Z+Quarter Plate	x
5002458	Z+ Quarter Plate AOCS	x
5002569	Z+ Quarter Plate AOCS	x
5009592	Z+ Quarter Plate AOCS	5002458
5016281	Z+ Quarter Plate AOCS	5002458
5016392	Z+ Quarter Plate AOCS	5002569
5020317	Z+ Quarter Plate AOCS	5002569
5024034	Z+ Quarter Plate AOCS	5002569
5024145	Z+ Quarter Plate AOCS	5002458
5027599	Z+ Quarter Plate AOCS	5002458
5027710	Z+ Quarter Plate AOCS	5002458
6004827	EPS Bay Back Plane	x
6009113	EPS Bay Back Plane	x
6009680	EPS Bay Back Plane	6004827
6013949	EPS Bay Back Plane	6009113
6013966	EPS Bay Back Plane	6009113

Table 5.4: Node Selected by the Algorithm

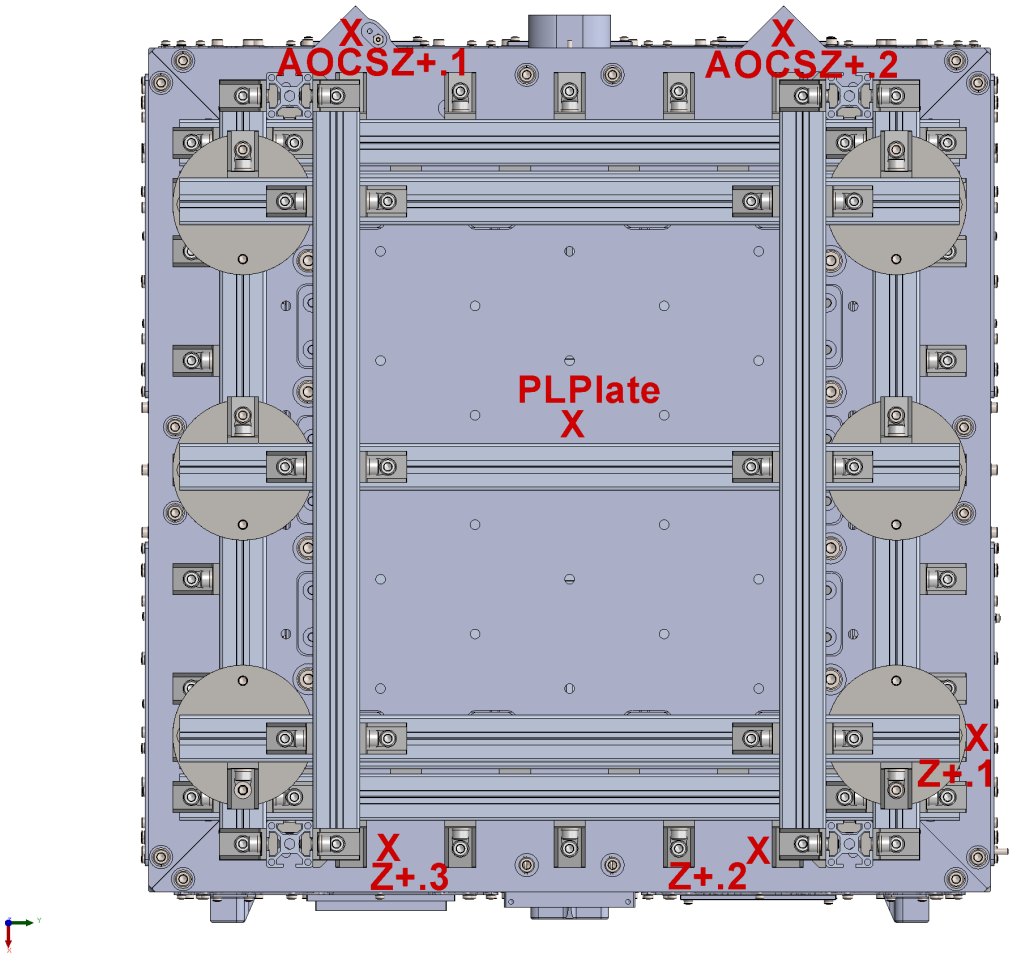

Figure 5.15: Sensor Location on Payload Interface (Z+)

Tests Performed

6.1 Objectives

This section aims to provide a description of the tests performed to gather the modal data necessary for the updating procedure.

- **Hammer Test:** The main goal of the hammer test is to provide FRFs [g/N] between the different sensing points and the input location where the excitation force is applied. This test is performed both in the Free-Free configuration and in the Constrained set-up. This allows for the characterization of the normal modes of the STM without the boundary effects caused by the ring connector. A proper free-free boundary definition is needed to achieve the minimization of the springs and strings influence on the final results. Lastly, the hammer test is performed to gather information on the mass participation of the normal modes due to the input being a Force and hence preserving the mass information in the FRF, contrary to the shaker test.
- **Shaker Vibrations Test:** The shaker vibrations test is performed to test the STM under several important load cases such as quasi-static, random and sine sweeps. Resonance researches are carried out in between said tests to assess if the structure was damaged during the procedure. This is standard practice as structural damage would cause frequency shifts detectable during different resonance searches. For the scope of this thesis, the Shaker vibration tests are particularly important as they provide a cleaner and more precise information on the frequency at which the resonance peak is registered. This is mostly due to the type and force of the excitation the shaker provides on a large body such as a satellite.

6.2 Hammer Test

6.2.1 Test Set-up

The hammer test was carried out in Argotec's cleanroom using a modal hammer, a spider with 32 ports hosting cables for 10 tri-axial accelerometers,1 mono-axial accelerometer and 1 input channel. Several rovings were carried out in different configurations to allow for optimal data gathering and to cover extra positions in order to gather additional data for the post-processing phase. These extra-accelerometers are placed in proximity of important components, such as the reaction wheels or the bays back plates to monitor internal subsystems and better characterize the core behavior. A short recap of the sensor positions is visible in Table 6.1.
As previously stated several rovings were necessary to fully cover the different configurations including a distinction between Free-Free and constrained Load cases. An overall map of the different rovings including the accelerometers present at each iteration is visible in Figure 6.1. As not all roving cases proved successful in providing useful data for the correlation process only the most effective ones will be covered in subsection 6.2.2. The positions of the accelerometers are visible in Figure 6.2 and it can be seen how the Sensor Location algorithm was effectively used as a reference for the selection of several of the final sensor locations(Figure 5.15). Also a visual photograph of sensors placed in the described locations during Test Case 1 of the hammer test roving cases is provided in Figure 6.3. A picture of the Free-Free mounting is given in Figure 6.4a for reference and in Figure 6.4b the constrained setup is shown. Several input points were selected to excite the spacecraft response in different locations and along the 3 axis. In particular, excitation points were selected on the ring interface (In Free-Free configuration), on the ring itself (In constraint configuration) , along the Bay Base Plate closer to the CoG of the spacecraft and on the upper plate on the payload interface.

Sensor	Position	Normal Direction	Sensor	Position	Normal Direction
MP1	Z- Thruster Plate near ring connection	Z-	MP12	AOCS Z+ Plate on Right(Y+) Star Tracker	Z+
MP2	Upper Part of the core	Z-	MP13	Z+ Plate near Payload interface in Y+	Z+
MP3	Z+ Plate near Payload interface in Y-	Z+	MP14	Z+ Plate near Payload interface in X+	Z+
MP4	Central PL plate	Z+(mono)	MP15	AOCS 45deg side panel external (X-)	X-
MP5	AOCS Z+ Plate on Left(Y-) Star Tracker	Z+	MP16	Y- EPS Bay Right(X+) External Panel	Y-
MP6	AOCS (X-) Back Plate	X-	MP17	Y- EPS Bay External Bay Support	Y-
MP7	EPS (Y-) Back Plate	Y-	MP18	X- AOCS Bay Right(Y-) External Panel	Y-
MP8	EPS (Y+) Back Plate	Y+	MP19	Z- Thruster Plate more central	Z-
MP9	Avionics(X+) Back Plate Higher	X+	MP20	On the RBF ring nearby Interface connection	Z-
MP10	Avionics(X+) Back Plate Lower	X+	MP21	Z- Plate Corner between X- and Y-	Z-
MP11	External(X-) Nearby RW	X-			

Table 6.1: Sensor Positions and main accelerometer direction for Hammer Test

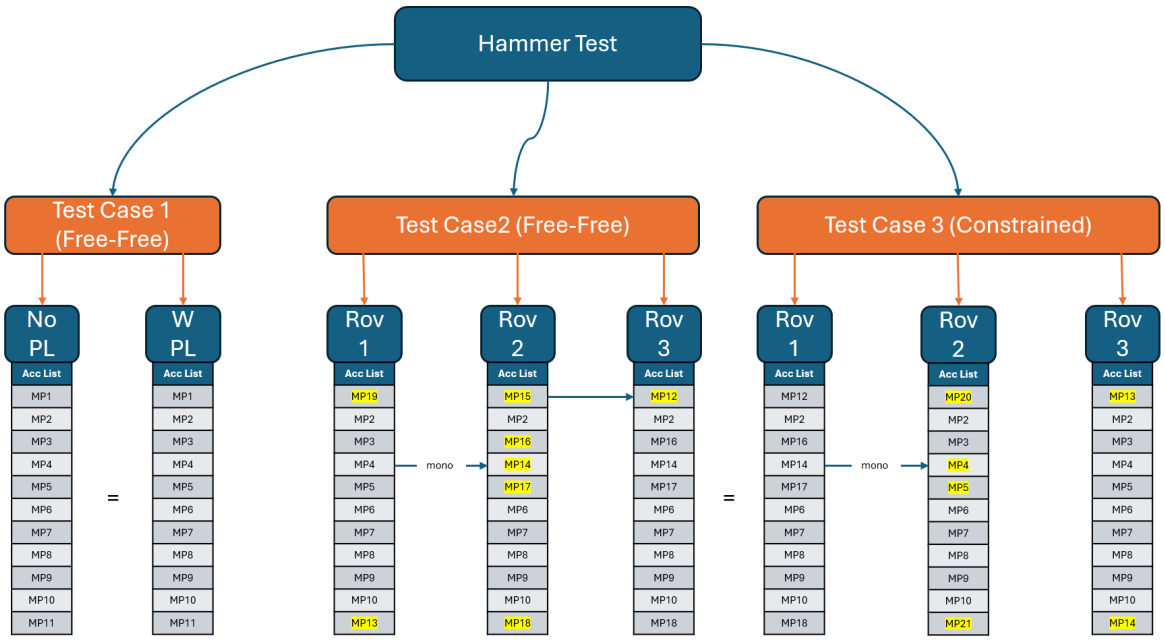

Figure 6.1: Sensor Roving during Hammer Testing

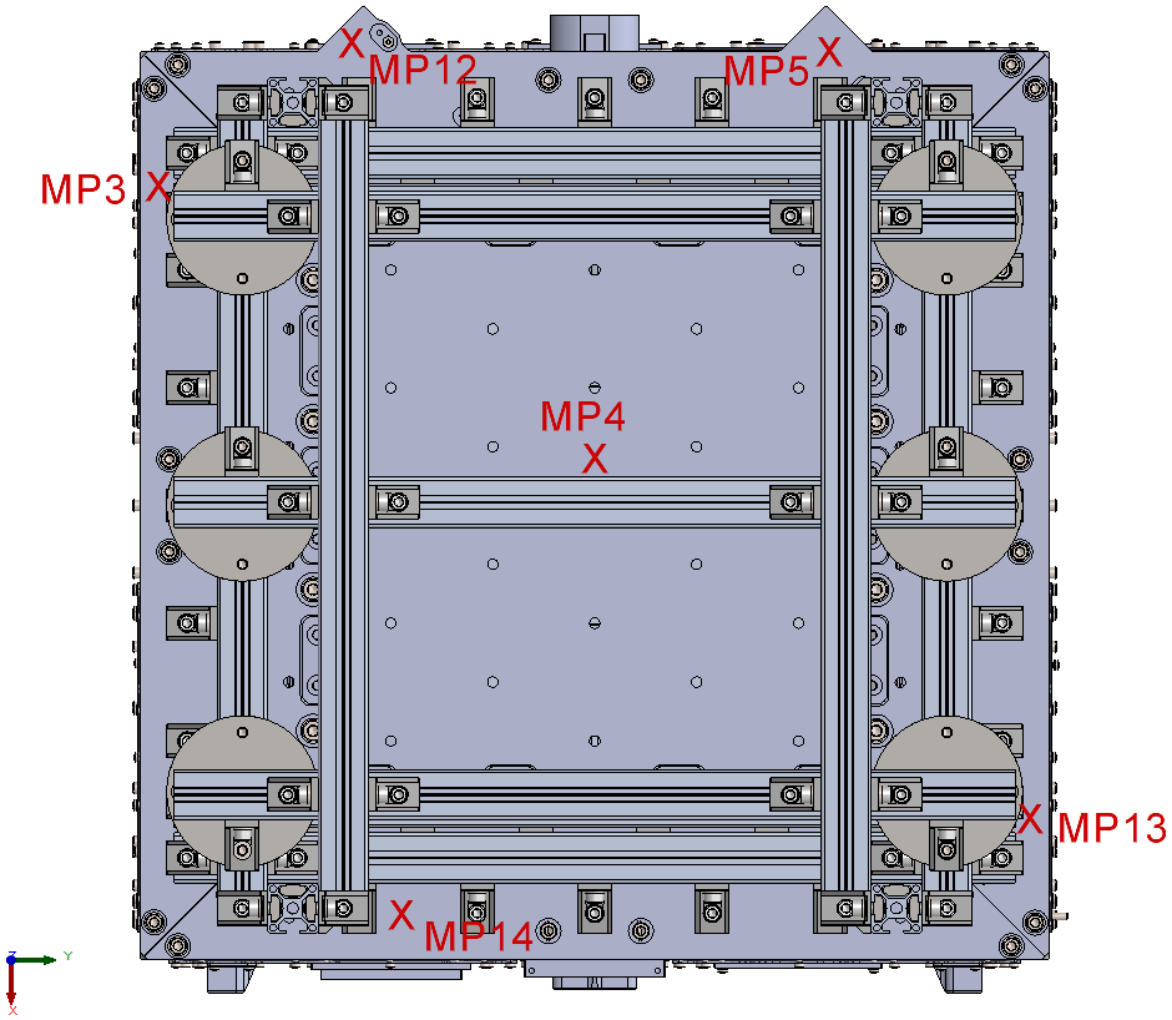

Figure 6.2: Sensor Locations in the Z+ Plate

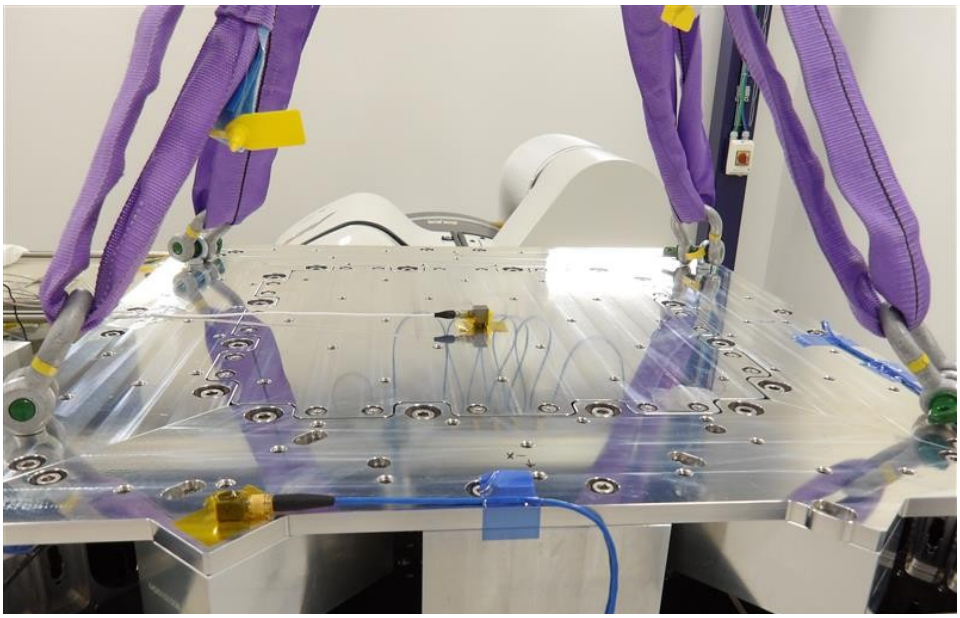

Figure 6.3: Sensor Positioning in the Z+ Plate

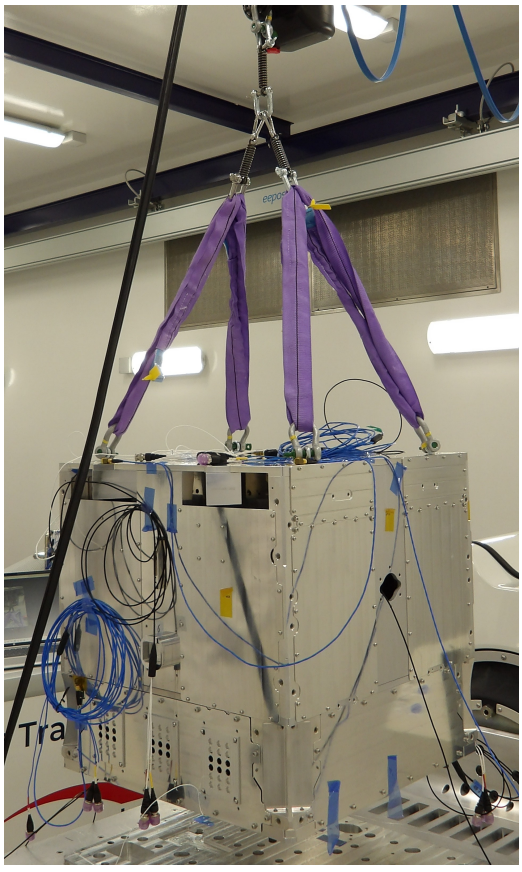

(a) Free-Free Configuration without Payload

(b) Constrained Configuration with Payload

Figure 6.4: Photographs taken during Hammer Test

6.2.2 Test Data

Test data is gathered in several roving cases as specified in subsection 6.2.1 in order to fully characterize the structure and its modal behavior. The FRFs gathered from the hammer test provide information about the modal characteristics of the structure, in particular its resonant frequencies, while retaining the mass information. As such, the different input locations allow for the characterization of the response throughout the structure, starting from the connection ring, in order to assess how the vibrations propagate inside the spacecraft. An example FRF is shown in Figure 6.5 as the ratio between the response measured by accelerometer MP6 in the X direction and the input force registered by the modal hammer load cell when hitting in the same direction. The software used

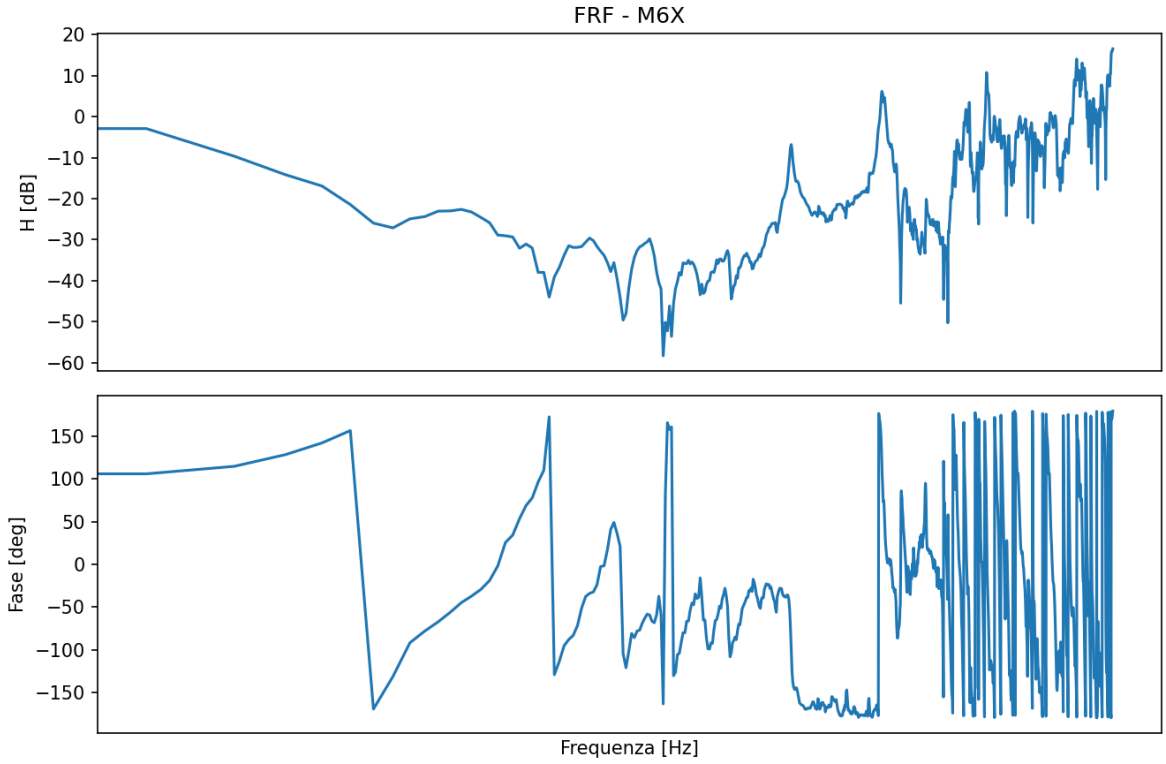

Figure 6.5: FRF Between MP6 and input

for the modal hammer test also allows for modal parameters identification and modes synthesis which are both useful and needed tools for the correlation, in particular modes tracking.

6.3 Shaker Test

6.3.1 Propulsion System Dummy Mass Test Set-up

Coherently with the positions identified by the software in Figure 5.9 the accelerometers during the test are placed as shown in Figure 6.6. Two additional sensors have been mounted for monitoring the COG(B2) and as a copilot(B1) to monitor the input spectrum given by the shaker.

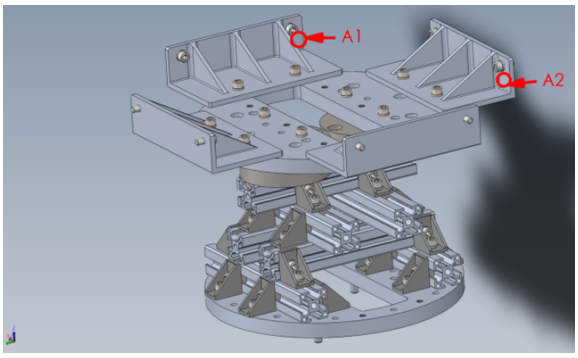

(a) A1 and A2 Sensor Positions

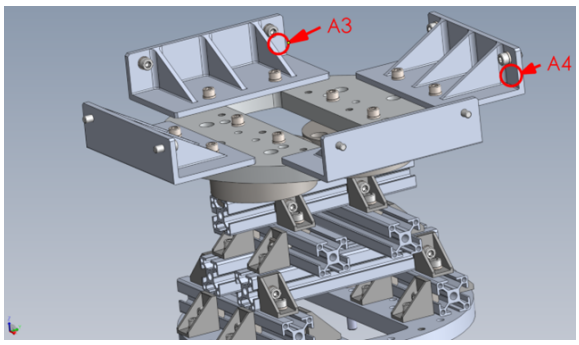

(b) A3 and A4 Sensor Positions

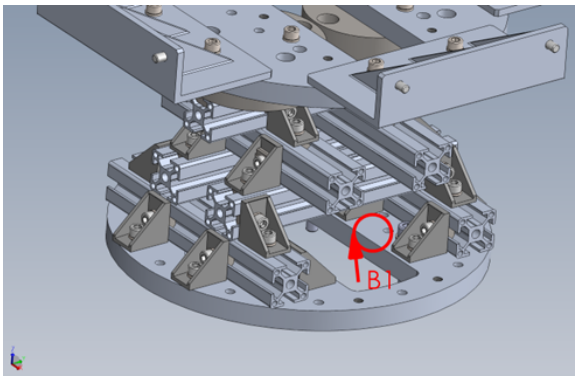

(c) B1 Sensor Position

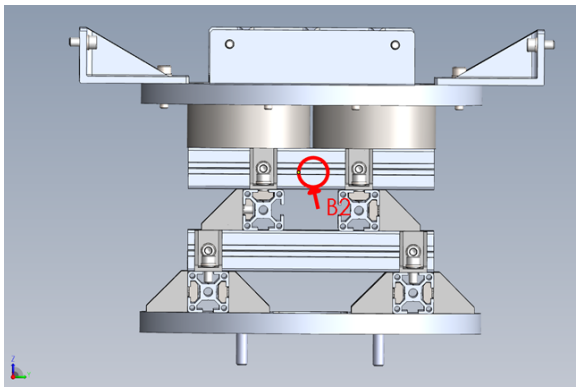

(d) B2 Sensor Position

Figure 6.6: Sensor Placement during Vibration Testing

The IUT is tested only in the Z direction as the scope of the test is only to provide data necessary for further developing the updating algorithm and code in the early stages. In order to perform the test the IUT is connected to the expander table of the Shaker and is than excited at 1g performing the resonance search. Similarly with all other test set-ups performed the accelerometers are fixed applying a layer of kapton both on the sensor and the area of interest on the IUT and than gluing together both layers to keep the accelerometer in position. Additional pathing is provided to the sensor cable to the spider, partially constraining it with kapton in order to limit its vibration during the test procedure. Particular attention is given

to the accelerometer orientation to align it with the IUT main reference system.

6.3.2 Propulsion System Dummy Mass Test Data

As mentioned in subsection 6.3.1 the only excitation direction in this test is the Z axis and as such only the data in that direction is available. The FRFs are than computed singularly for each sensor and are visible in Figure 6.8. In particular it is worth noting that B1Z (Figure 6.8a) is attached to the bottom plate which is constrained and as such its measure is only used for control purposes only. On the contrary it is clear that the positions identified by the algorithm are effective for measuring all the modes of interest in this direction proving it successful. Further analysis on the data will be performed in chapter 7 during the correlation process. Lastly an overall superposition of the different sensor measurements, useful for peak identification and cross-checking, is available in Figure 6.7.

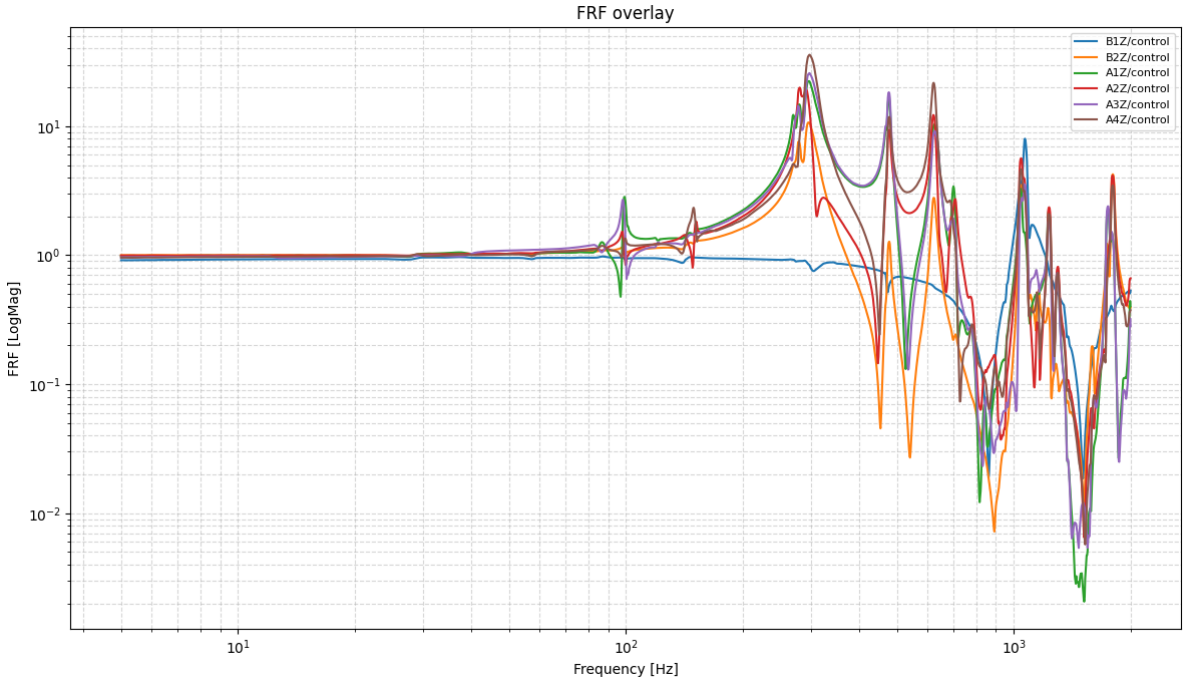

Figure 6.7: Superposition of all FRFs captured during the test

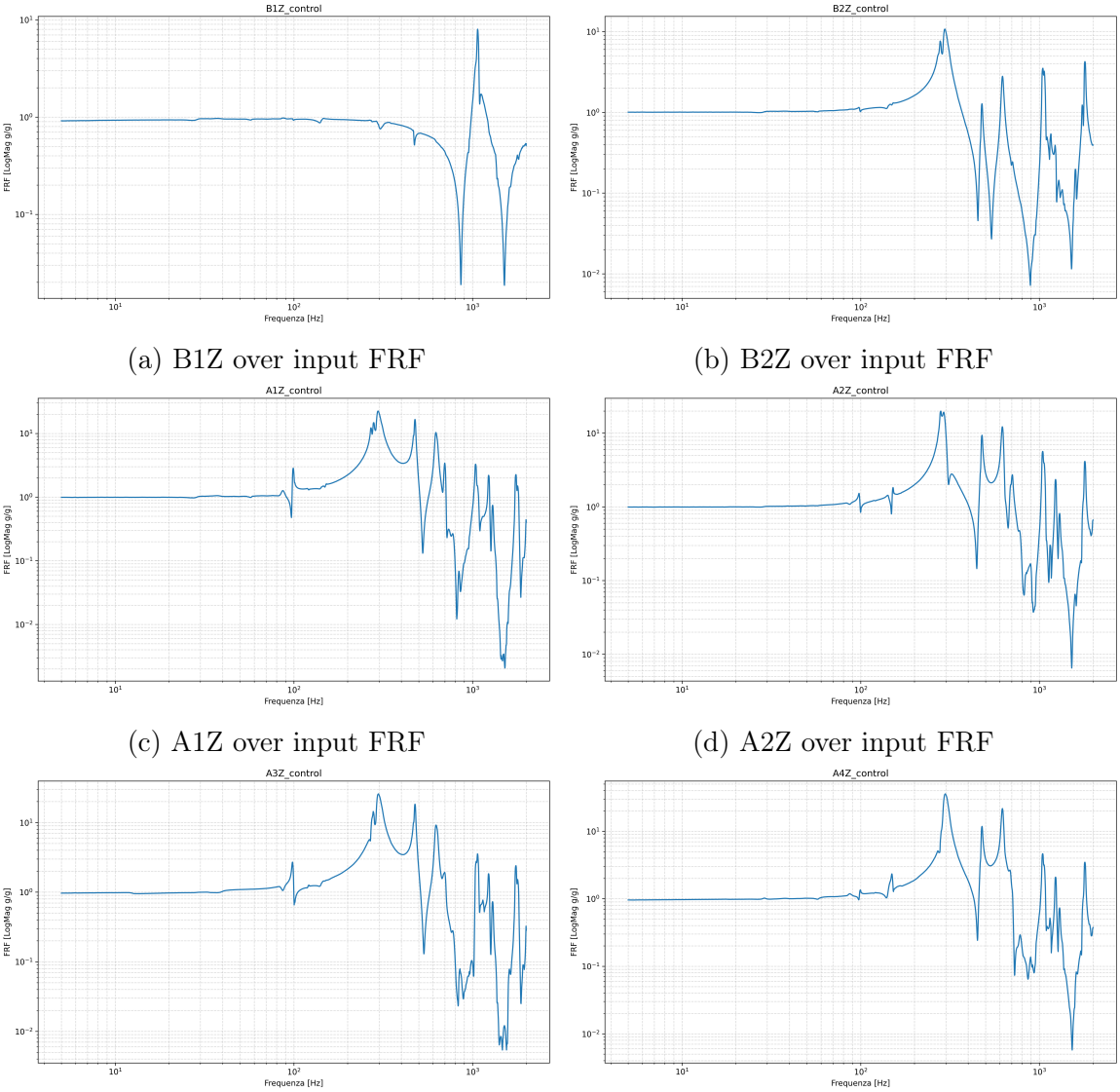

(a) B1Z over input FRF

(b) B2Z over input FRF

(c) A1Z over input FRF

(d) A2Z over input FRF

(e) A3Z over input FRF

(f) A4Z over input FRF

Figure 6.8: Accelerometers FRFs

6.3.3 HAWK PLUS Test Set-up

Most of the accelerometer positions in the shaker test configuration are coherent with those of the hammer test although some sensors have been moved to monitor different behaviors of the structure during random and quasi-static testing. Due to the changes being limited and mostly irrelevant for the purpose of modal data acquisition the new positions won't be repeated in this section, refer to subsection 6.2.1 for sensor locations. Moreover due to the availability of 2 spiders all the sensing points will be acquired simultaneously allowing for up to 64 output channels to be recorded. This adjustments erases the need of multiple roving over the interest locations and hence cancels the possible differences between inputs which instead affect the hammer test. It is also important to notice that a different, more realistic, dummy mass of the connection ring has been used in the shaker testing process. This difference slightly changes the boundary conditions of the test and hence causes a difference, although small, in the final resulting normal frequencies detected during the test. A photo of the final setup before testing on the slip table x and y axis is shown in Figure 6.9 for reference.

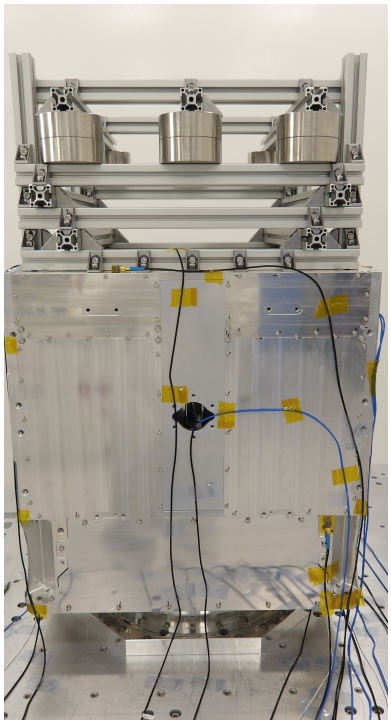

Figure 6.9: STM setup on the Shaker Slip Table

6.3.4 HAWK PLUS Test Data

The outputs from the shaker vibration testing are FRFs obtained by confronting accelerations both in input, recorded by the shaker itself, and in output, measured by the accelerometers. These curves are useful for an easier detection of the resonant frequencies as the higher input allows for clearer peaks with regard to the hammer test. An example FRF obtained by teh shaker test in the Z Axis of the STM is visible in Figure 6.10 for reference. The values obtained by these tests are used in correlating the model due to the higher reliability of frequency measurement and quantity of data available

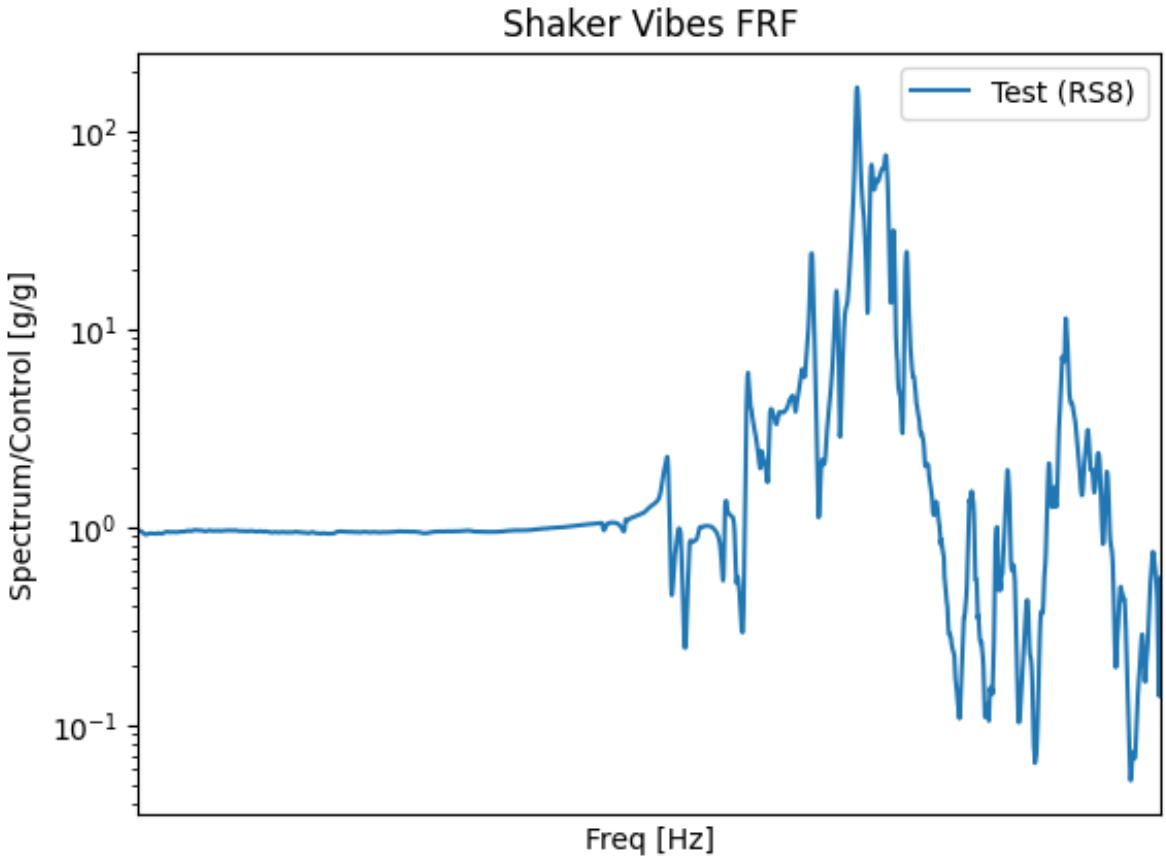

Figure 6.10: Output Example from the Vibes Test

Updating Process

7.1 Overview

In order to successfully correlate any model, it is crucial to properly define the plan and procedure that will be applied at each iteration of the process. The general method showcased in section 1.3 is hereby detailed and explained to provide an accurate methodology definition that is completely independent of the IUT and, hence, completely repeatable. Figure 7.1 provides a detailed explanation of the entire process, giving a useful reference map for the process and its crucial components. The starting points of the procedure are, as expected, the analytical model and the test data provided by the different testing methods described in section 2.2 and chapter 6. In section 7.2, the suggested initial adjustments for the smoothest integration with the developed tools, are detailed. Once the necessary data is gathered or provided, the initial test-FEM correlation (section 7.4) is performed to assess the quality of the data, the results expected by the method, and the desired targets to meet. Once the initial differences between model and test are assessed, an error localisation procedure is applied to assess the best candidates for the final optimization, as described in section 7.5. Lastly, the chosen variables are iterated in an optimization process limited by physical or generally imposed admissible boundaries.
The entire procedure is implemented via a customized Python code, handling the entire updating process from initial model import, through all the steps detailed in Figure 7.1, up until the final correlated model export.

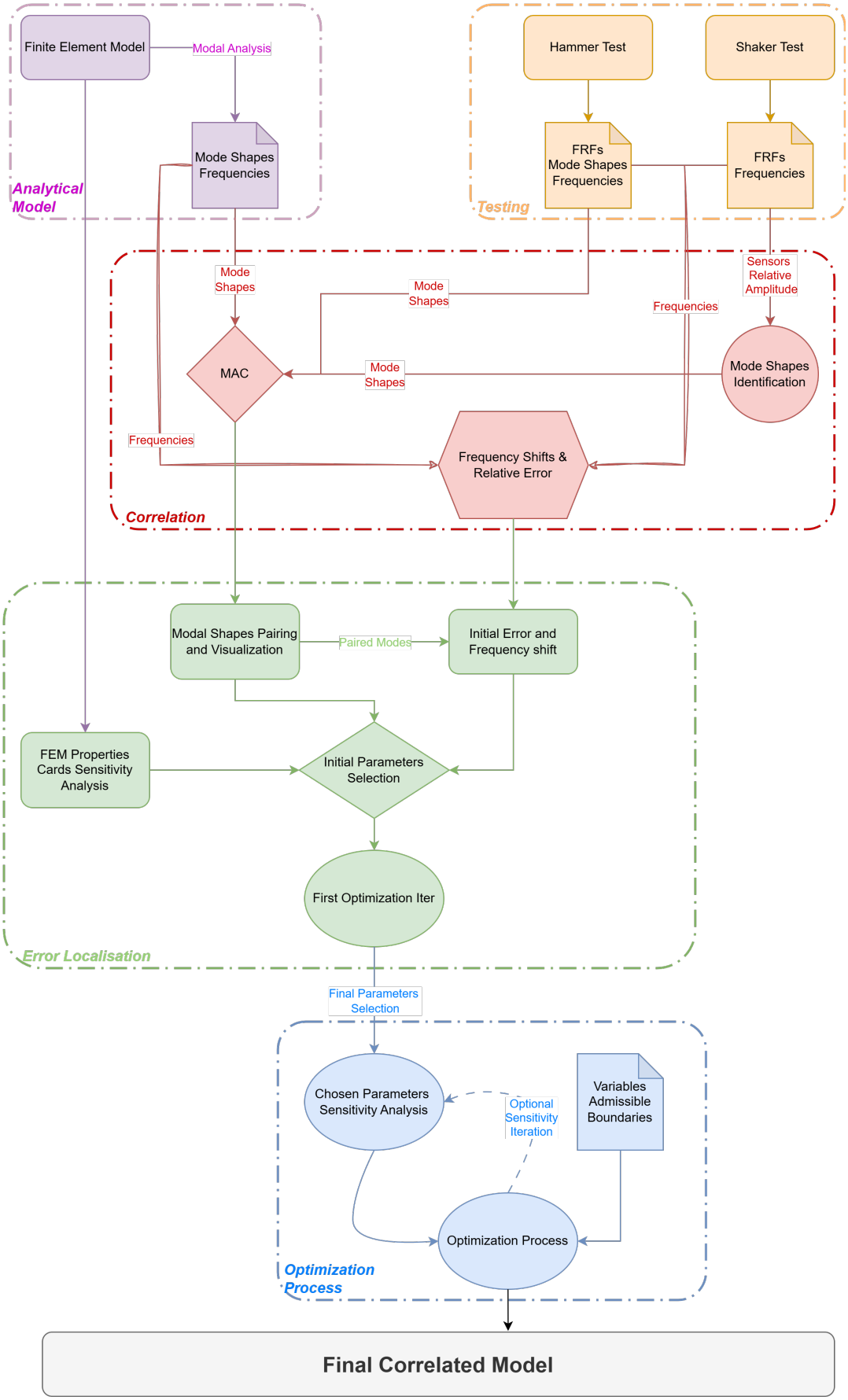

Figure 7.1: Detailed Correlation Plan

7.2 Analytical Model

Although no actual requirement is imposed on the initial Finite Element Model there are several considerations which would overall improve the efficient integration of any model with the actual code of the updating procedure.
Firstly, it is important to state that the written algorithm actively uses NASTRAN for model definition, modal analysis execution and output results reading. This allows the written code to operate on the .dat file given in input to NASTRAN, modifying the properties cards described in the bulk section of the file.
The necessary outputs to be requested to the NASTRAN solver are the natural frequencies in the range of interest, their mode shapes and the mass participation of each mode. All said outputs are extracted and post processed directly from the standard F06 and OP2 files generated by NASTRAN.
With proper definition and implementations, the output might be reduced to the OP2 file only, but no effective benefits, for neither solving capabilities or computational times, have been found to justify the additional coding effort necessary to implement such changes in the cases under analysis in this thesis.
Although no other output is necessary, a selection of general good practices adopted during the methodology development is provided:

- The software actively works on defined properties only, both materials and element cards. It is recommended to add personalized properties in the areas of interest and split properties affecting a large number of elements, as may be the case for the materials, in several different copies of the same card to allow the solver to independently modify each one.

- On the other hand, it must be considered that adding parameters as variables increases computational time, especially of the sensitivity analysis, Hence, in case of large and complex structures a pre-selection of primary structures or known uncertainty areas is suggested to minimize iterations.

- Although the tested algorithm proved efficient in terms of computational time, the most time consuming activity is the iteration

of modal analysis to build the sensitivity matrix, as detailed later in section 7.6. Hence investing time initially in properly defining the modal analysis case is strongly suggested. For example, properly defining the frequency range of interest or the number of modes desired may shorten the single analysis time consumption, consequently providing considerable time reductions in the complete run.

- In case an additional error localisation, or optimal sensor location determination, is requested it is possible to directly compute the Kinetic Energy per grid node or the Strain Energy per node. The following NASTRAN code lines have to be added to the DAT file in the analysis definition:[HEX22]
  "ESE(PLOT) = ALL"
  "EKE(PLOT) = ALL"
  These outputs are included in the OP2 file which, being a binary format, is very efficient in saving great amount of data, but once again, caution must be advised. In fact these requirements apply to each node of the structural node, which, for large models, may likely be in the order of millions. As such, the output file is usually really complex to manage and computationally intensive to extract and elaborate. Hence, it is suggested to exclude these lines from the iterative modal analysis performed during the sensitivity matrix, and only require said outputs in a separate DAT file.

- In case of availability of hammer test data, the Cross Orthogonality Check may also be computed as defined in subsection 2.3.3. An additional input has to be added in the analysis case definition in the DAT file, namely:
  "PARAM,EXTOUT,DMIGPCH" [HEX22]
  The additional code line creates an output PCH file containing the complete mass matrix of the structure under analysis, used by the solver in the process. It is crucial to caution that this file requires plenty of available space and computational time to be created and as such it is heavily advised against to include this code in the run used to create the sensitivity matrix and the optimization process in general. An alternative solution may be to only create a super-element with appropriate reduction methods, such as the

Craig-Bampton method, with the known positions of the testing points and compute its mass matrix only as it is order of magnitude smaller and easier to obtain [HEX23].

Lastly, when modelling, it is important to keep in mind which type of element is used, and consequently, which cards each element creates and are hence available for optimization.

7.3 Test Data

Depending on the performed tests and data available the following steps apply:

- **Shaker Test:** As a resonance search is carried out through a Sine Sweep the accelerometers data as well as the input provided are recorded. The Transfer Function between input and output is than computed by the testing software or via a custom python code. The different Transfer Functions are compared and the resonant frequencies are than provided by the testing software [Insc] or may alternatively be extracted using a custom python code based on a Peak Picking technique.
- **Hammer Test:** Since the input force is measured during hammer testing, the structure's FRFs can be computed directly. FRF generation is handled either by the test software, with the help of a Mode Indicator Function (MIF), or by custom Python code, provided that both the sensor outputs and the force input are recorded. The test software then uses modal parameter identification tools, including the stability diagram implemented Least Square Complex Exponential (LSCE) fitter for pole identification. The stable physical poles (as opposed to 'computational poles' sometimes produced by the LSCE) are than selected from the Stability Diagram for the next step mode shape calculation, using the Least Square Frequency Domain (LSFD) algorithm [Insb]. After the modes are selected, the corresponding natural frequencies, damping values, and mode shapes can be calculated and displayed or animated. [Insa]

7.4 Correlation

As the analytical data and the corresponding test results are gathered, the initial correlation shall be performed mainly on the modal shapes and the frequencies of the selected modes. The two main tools chosen for proper correlation between models are the MAC function (detailed in subsection 2.3.2) and the relative error equation to describe the difference between test and analytical frequencies of the normal modes.

7.4.1 Frequency Error

The first parameter to evaluate proper correlation is the cost function described in Equation 7.1, as it gives a weighted relative error between the analytical results (represented by λ_a in the equation) and the test results (represented by λ_m in the equation).

$$E(X) = w_g \sum_{j=1}^{P} w_j (\frac{\lambda_{aj} - \lambda_{mj}}{\lambda_{mj}})^2 \tag{7.1}$$

Notably, both a global weighting matrix w_g and a local weighting vector w_j, are present to allow proper prioritization in the following updating process of chosen modes. The presented equation is the objective function of the minimization algorithm, which is adopted in the optimization section for the following reasons:

- It is a simple vector algorithm, ensuring efficiency, fast computational times and better data handling;
- Thr frequency-based cost function, allows the process to function using data which can be automatically extracted from the F06 and OP2 files, generated at each iteration of the optimization process.

The main problem with this approach is related to mode pairing as the modes must be correctly paired to properly compute the error. This pairing must be ensured both between initial test-analysis data correlation and throughout the entire optimization process to achieve consistent optimization and avoid mode switching. Metrics and methods to approach the known problem are presented in the following subsection 7.4.2 and subsection 7.4.3.

7.4.2 MAC & MMI

As mentioned in subsection 7.4.1 it is crucial for the optimization process to ensure proper mode pairing throughout the entire process, two metrics are hereby presented to achieve such result.
The first metric chosen is the MAC, as formulated in Equation 2.22, as it is independent from the modes normalization and is a reliable method to identify matching modes starting from their mode shapes. An additional metric has been added at each step to increase the matching reliability and increase overall likelihood of the modes actually matching. Said matrix the Modes Matching Index [Sve+21] and takes into account both the frequency shift and the MAC values of two candidate modes weighted by a factor γ,as follows:

$$MMI = (1-\gamma)MAC_{m,n} - \gamma\frac{|f_m - f_n|}{f_m} \tag{7.2}$$

These tools are used both in the first correlation and during the iterative optimization process to ensure mode tracking. At each iteration the MAC and MMI values are computed for each output mode from the solver with respect to those resulting from the tests. The best fit is labeled as chosen mode for pairing and is used for the error function computation.
The redundancy of metrics to track the modes enables a greater degree of confidence in the proper pairing, but it is heavily dependent on the accurate acquisition of test mode shapes.

7.4.3 Mode Shapes Identification

As previously stated in section 6.3, the results derived from the shaker vibration testing lack the crucial information of mode shapes. To address this problem and integrate the shaker testing in the correlation procedure a manual approach is proposed to gather the necessary information regarding the modes shape. In particular, the amplitude measured during the test by each sensor is observed to verify that the areas with the highest deformation measured by the FEM model are effectively closely spaced with the sensors measuring the highest amplitude. This manual approach provides a first layer of visual cross-checking between FEM modes and accelerometers data. Once the first assessment is carried out, a Frequency/Harmonic Response analysis is performed using NASTRAN,

while giving a sine load input coherent with the one provided by the shaker to visualize the amplitude in response in each accelerometer location.
In case of reliable test data and well spaced modes the test and analysis results are then visually confronted, as shown in Figure 7.2. Each accelerometer location is investigated to assess which modes visible in the FEM model have an actual correspondence with those derived from the tests. Once a proper matching is found, the corresponding frequency measured by the shaker test is assigned to the initial FEM mode shape in order to allow mode tracking during the optimization process. As each mode shape is assigned by the initial FEM model for mode tracking purposes, this solution isn't suitable for optimization based on a mode shape objective function but can be used with the frequency based objective function described in subsection 7.4.1. This is, of course, only feasible with a limited number of modes chosen to be correlated, and it becomes increasingly unreliable the more complex the mode is, as it would be seemingly impossible to reliably identify said complex modes with a limited number of sensor outputs.

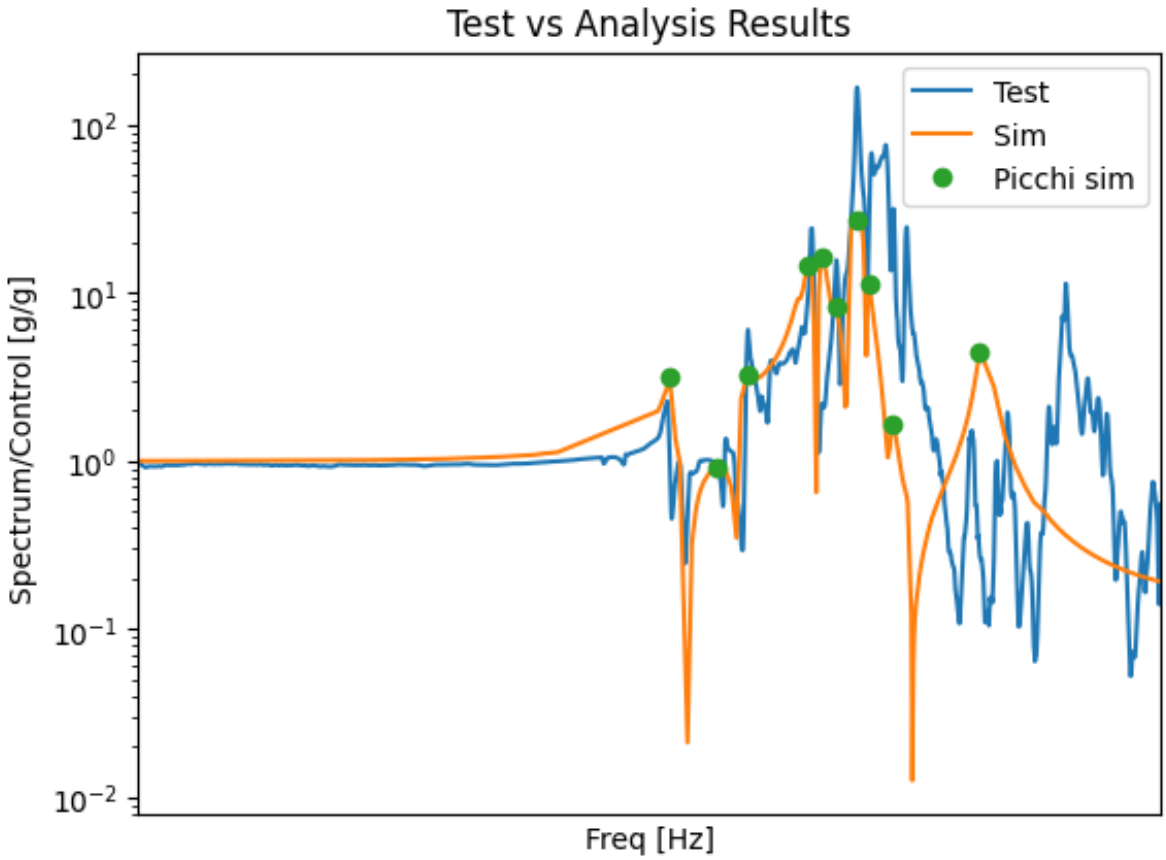

Figure 7.2: Comparison between analysis and test results in the Z axis

7.5 Error Localisation

As the initial correlation is carried out through the tools identified in section 7.4, the first step of the procedure, and the most important for the final outcome, can be performed. Firstly, the chosen modes for correlation, usually the main bending modes and the most participated modes as per analysis, are paired with the corresponding identified modes in the test data. Once there is sufficient fidelity in that pairing, the errors are computed to address which modes hold the most uncertainty, then an initial investigation on the most affected components of the structure from such modes is carried out. As the initial candidates for optimization are selected, the sensitivity analysis can be performed.
For small models comprised of a sufficiently low number of properties, such as the PS Dummy Mass,all the model cards can be subject to a sensitivity analysis. On FE models with a sufficiently big number of properties to be investigated such a direct approach is not suggested as the computational time and resources needed for the operation would be excessive.
As a reference a single sensitivity iteration, compiling a full column of the sensitivity matrix for a single variable, took on average 41 seconds for the PS Dummy Mass model. Correspondingly, the same process on the HAWK PLUS STM model took an average of 18 minutes. As such, for large structural models, a proper identification of highly affected areas for each uncertain mode should be carried out in advance to filter out some uninfluential properties on the chosen modes.
Selected methods for this investigation may be visual inspection of mode shapes both on analytical or test data, as well as more computationally intensive methods such as Kinetic Energy per node, similarly to the process used for sensor positioning as described in subsection 5.2.2.

7.5.1 Sensitivity Analysis

As the first set of candidates is selected for the sensitivity analysis, the software automatically reads the properties cards and builds the Θ matrix of variables. Each property card has several possible variables depending on the type of element or physical characteristic it is representing, examples may be thickness 't' for PSHELL or each individual component of the vector 'K' for PBUSH as well as 'rho' and 'E' for MAT properties. Each identified characteristic describing the property can be set as a

variable for optimization and can be treated independently from the others. This individual selection allows for the minimization of variables, improving the final optimization problem conditioning. Once the initial row of matrix Θ, which is the matrix of variables updated at each iteration, is completed, the software iteratively and automatically perturbs one component of said row, representing an optimization candidate, by a standard set value of 1% and compiles the DAT file launching the modal analysis. The resulting F06 file for each performed analysis is then read, and the frequencies are extracted to assemble the sensitivity matrix. Each component of the sensitivity matrix is dimensionless and is computed as described in Equation 7.3, where λ_{pt_j} and θ_{pt_j} represent the outcome frequencies and variable from the perturbed model, while λ_{0_j} and θ_{0_j} represent the initial model values.

$$G_{j,i} = \frac{\frac{\lambda_{pt_j} - \lambda_{0_j}}{\lambda_{0_j}}}{\frac{\theta_{pt_j} - \theta_{0_j}}{\theta_{0_j}}} \tag{7.3}$$

The G matrix has dimensions $[j \times i]$ where j is the number of chosen modes for updating and i is the number of variables in Θ. As this process requires to perform a sensitivity analysis for each iteration, it is heavily computational intensive and time consuming, as such it can be split in different runs for large models, saving the submatrix at each iteration and creating a final assembly at the end of the line.

7.5.2 First Optimization Iter

Once the sensitivity matrix is provided, a first optimization iteration, which is later detailed in section 7.6, can be performed. This optional step can be used as an auxiliary tool to properly assess each candidate's influence on the overall optimization process.
In this first iteration all the variables are left without boundaries, to check which ones are changed the most by the model. This result is affected by the sensitivity matrix, but provides insights on the variables changed the most by the optimizer during the process. This information may be impactful for error localisation, as the most affected areas are likely the ones impacting the uncertain modes the most and, as such, may provide an insight on where to focus the optimization effort in the updating procedure or in manual corrections of eventual modelling errors.

7.6 Optimization Process

The optimization process consists in iteratively computing the minimization problem of the objective function detailed previously in subsection 2.3.1. In order to perform this task, a pre-built optimizer from the scipy library [Sci], is chosen. That optimizer, namely $'lsq\_linear'$, solves a linear least-squares problem with bounds on the variables. The optimizer is provided with both matrix $A = -W \cdot G$, which represents a weighted version of the sensitivity matrix and vector $b = -W \cdot \frac{(\lambda_i - \lambda_m)}{\lambda_m}$ which is the residue computed with respect to the measured frequencies from the test data.
The weighting matrix W can be either set to identity or can be used to prioritize some of the selected modes. As the updated set of parameters is provided by the optimizer, it is saved in a new Θ row and the updated DAT is written to perform the modal analysis. As the results from the analysis are extracted MAC and MMI metrics are computed iteratively on the resulting modes with respect to the testing modes. The test results are then matched with the the updated modes presenting the highest values of the chosen metrics, described in section 7.4. As the modes are paired, λ_i, the objective function E(X) and MAC are computed and saved for the next iteration. The process is repeated for an arbitrary number of iterations chosen by the user or until the overall boundaries of the variables are reached.

7.6.1 Variables Boundaries

Different philosophies exist on how to address the variable boundaries during the optimization and hence correlation of a modal model. In this thesis, a physical approach has been selected to retain re-usability of the model in different analysis and tests, providing a comprehensive updating representative of the general structure. To achieve such a feat, a prior assessment of the variables and their physical nature has been carried out, summarized in Table 7.1. An overall uncertainty has been assessed to $\pm 10\%$ for materials. However to preserve batch integrity, meaning to avoid that the error between components made from the same batch of material during production was inconsistent, a local boundary was fixed to $\pm 5\%$. On the other hand for PSHELL and other geometrical entities the error, and hence the variable boundary ,was measured relatively to the

geometrical tolerance of the component, as per standard ISO 2768-mk [OMP], used in the mechanical drawings of machined components. Higher error margins were established for cast, commercial components such as the PS Dummy Mass brackets. The higher uncertainty, in turn, establishes higher boundaries for the optimization process.

Property	**Cards**	**Admissible Error**	**Cause**
MAT	E, ρ	$\pm 10\%(Overall)$ $\pm 5\%(Local)$	Material uncertainties from batch
PBUSH	K1,K2,K3,K4,K5,K6	$\pm 10\%$	Mathematical modelling uncertainty
PSHELL	t	Depending on admissible geometrical error from production drawing	Standard ISO 2768-mk

Table 7.1: Variables Boundaries Overview

Results

8.1 Test Cases

Two different test cases were carried out to test the methodology and the created code:

1. The **PS Dummy Mass**, described in subsection 4.1.3, was chosen as first test case to test the methodology and related code. The FE model presented a number of nodes several orders of magnitude lower than the actual STM model. This allowed computational times for the modal analysis in the order of seconds, enabling a fast trial and error implementation on both the code and the methodology adopted. The only test data gathered for this case was the Shaker output in the Z axis, as previously described in subsection 6.3.2. The correlation has been performed on Z axis exclusively as the scope of this test case is to test the algorithm and the code itself, rather than properly achieve a truthful correlated model of this subsystem.
2. The most important test case is represented by **HAWK PLUS STM**, described in subsection 4.1.2. The entire satellite STM FE model is several orders of magnitude bigger than the previous case, as a consequence the computational times for a singular modal analysis spaced between 15 to 20 minutes. Consequently, several improvement were needed to properly address the issue. These solutions are detailed in section 8.3. The objectives of this test case are:
    - to verify that the methodology could successfully be applied to large models,
    - provide a correlated model of HAWK PLUS STM.

8.2 Propulsion System Dummy Mass

The available test data didn't provide mode shapes, as it was gathered through shaker testing, hence a pairing analysis was carried out accordingly with the method described in subsection 7.4.3. The entire sensitivity matrix along all properties and cards of the FE model was deemed feasible due to the low computational time. The entire process of creating the matrix took approximately 40 minutes and provided sensitivity for the 3 identified modes in the Z direction with respect to all the 63 initial variables.
After the initial sensitivity study and results analysis a total of 11 final variables for iteration were selected. These variables included MAT, PSHELL and PBUSH property cards and provided a sensibility factor of at least 2% for each mode of interest.
As the parameters for updating were defined, the respective boundaries to ensure physical fidelity were assessed as described in subsection 7.6.1. Then, the iterative optimization was carried out, correlating the model and providing the results available in Table 8.1.

Mode	Initial Error	Final Error
1	7.32%	2.09%
2	11.88%	4.89%
3	4.59%	0.51%

Table 8.1: Correlation results for PS Dummy model

The variables chosen for optimization and their relative change has also been reported in Table 8.2 for references.
The results shown were obtained over 10 iterations of the optimization process; however, the variables saturated the boundary only in the final iterations as the error function was approaching its minimum. The number of iterations was defined based on the saturation of the variables boundaries. A visual representation of the cost function evolution, detailed in Equation 7.1, is visible in Figure 8.1. Lastly, the initial and final MAC matrices before(Figure 8.2a) and after(Figure 8.2b) the optimization process are provided in Figure 8.2. Most importantly, as already stated, the initial mode shapes are assigned from the initial FE model after performing the pairing described in subsection 7.4.3. This implies that the MAC in Figure 8.2a is actually an AUTO-MAC matrix.

Variable	Relative change	Boundary
E_1	-5%	$\pm 5\%$
Rho_1	3.01%	$\pm 5\%$
E_2	-5%	$\pm 5\%$
t_2	-8%	$\pm 8\%$
t_3	-7.5%	$\pm 7.5\%$
t_4	-6.67%	$\pm 6.67\%$
t_5	-5.06%	$\pm 7.5\%$
t_6	-6%	$\pm 6\%$
$BUSH_{15}K_4$	10%	$\pm 10\%$
$BUSH_{15}K_4$	10%	$\pm 10\%$
$BUSH_{16}K_2$	-10%	$\pm 10\%$

Table 8.2: Variables Variation with respect to their original value

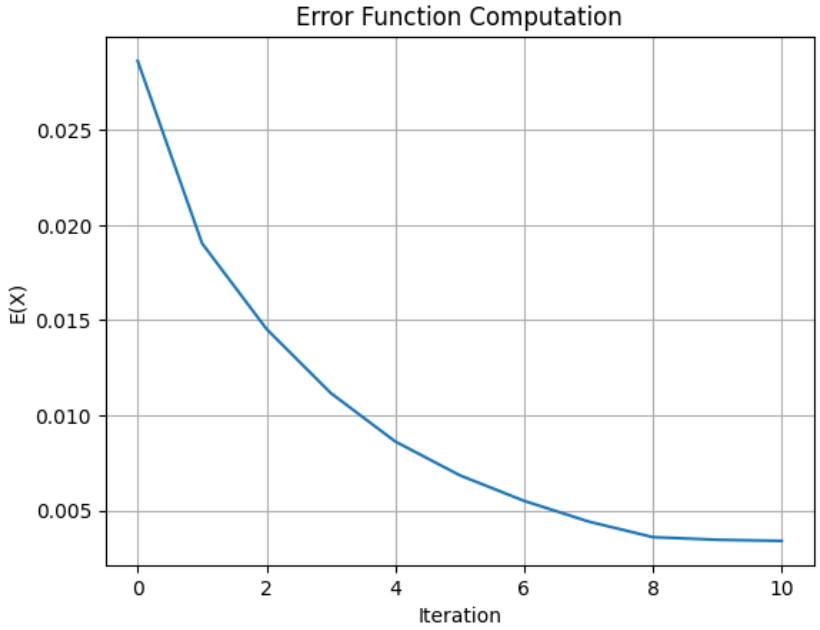

Figure 8.1: Error Evolution over 10 iterations

The optimization process drastically improved the cross-correlation between modes 2 and 3 while worsening the off-diagonal values for modes 1 and 2. This cross correlation is likely due to the low number of accelerometers available in the test and hence lower information on the actual differences between mode shapes. Despite this, the final MAC is within the acceptable values for correlation purposes.
It is clearly visible how the developed methodology successfully provided good error localization for accurate parameter selection, and hence a successfully correlated model with all the frequencies of interest being

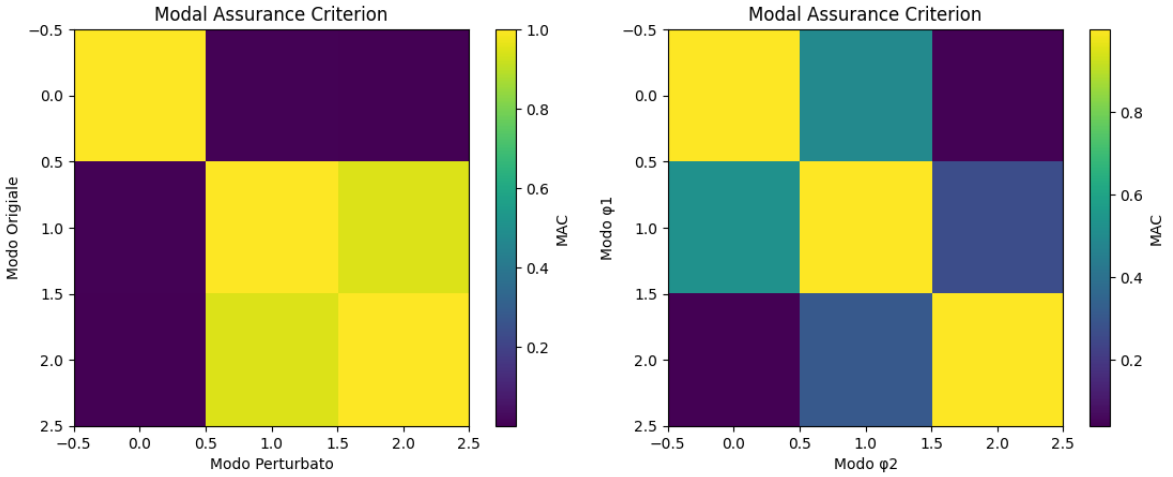

(a) MAC matrix before optimization (b) MAC matrix after optimization

Figure 8.2: MAC Matrices before and after Optimization

beneath the limits imposed by the normative [ESA08].

8.3 HAWK PLUS STM

The second test case to be correlated is the HAWK PLUS STM FEM, presenting a model several orders of magnitude bigger and consequently drastically longer computational times and iterations. Nonetheless, the developed code and methodology successfully handled the large model and allowed an automatic and iterative approach to the optimization problem as expected.
In this correlation case, both the hammer test results and the shaker vibration test results were available, but only the latter were presented in the results provided herein. This allowed an identical procedure to the one adopted for the PS Dummy Mass to be implemented, facilitating a more direct comparison between the two correlation cases. Similarly to the procedure adopted for the PS Dummy Mass and detailed in subsection 7.4.3, a pairing was performed between the normal modes identified in the shaker test and the ones determined analytically by the FEM model.
Once the test data had been collected and matched, the initial errors were computed and the procedure started with a sensitivity analysis. Since the model was too large for a complete sensitivity evaluation, the analysis was restricted to the Primary Structure Components, as these were considered the most influential in determining the modes governing the behaviour of the overall structure. Owing to the high computational cost and memory requirements, the sensitivity analysis was split into several sub-runs, after which the final matrix was reconstructed from the completed results.
A total of 8 modes were paired and matched with the test outcomes and hence used for the optimization procedure. Alongside the selected modes a total of 71 variables were identified for sensitivity in the regions interested by said modes. At the end of the error localisation process an overall of 14 variables were selected for the 5 optimization iterations. Initial and final errors in the chosen modes are visible in Table 8.3 while Table 8.4 showcases the chosen variables and their total variation with respect to the imposed boundaries. In the final iteration the weighting matrix was built as to distribute twice as much importance to the mode 4, which held the most overall error. As such, it is clearly visible in Table 8.3 that the optimizer forcefully reduced the error of said mode despite increasing the error of other modes. Such behaviour is expected, as modifying the modal

Mode	Axis	Initial Error	Final Error
1	Y	1.99%	3.23%
2	X	1.85%	3.71%
3	Z	6.27%	2.43%
4	X	18.32%	14.87%
5	Y	1.97%	4.73%
6	Y	2.83%	5.37%
7	Z	1.74%	6.21%
8	Z	1.51%	3.81%

Table 8.3: Correlation results for HAWK PLUS STM

Variable	Relative change	Boundary
E_1	-10%	$\pm 10\%$
Rho_1	7.48%	$\pm 10\%$
E_2	-10%	$\pm 10\%$
E_4	-10%	$\pm 10\%$
E_6	-10%	$\pm 10\%$
E_7	-7.50%	$\pm 10\%$
E_8	-10%	$\pm 10\%$
E_{Ring}	-10%	$\pm 10\%$
t_{Core_1}	-3.33%	$\pm 3.33\%$
t_{Core_2}	-5.00%	$\pm 5\%$
$t_{PlateZ+}$	-6.25%	$\pm 6.25\%$
t_{EPSBay}	-5.00%	$\pm 5\%$
$t_{Avio/AOCSBay}$	-5.00%	$\pm 5\%$
$BUSH_{PS}K_2$	-20%	$\pm 20\%$

Table 8.4: Variables Variation with respect to their original value

characteristics of a FEM model would impact the entire set of normal modes results.
The results combined with the initial sensitivity analysis proved that the chosen candidates had almost the same impact on the 3rd and 4th mode that they had on the other 6, already correlated, modes. This implies that as the optimizer attempted to correct the 4^{th} mode it over-corrected the already correlated ones by a similar percentage variation.
As visible from provided data, the error is concentrated around a single mode. due to the nature of its modal shape and the components affected by it, the primary components are not an ideal fit for this optimization. In Table 8.4, it is also visible that almost every variable has reached the boundaries, which in turn means that the optimizer has actually completed its minimization but the variables chosen didn't allow further

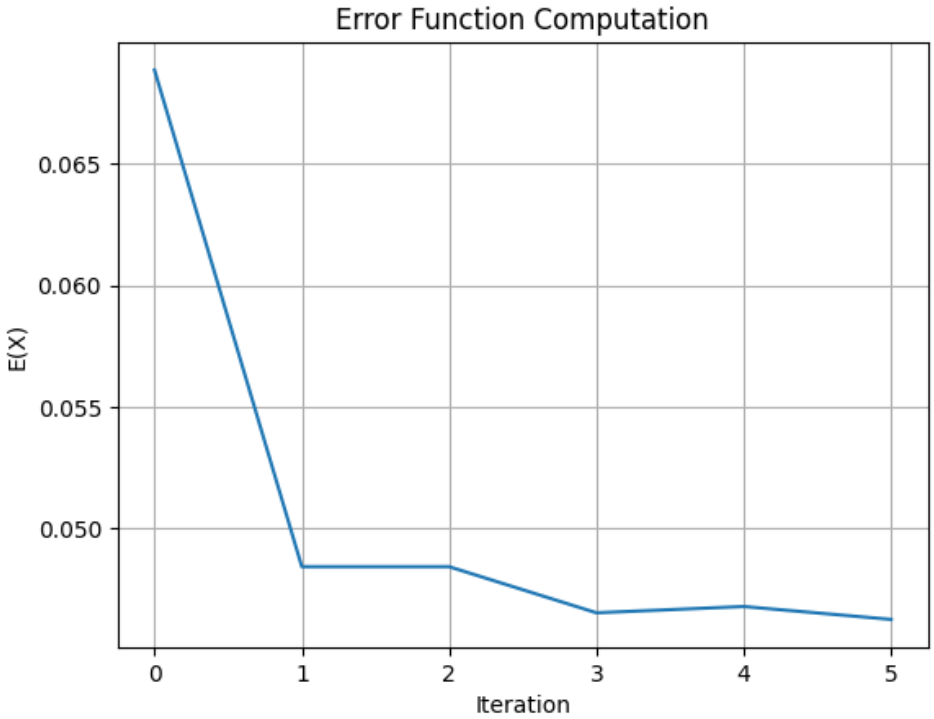

Figure 8.3: Error Evolution during the optimization iteration

optimization. This can also be seen in the cost function evolution plotted in Figure 8.3. Overall, the code proved effective in reducing the error of the target modes. Nevertheless, due to an inefficient choice of variables and the presence of a localized error, the final optimization did not produce satisfactory results in terms of the final model correlation.
To overcome this limitation, the entire procedure was repeated with particular attention to Mode 4, which showed the most significant localized discrepancy. A detailed analysis of the corresponding mode shape and of the components most influential to it revealed, from the analytical data, that this mode was governed more by the PS Dummy Mass than by the primary structure itself. On the basis of this result, the PS Dummy Mass properties were included in the subsequent iterations, and 11 variables were selected from the original set of 34 candidates.
The resulting errors are shown in Table 8.5, while Table 8.6 showcases the chosen variables, their boundaries and the actual change. The results from the second optimization process proved satisfactory as the solver successfully reduced the targeted mode uncertainty. The other already correlated modes are also almost unaffected by the optimization procedure, with the exception of mode 6 registering a 2.73% increase of

Mode	Axis	Initial Error	Final Error
1	Y	1.99%	1.93%
2	X	1.85%	1.75%
3	Z	6.27%	6.08%
4	X	18.32%	12.72%
5	Y	1.97%	2.38%
6	Y	2.83%	5.56%
7	Z	1.74%	2.85%
8	Z	1.51%	1.42%

Table 8.5: Correlation results after the second optimization

Variable	Relative change	Boundary
E_6	−5.00%	±5%
$E_{99200000}$	2.00%	±5%
$Rho_{99200000}$	5.00%	±5%
$E_{99200001}$	−5.00%	±5%
t_{Core_1}	−0.76%	±3.33%
$BUSH_{99200006}K_3$	−9.61%	±10%
$t_{99200007}$	−8.00%	±8%
$t_{99200008}$	−7.50%	±7.52%
$t_{99200009}$	−8.89%	±8.89%
$t_{99200010}$	−8.00%	±8%
$t_{99200010}$	−9.61%	±10%

Table 8.6: Variables Variation in the second optimization

the measured error. This set of results is deemed successful in the correlation of the model. The initial and final MAC matrix is provided as reference in Figure 8.4.
The final MAC matrix after the optimization cycle shows reduced correlation in the diagonal elements, especially in the most modified modes. This is expected as the procedure focused on modifying the areas affecting said modes, as such creating differences from the initial mode shapes imposed before optimization. Nonetheless, the modes were successfully tracked and the MAC function still shows acceptable values. Notably, the variables, in particular the thickness of the PS Dummy Mass brackets, were assigned higher boundary limits. This is due to the brackets being Commercial Off The Shelf (COTS) cast components, which present higher geometrical tolerances in their dimensions with respect to internally manufactured detail components such as the primary structure. Although the procedure proved successful in diminishing the error on selected modes it has not yet reached the target 10% error as required by

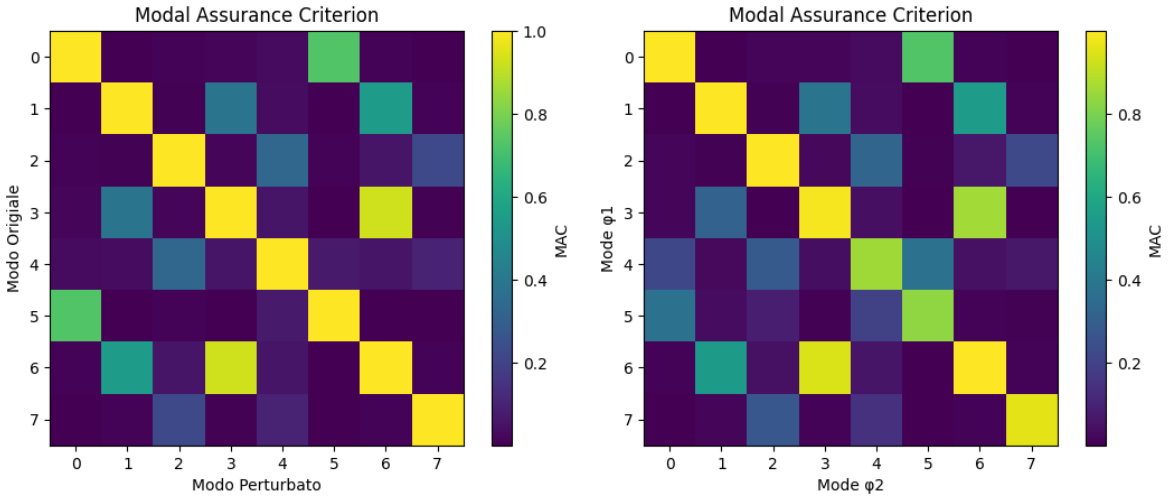

(a) MAC matrix before optimization (b) MAC matrix after optimization

Figure 8.4: MAC Matrices before and after Optimization

ECSS [ESA08], but it provided crucial data on the localisation of the uncertainties of the model. Future optimization iterations, including other variables or tailoring the cost function to the test case, shall be performed to effectively correlate the model to the standards defined by the normative.

Conclusions

The methodology presented in this thesis provides an iterative, automated tool to correlate FE models with the test results. The entire process from data acquisition to the final correlated model is described and applied effectively to two different test cases. Results from the first test case, namely the PS Dummy Mass, showcase an effective application of the methodology, successfully correlating the FE model to the normative standards. The second test case, being HAWK PLUS STM, highlights the necessity of proper variable selection to correctly assess the error localisation in the model. Long computational times to perform the sensitivity analysis proved to be an hinderance throughout the correlation process, effectively limiting the error localisation capabilities. As such, the final test case requires additional iterations through the variables in the model to properly identify additional sources of error, in order to conclusively correlate the model to the normative standards. Nonetheless, the methodology proved successful in optimizing target modes, either through distributed errors, such as in the first test case, or strongly localized error, as in the second test case. Retaining the physical reliability of the model has also proven to be a challenging aspect, as the boundary limits of the variables heavily influence the overall capabilities of the optimizer to converge.

9.1 Future Improvements

Future development and integration of the methodology include:

- Investigating additional variables to fully correlate the HAWK PLUS STM FE Model;
- Including Hammer test data and postprocessing in current or future test cases, to test the method implementation and possibly adding a

second optimization step based off modal shapes and related metrics;

- Implementing and testing different, customized cost functions to efficiently include the variable boundaries in their weighting. Explore different optimization methods to better handle such functions;
- Iteratively updating the sensitivity matrix at each iteration, to achieve finer tuning of the model at each step of the optimization process.

Bibliography

[GS95] Robin S. Glassburn and Suzanne Weaver Smith. "EVALUATION OF SENSOR PLACEMENT ALGORITHMS FOR ON-ORBIT IDENTIFICATION OF SPACE PLATFORMS". MA thesis. University of Kentucky, 1995.

[JCL95] George H. III James, Thomas G. Carne, and James P. Lauffer. "The Natural Excitation Technique (NExT) for Modal Parameter Extraction from Operating Structures". In: *Modal Analysis: The International Journal of Analytical and Experimental Modal Analysis* 10 (1995).

[Irv00] Tom Irvine. *AN INTRODUCTION TO FREQUENCY RESPONSE FUNCTIONS*. Tech. rep. Vibrationdata.com Publications, 2000.

[HF01] Jimin He and Zhi-Fang Fu. *Modal Analysis*. Butterworth-Heinemann, 2001.

[PD01] Bart Peeters and Guido De Roeck. "Stochastic System Identification for Operational Modal Analysis: A Review". In: *Journal of Dynamic Systems, Measurement, and Control (ASME)* 123.4 (2001).

[Ber04] Dionisio Bernal. "Modal Scaling from Known Mass Perturbations". In: *Journal of Engineering Mechanics* (2004).

[Fit+12] Kristin Fitzpatrick et al. *INTERNATIONAL SPACE STATION MODAL CORRELATION ANALYSIS*. Tech. rep. NASA, 2012.

[Avi14] Peter Avitabile. "MODAL SPACE (in our own little world)". In: *SEM Experimental Techniques* (2014).

[Beh+15] Iman Behmanesh et al. "Hierarchical Bayesian model updating for structural identification". In: *Mechanical Systems and Signal Processing* (2015).

[YS17] Liangliang Yu and Hanwen Song. "Scaling Mode Shapes in Output-Only Structure by a Mass-Change-Based Method". In: *Shock and Vibration* (2017).

[Sch20] Peter Schaldenbrand. *Modal Testing: A Practical Guide - Siemens Testing*. https://community.sw.siemens.com/s/article/Modal-Testing-A-Guide. 2020.

[Chi21] Akobuije Chijioke. *Characterization of laser Doppler vibrometers using acousto-optic modulators*. https://www.nist.gov/programs-projects/dynamic-mechanical-metrology-acceleration-force-and-acoustics/characterization. 2021.

[Oh+21] Yosep Oh et al. “Neural network-based build time estimation foradditive manufacturing: a performance comparison”. In: *Journal of Computational Design and Engineering, 2021, 8(5), 1243–1256* (2021).

[Sve+21] Bjørn T. Svendsen et al. “Improved finite element model updating of a fullscale steel bridge using sensitivity analysis”. In: *Structure and Infrastructure Engineering* (2021).

[AN22] ASI and NASA. *ArgoMoon image of Earth - ASI/NASA*. https://www.asi.it/2022/11/gli-scatti-lunari-di-argomoon/. 2022.

[ESA22] ESA-ASI. *ESA - LICIACube Image of Asteroid Ejecta*. https://www.esa.int/ESA_Multimedia/Images/2022/10/LICIACube_image_of_asteroid_ejecta. 2022.

[Liu+22] Shijie Liu et al. “Dynamic PSF-based jitter compensation and quality improvement for push-broom optical images considering terrain relief and the TDI effect”. In: *Applied Optics 61* (2022).

[CS25] Justin G. Chen and Eric C. Stewart. *Video-based Methods for Measurement of Vibration Mode Shapes*. Tech. rep. NASA, 2025.

[ESA25] ESA. *IRIDE: presentata presso il Centro ESA–ESRIN la prima immagine*. https://www.esa.int/Space_in_Member_States/Italy/IRIDE_presentata_presso_il_Centro_ESA_ESRIN_la_prima_immagine. 2025.

[Srl25] Argotec Srl. *HAWK PLUS Brochure*. https://www.argotecgroup.com/products/platform/hawk-plus. 2025.

[Insa] Crystal Instruments. *Hammer Testing*. https://www.crystalinstruments.com/hammer-impact-test.

[Insb] Crystal Instruments. *Standard Modal Analysis*. https://www.crystalinstruments.com/modal-analysis.

[Insc] Crystal Instruments. *Swept Sine Vibration Testing*. https://www.crystalinstruments.com/sine-control.

[Ras] Hamid Rastan. “Frequency Response Function: Theory & Applications Guide”. https://caeflow.com/vibration$_a nd_a coustics/frequency - response - function$.

[Sci] Scipy. *Optimizer from Scipy Library*. https://docs.scipy.org/doc/scipy/reference/generated/scipy.optimize.lsq_linear.html#scipy.optimize.lsq_linear.

[Cal97] Adriano Calvi. “Finite Element Model Updating in Structural Dynamics using Design Sensitivity and Optimisation”. PhD thesis. Cranfield University-College of Aeronautics, 1996-97.

[ESA08] ESA. *ECSS-E-ST-32-11C, Space Engineering - Modal Survey Assessment*. 2008.

[ESA23] ESA. *ECSS-S-ST-00-01C Rev.1, System - Glossary of Terms*. 2023.

[Arg] Argotec. *ISSPresso*. https://en.wikipedia.org/wiki/ISSpresso.

[MSC22] MSC. *MSC Nastran 2022.2,Dynamic Analysis User’s Guide*. 2022.

[HEX22] HEXAGON. *DMAP Programmer's Guide*. 2022.

[HEX23] HEXAGON. *Superelements and Modules User's Guide*. 2023.

[OMP] OMPItaly. *ISO2768-mk*.

[Pag25] Alfonso Pagani. *Richiami di dinamica,risposta a carichi random e analisi vibroacustica - corso di Strutture per Veicoli Spaziali*. Tech. rep. Politecnico di Torino, 2024/2025.